MICROPLASMA TRANSISTOR FOR HARSH ENVIRONMENT APPLICATIONS

by

Pradeep Pai

A dissertation submitted to the faculty of
The University of Utah
in partial fulfillment of the requirements for the degree of

Doctor of Philosophy

Department of Electrical and Computer Engineering

The University of Utah

May 2015

Copyright © Pradeep Pai 2014

All Rights Reserved

The University of Utah Graduate School

STATEMENT OF DISSERTATION APPROVAL

The dissertation of **Pradeep Pai**

has been approved by the following supervisory committee members:

Massood Tabib-Azar, Chair **10/28/2014**
Date Approved

Marc Bodson, Member **10/29/2014**
Date Approved

Bruce Gale, Member **10/31/2014**
Date Approved

Carlos Mastrangelo, Member **10/28/2014**
Date Approved

Darrin Young, Member **10/30/2014**
Date Approved

and by **Gianluca Lazzi**, Chair/Dean of

the Department/College/School of **Electrical and Computer Engineering**

and by David B. Kieda, Dean of The Graduate School.

ABSTRACT

Microplasmas are currently used in displays, two-terminal breakdown switches, light sources, and medical instruments. They can also be used in miniaturized particle accelerators, micro-X-ray generators, UV and extreme UV sources, gas sensors, and in micropropulsion thrusters. They are also excellent candidates for applications in harsh environments that usually lead to the breakdown of silicon electronics. Here we develop their unique applications in X-band microwave analog and digital devices and circuits. To enable these applications, we identified a breakdown region, called sub-Paschen regime that enables generation of atmospheric plasmas at low voltages. The sub-Paschen regime, involves devices with a breakdown gap below 10 μm in 1 atmosphere in air. This newly discovered operation regime enabled us to design plasma devices with relatively low operation voltages of 50–100 V.

We developed microplasma devices similar to metal oxide semiconductor field effect transistors (MOSFETs) with drain, source, and gate regions that used plasma channels for switching or amplification. The gate field effect was successfully tested under both direct current (dc) and alternating current (ac) excitations. A drain current modulation frequency up to 7 GHz was obtained. Additionally, we implemented logic gates with microplasma devices to realize simple Boolean logic operations including OR, AND, NOT, and XOR. The gates were then combined to obtain a 1-bit half-adder circuit. The MOPFET developed in this work achieved 3x reduction in the breakdown (device

turn-on) voltage by operating in the sub-Paschen regime. In addition to the scaling in breakdown voltage, the microplasma field effect transistors (MOPFETs) are at least 50x smaller compared to plasma transistors reported in the past. The smallest MOPFET used in this work had a source-drain gap of 1 μm and showed unprecedented functionalities derived from plasmas at a microscale.

Dedicated to my parents, Mr. Prakash Pai and Mrs. Veena Pai

TABLE OF CONTENTS

ABSTRACT iii

LIST OF TABLES viii

ACKNOWLEDGMENTS ix

Chapters

1. INTRODUCTION 1

    1.1 Motivation 1
    1.2 Literature review 3
    1.3 Novelty of this research work 7
    1.4 Scope of the research work 8

2. MOPFET THEORY AND DESIGN 10

    2.1 Basics of plasma 10
    2.2 Plasma discharge 11
    2.3 Microplasma field effect transistor 18

3. FABRICATION 21

    3.1 Material selection 21
    3.2 MOPFET physical design 23
    3.3 Fabrication techniques and challenges 25

4. MOPFET DC CHARACTERIZATION 42

    4.1 Sub-Paschen breakdown 42
    4.2 Gate field-effect 49
    4.3 MOPFET transconductance 55
    4.4 Comparison between TiW and Cu MOPFETs 60
    4.5 Carrier mobility 62

5. MOPFET RF CHARACTERIZATION 67

    5.1 RF plasma switching with two electrodes 67

5.2 Gate field-effect with dc excitation..71
5.3 Gate field-effect with rf excitation..71

6. MICROPLASMA LOGIC CIRCUITS..81

6.1 Diode-resistor scheme...82
6.2 Space charge scheme 88

7. CONCLUSION..99

REFERENCES 102

LIST OF TABLES

Tables

3.1: Properties of some common materials used in microfabrication considered as potential candidates for the MOPFET electrodes. Tungsten is the material of choice due to its low FOM 23

6.1: Response of the AND/OR logic circuit of Fig. 6.3a for different combinations of inputs 86

6.2: Response of the XOR logic circuit of Fig. 6.4a for different combinations of inputs 87

ACKNOWLEDGMENTS

According to the Hindu philosophy, two keys to achieve success are to set a goal and follow a Guru. I consider myself extremely lucky to have found my Guru, my advisor Prof. Massood Tabib-Azar, who supported me unconditionally through the course of my degree program and has made me the researcher I am today. He has been a constant source of inspiration and motivation for me, and I cannot thank him enough for the countless ways in which he has helped me. Likewise, I want to thank my first Gurus, my parents Mr. Prakash Pai and Mrs. Veena Pai, for their unconditional love and support. They taught me the value of hard work and instilled discipline in me that has helped me at every stage of my life and made me the person I am today.

I want to thank my committee members, Prof. Mastrangelo, Prof. Young, Prof. Bodson, and Prof. Gale, for their time and effort in evaluating this work. They have been my teachers, critics, and supporters through different stages of my degree program and have helped me be a better researcher. The journey of a graduate student is hard and uncertain. It is the constant support of family, friends, and colleagues that gave me the strength to overcome the hurdles in my path and made this journey a memorable one. I want to thank my sister, Ms. Priya Kamath, for always believing in me.

I would also like to thank the Defense Advanced Research Projects Agency for giving me an opportunity to work on this interesting project and financially supporting it. I also want to thank the College of Engineering for publicizing this research work. Last,

but not the least, I would like to thank the staff at Nanofab Utah for their technical assistance and inputs that helped me during the device fabrication.

CHAPTER 1

INTRODUCTION

1.1 Motivation

Ever since their invention, transistors have revolutionized the electronic industry and have today become an integral part of every electronic component. Following Moore's law in their development, these devices have tremendously improved in performance and speed by pushing size scale close to the physical limits. However, there are certain applications involving harsh environment operation where even the performance of these limitless devices are put to the test. Silicon based-semiconductors, which are the basic building blocks of these transistors, unfortunately cannot operate in harsh environment such as high temperatures and ionizing radiation due to excess carrier generation. Electronics used in satellites, space exploration, nuclear reactors and oil drilling applications are constantly subject to temperatures in excess of 300 °C and require special shielding to protect the electronics. Although silicon-on-insulator complementary metal oxide semiconductors (SOI-CMOS) are being used to extend the operating temperature range of semiconductor electronics, this is only a work around and increases the maximum temperature limit only by 50–100 °C. Alternately, large band-gap semiconductors are being used for higher temperatures, but do not have the same advantages as silicon in material processing. The motivation of this research work is to develop robust electronics for harsh environments that can overcome the limitation of

silicon-based transistors.

Alternate devices have been proposed to address these shortcomings. Carbon nano tube (CNT) is a promising device that can outperform the MOSFET in almost every aspect. The drawback of CNT is in the post fabrication process. Although CNTs have been successfully mass fabricated, there has been no work reported to date that has produced well aligned CNTs with ohmic contacts at a large scale. There have been reports of microelectromechanical systems (MEMS) and nanoelectromechanical systems (NEMS) switches implemented as CMOS and logic gates. These devices could survive harsh environments, but cannot match the operating speed of MOSFETs due to the nature of their operation.

An interesting alternative has been proposed recently in the form of plasma transistors. These transistors use a gaseous medium (plasma) as the active component to perform electronic switching for information processing similar to a semiconductor transistor. The ready availability of electrons and ions in plasma makes it inherently suitable to be used as an electronic component like diode or transistor. In addition to this, plasma can sustain high temperatures and ionizing radiation due to its physical nature. Despite this fact, very less work has been done in these lines.

Plasma possesses interesting physical and chemical properties that makes it versatile. Plasma finds use in a wide variety of applications such as displays, material processing, gas sensing, spacecraft thrusters and numerous biomedical applications, to name a few. In addition to its versatility, plasma retains its properties even when scaled in size, which allows for miniaturization of the devices. Semiconductor micromachining techniques have been used to realize microscale pixel arrays for display and plasma

torches for material processing at an atomic level.

1.2 Literature review

Plasma can be produced by super-heating a gas until it decomposes to its atomic components. At a small scale, it can be more efficiently produced by applying a large electric field through the gas that breaks down the gas to its atomic/molecular components. All the commercial and lab applications that use plasma generate plasma in this manner. Plasma generated in such a manner is composed of ions and electrons that are in thermal nonequilibrium where the temperature of electrons exceeds that of ions by 1–2 orders of magnitude. Due to the large size and mass of ions, the overall temperature of the plasma is typically in the range of 200–700 °C and decays rapidly outside the plasma core. The electric current sustaining the plasma can be modified to control the plasma temperature and even bring it down to room temperature [1]. This makes it convenient to be used in practical applications. Current conduction in plasma occurs due to ions and electrons. However, due to their heavier mass, ions fail to respond to frequencies greater than a few hundred kilohertz, and the current is carried entirely by electrons. Nevertheless, switching can be reliably performed both at high and low frequencies with or without involving ionic conduction. The following subsections mention some applications of microplasma devices.

The basic characteristics of plasma include light emission, high temperature, low resistance, etc. The most popular microplasma device is a plasma display. The individual pixels of a plasma display consist of a microcavity where plasma is generated. The light emitted from the plasma then passes through the respective color filter to obtain a colored image. The wavelength of light emitted by plasma depends on the composition of the gas

used. Based on this property, gas sensors have been realized that determine the composition of gas based on its optical emission [2]. The high temperatures resulting from plasma arc discharges are used in welding. Such arc discharges can also be produced at a microscale to perform microwelding. The semiconductor industry uses plasma at a larger size scale for material processing. There are reports of a microversion of this application that was used to synthesize materials at a nanoscale in a much localized area [3]. Recently, the biomedical industry has employed UV emitting plasma torches to sterilize surgical instruments. Since the temperature of the plasma can be lowered down to room temperature, the sterilization usage has been extended to skin treatments by direct contact with plasma. The radiation from the plasma can kill stubborn bacteria that are immune to medication. The light emission from plasma has also been used as a source of illuminating and decorative lighting. The electrical applications of microplasma make use of its low resistance. The low resistance results from the higher electron mobilities in plasma compared to semiconductors. Plasma is also an abundant source of charge carriers. These properties have been used to realize microplasma switches and transistors in different ways as mentioned below.

1.2.1 Microplasma switches

Rahaman et al. demonstrated a microplasma switch that could switch with subnanosecond speeds [4]. The device consisted of a spark gap comprising two metal electrodes separated by a 100–200 μm gap. The plasma was produced by pulsing high voltage dc (5–10 kV) through a gas maintained at high pressure (1–5 atm). Rocca and Floyd demonstrated the switching of a plasma current by using a magnetic field that deflected the electrons away from the discharge region [5].

1.2.2 Microplasma transistors

There have been quite a few reports of microplasma transistor in recent years. Chen and Eden developed a plasma transistor (Fig. 1.1) very similar in operation to a bipolar junction transistor (BJT), consisting of an electron emitter [6]. They were able to achieve a 4 times the increase in the conduction current by biasing the electron emitter to -20 V. Their work demonstrated a good technique to achieve gain in plasma transistors. The device was, however, not dynamically characterized for its switching speed. Wagner et al. developed a plasma BJT (Fig. 1.2) that consisted of a hybrid plasma-semiconductor interacting device [7]. The plasma BJT exhibited a voltage gain of 27 and was able to turn off the device (plasma) with a mere 1 V of emitter-base voltage. Despite these impressive features, the device lacked in speed due to large emitter-base capacitance that limited it to 4 kHz.

Yuan et al. developed a microplasma transistor that relied on a field effect to produce switching [8]. Their work used the field effect to modulate the ionic concentration in the conduction channel of a radio frequency (rf) plasma, which in turn modulated the plasma current. The work also demonstrates the feasibility of operating a plasma device under a harsh environment involving high temperatures and ionizing radiation.

All of the switches and transistors described above are large in size (>50 μm) with an interelectrode separation of similar size. Due to this, the operating voltage of these devices was in excess of 300 V. Although this is not a problem for devices meant to operate individually, it creates a major hindrance to the development of integrated devices to realize complex functionality. Hence, there are two factors that need to be

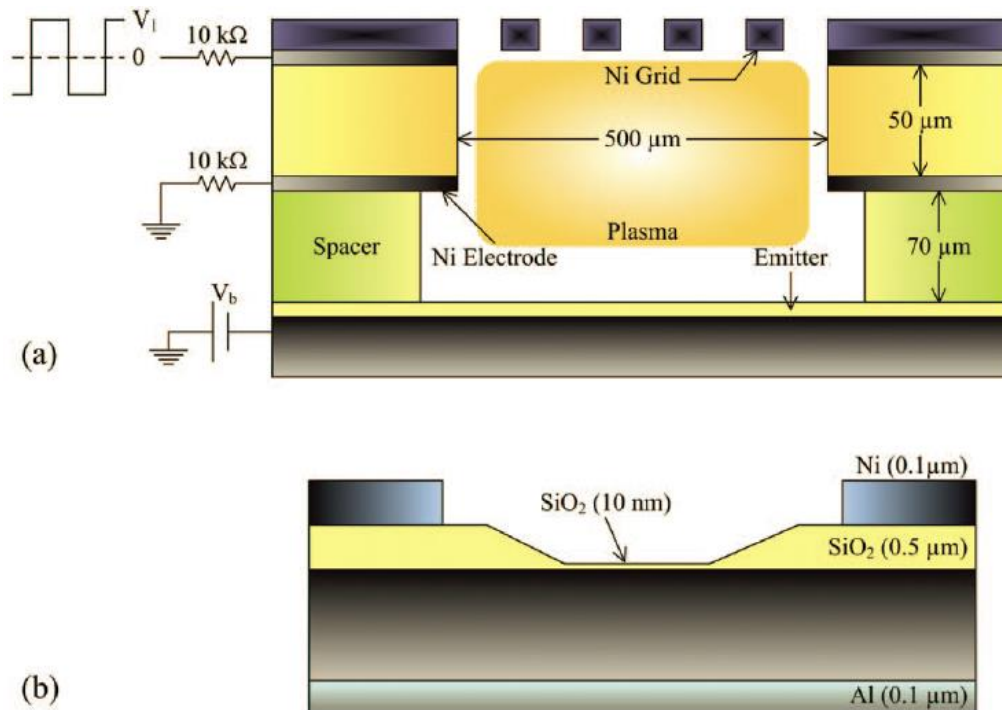

Fig. 1.1.[1] Structure of the microplasma transistor developed by Chen and Eden. (a) cross sectional diagram and electrical connections for the entire device and (b) detailed cross section of a MOS electron emitter.

addressed for further development of plasma transistors/switches, viz. size scaling and voltage scaling.

Cai et al. [9] and Chowdhury et al. [10] have tried to address these problems by isolating the plasma source from the switching device. Plasma was generated in a plasma torch by rf excitation, and the charge carriers in plasma were then flown over a large number of small, three-electrode devices to perform switching. Fig. 1.3 shows a schematic of the device used by Cai and Chowdhury.

The operating principle of the device was an extension of the Langmuir probe with the addition of a third electrode. Although this technique succeeded in lowering the

[1] Reprinted with permission from K. F. Chen and J. G. Eden, “The plasma transistor: A microcavity plasma device coupled with a low voltage, controllable electron emitter,” *Appl. Phys. Lett.*, vol. 93, pp. 161501, 2008. Copyright 2008, AIP Publishing LLC

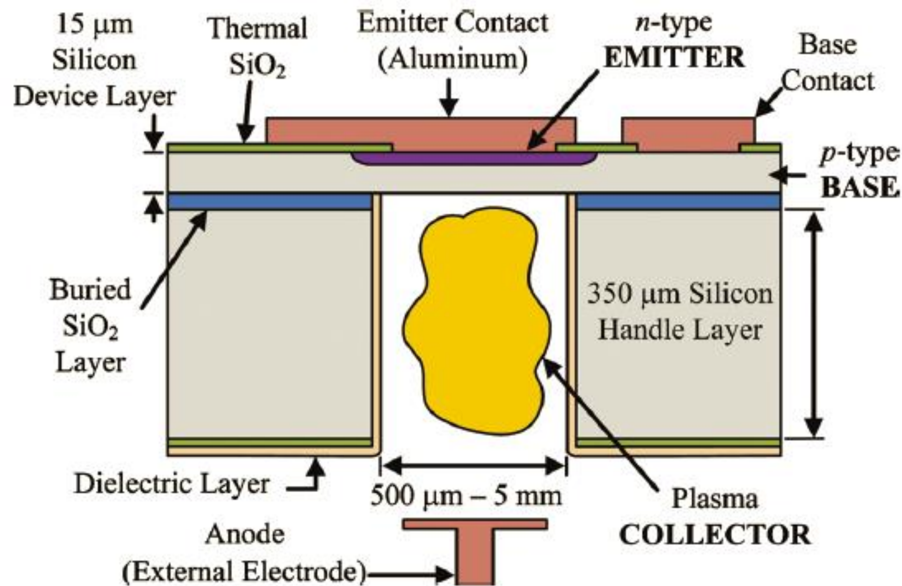

Fig. 1.2.[2] Cross sectional diagram of the npn plasma BJT developed by Wagner et al.

operating voltage of the transistor and reducing the size, it suffered from a slow switching time. The device characteristics were also sensitive to the position of the plasma torch. Also, the electrons from the plasma would pass through the electrodes of an inactive device, resulting in a nonzero current.

1.3 Novelty of this research work

This research work developed a MOPFET that operated with localized plasma and yet managed to keep the size and operating voltages small. Different variations of MOPFET were fabricated and tested. Fig. 1.4 shows a schematic of a generic MOPFET. The device consists of three electrodes similar to a MOSFET, namely source, drain, and gate, that serve a similar purpose as in a MOSFET. The source and drain electrodes are separated by a gap where plasma is generated. The length of the gap is less than 5 µm,

[2] Reprinted with permission from C. J. Wagner, P. A. Tchertchian, and J. G. Eden, "Coupling electron-hole and electron-ion plasmas: Realization of an npn plasma bipolar junction transistor," *Appl. Phys. Lett.*, vol. 97, pp. 134102, 2010. Copyright 2010, AIP Publishing LLC.

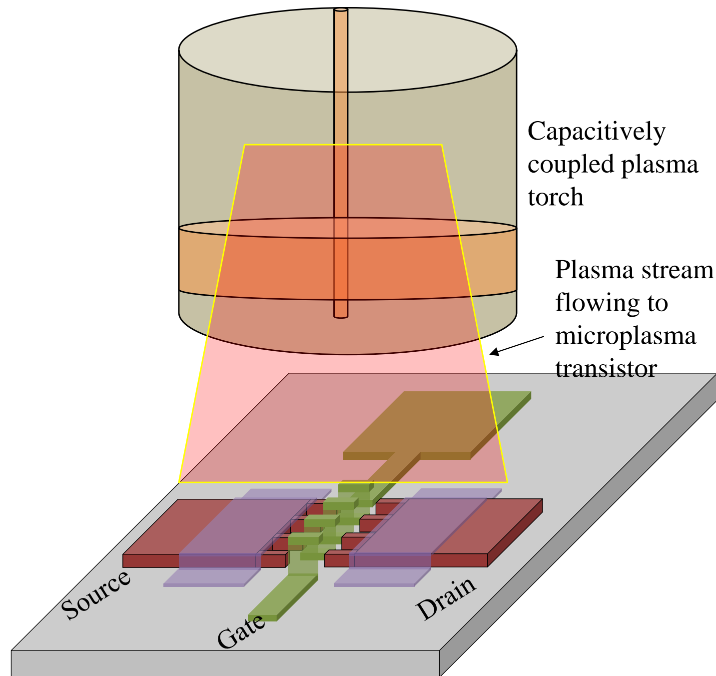

Fig. 1.3. Schematic of the microplasma field effect transistor developed by Cai and Chowdhury. Charge carriers for the transistor switching are supplied by the external plasma torch.

which is at least an order of magnitude smaller than the devices reported in [6]. The gate electrode interacts with the plasma in close proximity from one of the sides (bottom, in Fig. 1.4). The gate voltage modulates the drain-source current by actively injecting electrons into or sinking electrons away from the channel region (plasma). Both dc and rf excitation were used to generate plasma. Since the plasma was generated within the device, this design overcomes the drawbacks of the plasma transistor demonstrated by Cai and Chowdhury.

1.4 Scope of the research work

The central focus of this research work is to develop high temperature electronic switching device. The three major goals of this research work are listed as follows:

1) Develop a reliably switching low voltage plasma transistor with >1 GHz

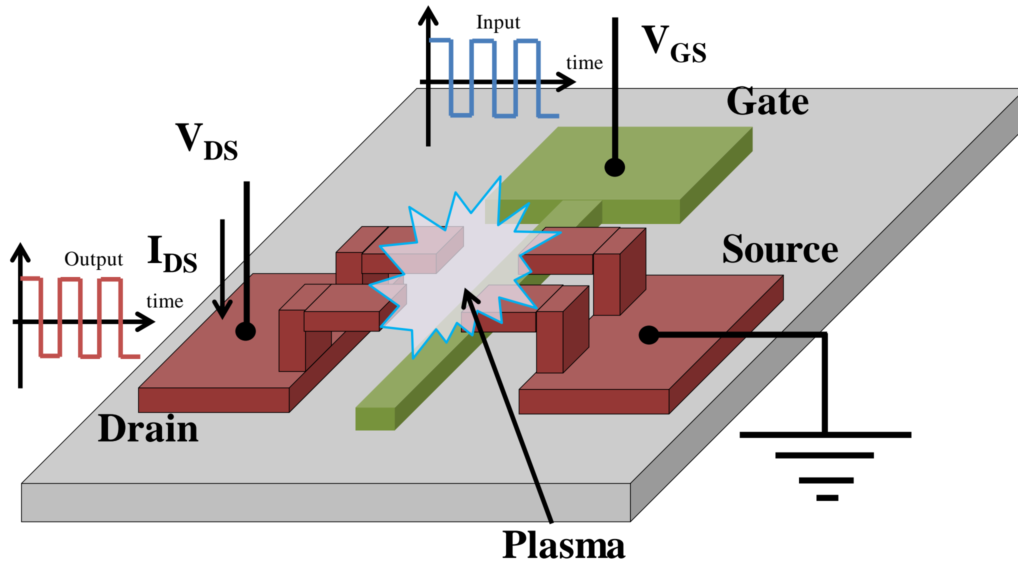

Fig. 1.4. Schematic of the MOPFET device structure. Plasma is created between the source and drain electrodes by the voltage V_{DS}. The gate voltage V_{GS} interacts with the plasma and modulates the drain current.

operating speeds.

1) Demonstrate size scalability of the transistor for reduced footprint and lower power dissipation.
2) Demonstrate application of the transistor for analog and digital switching.

A plasma transistor that meets all these goals will be the smallest one of its kind reported till date. To achieve size scaling to such an extent, a good understanding of the plasma discharges at micron scale is necessary. This is discussed in detail in Chapters 2 and 3. There were several challenges addressed to develop a continuously operating microplasma transistor that are explained in detail in Chapters 3, 4, and 5. In addition to the transistor, other unique microplasma devices were developed for logical switching operations. These devices are presented in Chapter 6.

CHAPTER 2

MOPFET THEORY AND DESIGN

2.1 Basics of plasma

It is necessary to understand the conditions that prevail in plasma and the carrier dynamics before getting into the details of the working principle of a MOPFET. From the basic definition of plasma, it is the fourth state of matter apart from solid, liquid, and gas. It is a mixture of ions and electrons that are dissociated from their constituent molecules/atoms. The electrons and ions are randomly distributed through the bulk of the plasma medium due to which there is no net electric field in the plasma and thus, there is no charge accumulation in the absence of an external electric field. Plasma can be broadly classified into strongly ionized and weakly ionized plasma [11]. The matter is almost completely ionized (no neutral atoms/molecules) in a strongly ionized plasma. Due to the constant collision with electrons and having no means to dissipate the energy, the ions reach a thermal equilibrium with the electrons in a strongly ionized plasma and therefore exist at high temperature in excess of 5000 K. Typical examples of strongly ionized plasmas are the matter found in stars, nuclear fusion reactors, etc. Most of the laboratory and industrial use plasmas are weakly ionized. They can be easily produced by applying strong electric fields through gases. Although the degree of ionization (ratio of number density of ions and neutral molecules) changes depending on the method of excitation, it is usually less than 10^{-6}. With plenty of neutral gas molecules available per

ion, the ions lose their energy through collision with the neutral molecules/atoms. As a result of this, the temperature of weakly ionized plasma is low (a few hundred K above room temperature) compared to the electrons (>5000 K). Typical examples are the plasmas found in reactive ion etchers, neon signs, etc. The plasma generated in this work is weakly ionized.

2.2 Plasma discharge

Plasma can be produced by both dc and ac electric fields. For simplicity, dc excitation is considered here to explain the evolution of a discharge and its classification. A simple plasma discharge apparatus consists of a glass tube with two electrical leads separated by a gap. The glass tube is filled with any choice of gas and maintained at a low pressure (0.1–10 Torr). The pressure of gas affects the excitation field required for a discharge and will be discussed in detail in later chapters. The leads are connected to a variable dc voltage source. At small voltages of a few hundred volts, there is practically no current flowing through the gas. However, a sensitive ammeter could detect very small currents less than pico A. This is due to the random charges produced in the gas by cosmic rays and natural radioactivity. Intentionally irradiating the gas with UV or X-ray radiation can increase this current to hundreds of nano A. When the voltage is increased to a few kV, the randomly created electrons are greatly accelerated by the strong electric field and produce ionizing collisions with neutral gas molecules. Every ionizing collision knocks an electron out of the neutral gas molecule. The new electron accelerates in the field and produces more electrons. In addition to the electrons produced by impact ionization, there are additional electrons produced at the cathode through secondary processes that further amplify the current through the gas. This leads to an avalanche

multiplication of electrons and causes electrical breakdown of the gas. The electrical breakdown/discharge can be classified into different types based on its appearance and current conduction [12].

For low pressures (<1 atm) and high external resistance, the discharge is accompanied by a glow that engulfs the entire area between the cathode and anode. Due to its appearance, this type of discharge is called a glow discharge (Fig. 2.1). Glow discharges are usually sustained by currents of 10s of micro A up to 1 A.

As shown in Fig. 2.1, the glow discharge occurs in the form of alternate glowing and dark regions. The glow in certain regions is due to the excitation of atoms. Ionization mostly occurs in the cathode dark space. The positive column has an almost equal number of electrons and ions and is therefore neutral. Similar to the ionic sheath at the cathode, there is a thin sheath of electrons near the anode. However, the potential drop in the anodic sheath is much smaller than the cathode sheath due to the higher mobility of electrons.

When the external resistance is too high and the current is limited to less than 1 μA, the ionization is very weak and does not emit any light. This type of discharge is called the Townsend dark discharge. For higher pressures (≥1 atm) and low external resistance, the discharge turns into a narrow columnar glow accompanied by excess heat dissipation that can destroy the glass tube. This is an arc discharge and is used in arc welding due to the high temperatures. An arc discharge is sustained by currents greater than 1 A. At high pressures and large electrode separations, a spark discharge is produced when sufficiently high voltage is applied. The spark discharge comprises of multiple glowing plasma channels that connect the two electrodes. Spark discharges are

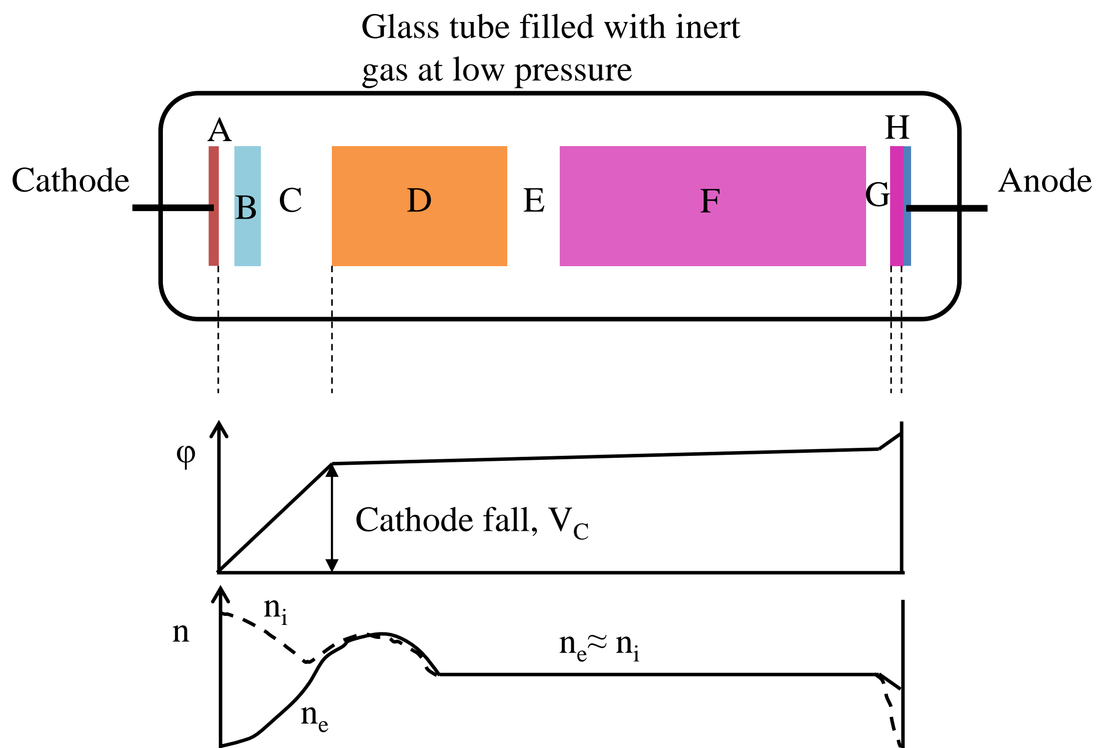

Fig. 2.1. Schematic of a basic experimental setup required to obtain a plasma discharge. The discharge occurs as alternate bright and dark regions at low pressures. The regions are Ashton dark space (A), cathode glow (B), cathode dark space (C), negative glow (D), Faraday dark space (E), positive column (F), anode dark space (G), and anode glow (H). φ and n plots show the distribution of voltage and carrier concentrations along the interelectrode space. A majority of the applied voltage drops across the cathode dark space, which is formed by a sheath of positive ions. The ionic concentration in this region is much greater than the equilibrium electron and ion concentrations.

commonly observed in automobile spark plugs and tasers. Lightning is a form of spark discharge. When the electrode separation is too large for the field to breakdown the gas within, a corona discharge occurs. The corona discharge is accompanied by small glowing areas surrounding each electrical lead. This is due to the intense electric field at the end of the leads that locally ionizes the gas in the immediate vicinity of the electrode. The microplasma transistors in this work used Townsend dark discharge and glow discharge plasmas.

2.2.1 Laws of electrical gas breakdown

A good understanding of the conditions and parameters that produce a stable discharge is essential to ensure reliable operation of the microplasma transistors. A mathematical criterion for a gas breakdown was first proposed by Townsend, which explains the initiation of breakdown in gas by an avalanche process. The avalanche process is initiated by random electrons present in the gas. These random electrons produce more electrons by impact ionization when accelerated by an electric field. The electrons thus produced accelerate towards the anode. Different loss mechanisms that include electron loss and electron energy loss affect the avalanche growth. Electrons can be lost to surroundings by diffusion and attachment to electronegative gases. The loss of electron breaks the avalanche chain. Electron energy loss could be due to elastic and inelastic collisions with neutral gas molecules. When the electric field strength approaches a certain "threshold," the electron production is significantly enhanced due to higher kinetic energy of electrons that reduces the transit time to the anode. The number of ionizing collisions produced by these individual electrons on their transit to anode is Townsend's first ionization coefficient. However, this process alone cannot produce a gas

breakdown and is assisted by a secondary process. The ions produced by impact ionization are accelerated towards the cathode. These ions bombard the cathode and cause electron emission from the cathode. The electrons thus produced acquire greater kinetic energy while accelerating to the anode, compared to electrons produced midway between the electrodes. The number of electrons produced at the cathode by an ionizing collision in the gas is termed as Townsend's second ionization coefficient. Although the breakdown process seems like a slow and gradual process, in reality it requires less than 10 ns with the right electric field strength. The current conducted by the gas during the breakdown process is given as

$$I = \frac{I_0 e^{\alpha d}}{1-\gamma\left(e^{\alpha d}-1\right)} \tag{2.1}$$

where I_0 is the current due to random electrons, α is Townsend's first ionization coefficient, γ is Townsend's second ionization coefficient, and d is the interelectrode separation. As long as the denominator is positive, the current is dominated by the primary ionization process and increases gradually with the applied electric field. When the denominator approaches 0, the equation becomes meaningless as I approaches ∞. This is the criteria for gas breakdown and is named after Townsend. At this stage, the electric current through the circuit is limited by the external resistance and charge recombination in the gas.

The transition from a steady ionization current to a gas breakdown is very rapid and depends exponentially on the applied electric field. The "threshold" electric field/voltage required for a gas breakdown depends on various factors that include the interelectrode gap, gas pressure, and cathode material. The mathematical equation for the

gas breakdown voltage was empirically determined by Paschen and is unique for a given gas. The equation produces the well-known Paschen curves and is given as

$$V_{BD} = \frac{B(pd)}{ln\left(\frac{A}{ln(\gamma+1)}\right)+ln(pd)} \tag{2.2}$$

where A and B are constants for a given gas, p is the gas pressure, d is the interelectrode gap, and γ is Townsend's second ionization coefficient. γ is typically of the order of 0.01–0.1 and depends on the cathode material. Fig. 2.2 plots Paschen's curves for breakdown voltage in different gases assuming γ of 0.01. The breakdown voltage is plotted as a function of the (pd) product. The gas pressure and the interelectrode gap have a major effect on the gas breakdown voltage.

As evident from the graph, every gas has a minimum breakdown voltage for a certain value of (pd), outside which the breakdown voltage increases exponentially. The effect is still valid when either p or d is kept constant. This phenomenon can be understood analytically by considering the effect of p and d on the mean free path of the electrons in the interelectrode gap. For simplicity, consider the case where d is kept constant. For high values of p, the number density of the gas molecules is large, which reduces the mean free path of the electrons significantly. Due to this, an electron undergoes several collisions on its transit to the anode losing its kinetic energy at every collision. The loss of kinetic energy reduces the ionization efficiency of the electrons. The external voltage has to be increased to compensate for this loss and achieve breakdown. At very low pressures, the number density of the gas molecules is reduced. This increases the mean free path of the electrons significantly, sometimes even spanning the entire length of the interelectrode gap when the gap is small. Under this condition, the

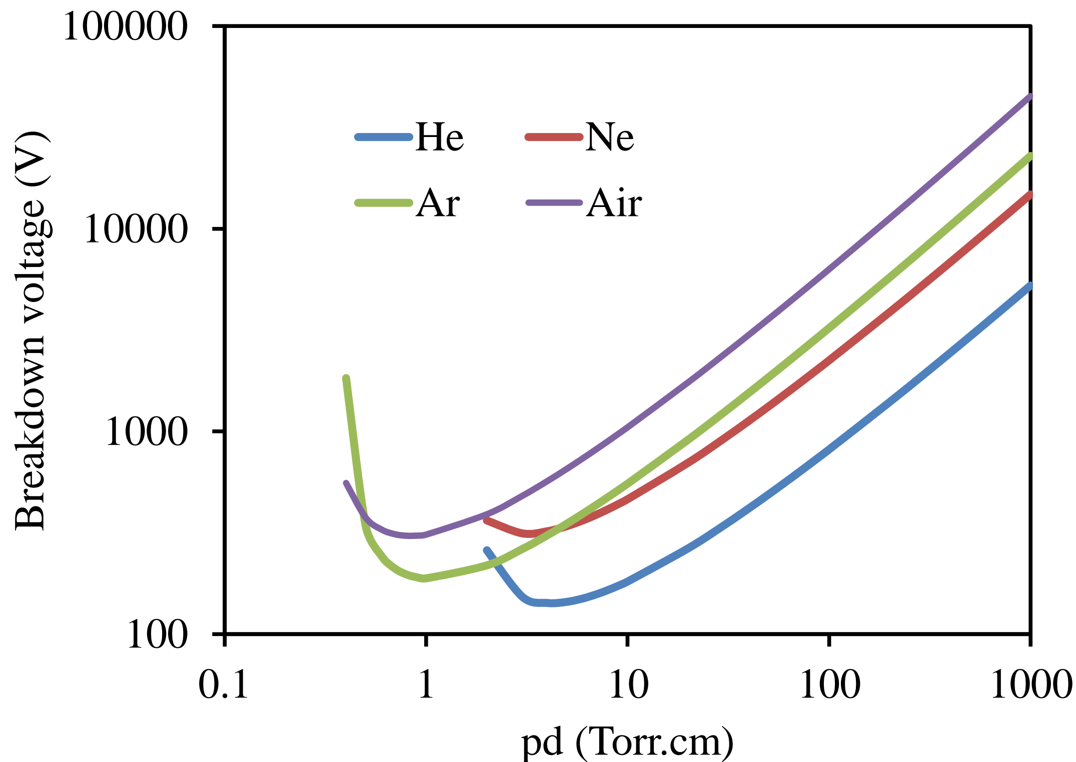

Fig. 2.2. Plot of the breakdown voltage of He, Ne, Ar, and air for different values of the gas pressure (p) and the interelectrode gap (d).

primary electrons do not interact with enough neutral gas molecules to produce sufficient ionization. An increase in the external voltage can compensate for this by increasing the ionization efficiency of the individual electrons and also the ions bombarding the cathode.

Similar understanding can be obtained for the case when p is kept constant and d is varied. In either case, the most important thing to note is the presence of an optimum value of p or d at which the breakdown voltage is minimum. The practical use of this concept can be observed in the reactive ion etching and sputtering machines, where the plasma is ignited at low pressures to achieve low breakdown voltage. Paschen’s curve is an important tool to determine the breakdown voltage of a given system with a good accuracy. However, it fails at very low and very high pressures/gaps because it does not

account for other secondary effects such as field emission and cathode surface conditioning. The dimensions of the gap in the microplasma transistor used in this work is less than 5 μm and falls well below the valid (pd) values of the Paschen curve. Hence, some modifications are needed in the Paschen's curve equation to reinstate its validity at these dimensions. The modifications will be discussed in detail in Chapter 4.

2.3 Microplasma field effect transistor

The working principle of a MOPFET can be understood by building on our understanding of the plasma discharges from previous sections. The central functional element of the MOPFET is the microplasma. From the previous sections it is established that there are two electrodes necessary to pass current through a gas and generate plasma. The source and drain electrodes serve this purpose. The drain-source voltage (V_{DS}) is maintained at a constant value sufficient to generate and sustain the plasma. This establishes a steady current through the drain-source that is composed of both electrons and ions. V_{DS} could be a dc voltage or an rf voltage. The contribution of ionic current is greater for a dc voltage compared to rf voltage. At dc voltages and rf frequencies lower than ~50 kHz, the ions respond to the oscillations in the voltage. At frequencies greater than this, the ions fail to respond to the oscillations due to their heavier mass, and the current is almost entirely due to electrons. For the same reason, the contribution of ionic current to the total current in a dc excited plasma is significantly lower than the electronic current. The important parameters to consider for plasma generation are the gas pressure and the drain-source gap. The choice of gas is also important if a low breakdown voltage is desired. Helium was chosen for most of our experiments due to its lower breakdown voltage. The devices in this work were operated at atmospheric pressure to obtain higher

charge densities in the plasma. The atmospheric pressure operation also helped to confine the plasma within the electrodes (plasma gets rarefied at lower pressures). The drain-source separation was less than 5 μm, with the smallest devices having a separation of just 1 μm. The drain-source current is modified by applying a voltage on the gate electrode. The voltage on the gate changes the density of electrons in the plasma that inturn changes the drain-source current. For a negative bias, the gate pushes electrons into the plasma. These electrons include the ones that diffused away from the plasma region and also some electrons that were emitted by the gate through field emission resulting from the strong electric field inside the plasma. Due to this, the drain-source current increases. Conversely, for a positive gate voltage, the gate absorbs the electrons away from the plasma and results in a reduced drain-source current. The MOPFETs were tested thoroughly with both dc and rf excitation, the results of which will be presented in Chapters 4 and 5. Fig. 2.3 shows a detailed graphical representation of the working principle of a MOPFET. Although the drain, source, and gate are represented by different colors, they were all fabricated with the same material.

This chapter discussed the plasma generation mechanism through electrical breakdown of the gas. The important parameters that affect the plasma generation include gas pressure, interelectrode spacing, and the cathode material. The invalidity of the Paschen's curve at micron-gaps calls for a new/modified theory of electrical gas breakdown, which is presented in the next chapter. The choice of cathode material is in fact a very important parameter that affects the longevity of the MOPPETs. Chapter 3 discusses the reasoning behind the choice of material.

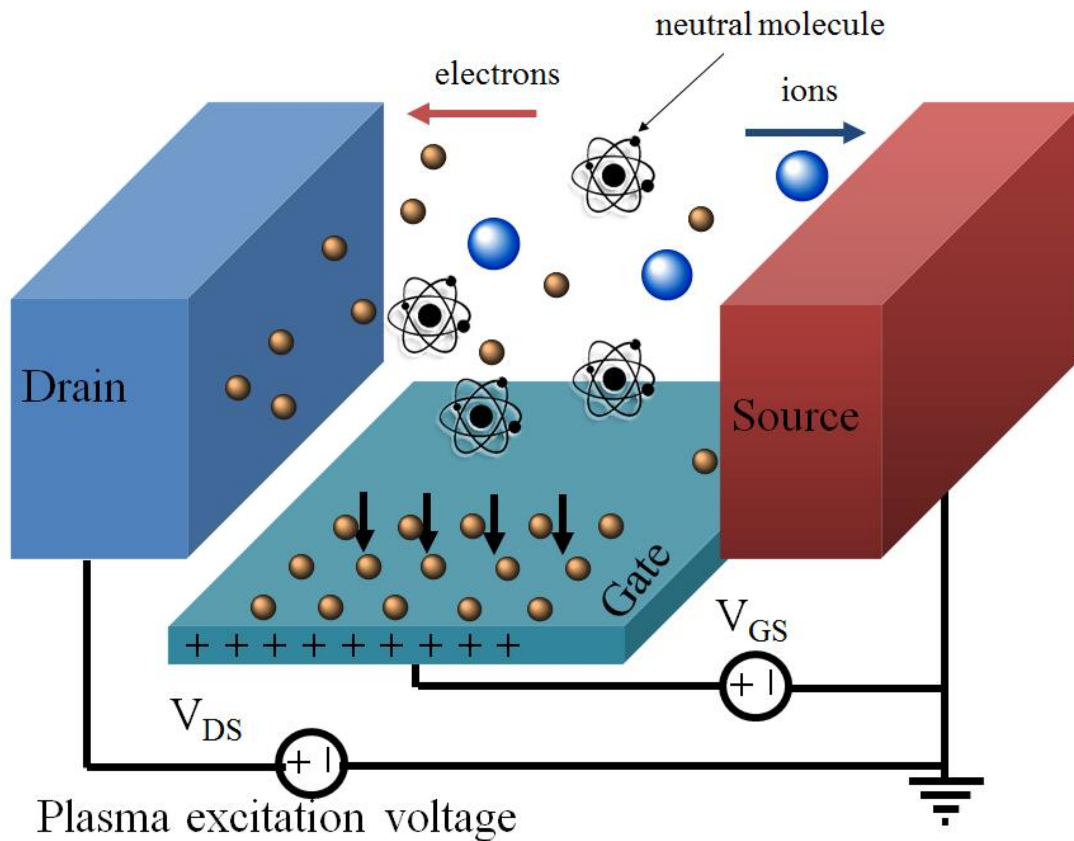

Fig. 2.3. Schematic showing the working principle of a MOPFET. The plasma is generated by the drain-source voltage. The gate voltage modulates the drain-source current by modifying the electron density in the plasma.

CHAPTER 3

FABRICATION

The fabrication process of the microplasma transistor is fairly simple and straightforward. However, the harsh conditions in plasma require use of robust materials to sustain the plasma and provide the transistors with a reasonably good longevity. This chapter discusses the logical reasoning followed in the choice of materials and the micromachining processes employed to fabricate the transistors.

3.1 Material selection

Plasma is the heart of a microplasma transistor. The insensitivity of plasma to high temperatures and ionizing radiation are advantageous to the operation of the transistor. The partially ionized plasma in the microplasma transistor typically has temperatures in the range of several hundred degrees Celsius depending on the gas pressure, plasma density, and the current density through the plasma. The gaseous state of the “active” region in the transistor is unaffected by the elevated temperatures in the plasma. However, the electrodes that generate and sustain the plasma are solid and are affected by elevated temperatures in different ways. The most obvious effects are softening, thermal expansion, and manifestation of residual stress along the cross section. Apart from the high temperature, plasma is also equipped with energetic ions that can sputter the electrode material. Considering these factors, one can list several desirable

properties that should be expected in a material qualifying for the electrodes. The following are some important properties of a potential electrode material that will ensure its longevity

- High melting temperature much greater than the plasma temperature
- High density to minimize the sputtering damage
- Good thermal conductivity to carry the heat away from the electrode tips
- Low thermal expansion coefficient to prevent expansion of the electrode layer

High thermal conductivity and low thermal expansion coefficient also prevent buildup of residual stress along the cross section by avoiding temperature gradients along the cross section. Besides these, there is an additional requirement that can be understood by considering the structure of the microplasma transistor. The structural design of the transistor will be discussed in detail in a later section of the chapter. For the current discussion it is sufficient to mention that the electrode(s) are in the form of a beam supported by an anchor. For reproducible switching, the electrodes have to remain fixed in their position as the switching (breakdown) voltage is sensitive to the mutual positioning of the electrodes. Thus, it is desirable to use a material with a high elasticity that does not comply easily, which is reflected by its Young's modulus. Based on all these requirements, a figure of merit (FOM) was defined as

$$FOM = \frac{\gamma.10^9}{E.\rho.M.\alpha} \tag{3.1}$$

where γ is the thermal expansion coefficient, E is the Young's modulus of elasticity, ρ is the material density, M is the melting point in °C, and α is the thermal conductivity. A good electrode is expected to have a low value of FOM. Table 3.1 lists the properties of

Table 3.1. Properties of some common materials used in microfabrication considered as potential candidates for the MOPFET electrodes. Tungsten is the material of choice due to its low FOM.

Material	E [GPa]	ρ [g/cm^3]	M [°C]	α [W/mK]	γ [10^{-6}/K]	FOM
Aluminum	70	2.7	660	237	24	811.82
Chromium	279	7.19	1907	93.9	4.9	13.64
Copper	128	8.96	1084	401	16.5	33.10
Platinum	168	21.45	1768	71.6	8.8	19.29
Poly-Si	188	2.3	1414	149	2.6	28.54
Tantalum	186	16.6	2996	57.5	6.5	12.22
Titanium	166	4.5	1668	21.9	8.6	315.16
Tungsten	411	19.25	3422	175	4.5	0.95

some common materials used in microfabrication along with their calculated FOM. Based on these FOMs, tungsten seems to be the best choice. Tungsten is a good refractory material and is well known for its physical hardness.

3.2 MOPFET physical design

The physical components of the MOPFET are similar to a MOSFET, comprising the source, drain, gate electrodes, and an active region. The use of a solid active region in the MOSFET allows a planar geometry, with the current conduction occurring through the substrate. In a MOPFET, the gaseous active region requires the use of three-dimensional electrode structure capable of ionizing the gas and controlling the degree of ionization. Similar to all microplasma devices, the MOPFET requires a cavity where a finite volume of trapped gas is ionized. The cavity in a MOPFET is formed between the source and drain electrodes. The gate can be positioned either on the top or bottom of this cavity and placed symmetrically with the source-drain electrodes. Fig. 3.1 shows schematics of two different designs of the MOPFET with the gate situated at the top (Fig. 3.1 a) and bottom (Fig. 3.1 b) of the cavity. Both these variations of the MOPFET

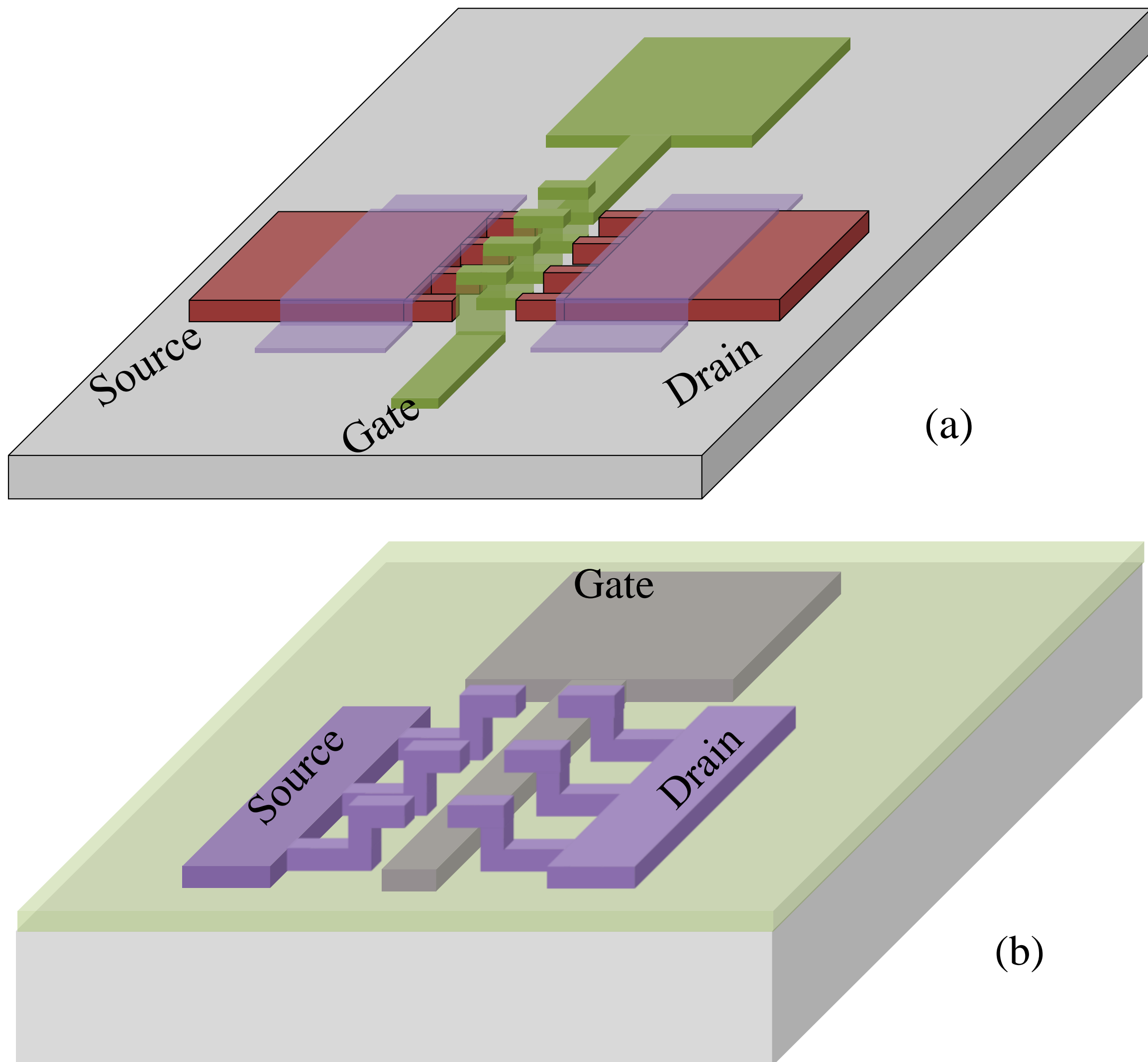

Fig. 3.1. Schematics of the two different MOPFET designs showing the source-drain cavity. (a) shows a MOPFET with the gate electrode positioned on top of the cavity. (b)[3] shows a MOPFET with the gate positioned at the bottom.

[3] P. Pai and M. Tabib-Azar, "Microplasma field effect transistors operating with dc plasma," *IEEE Electron Dev. Lett.*, vol. 35, pp. 593–595, 2014. © 2014 IEEE.

performed similarly on the electrical switching characteristics. However, there were other factors that affected the operation of these devices that favored one design over the other. This will be discussed in detail in the next section. Apart from these broad variations in the design, there were variations made to the width of the source-drain. For widths larger than 10 μm, the source-drain electrodes were distributed into multiple fingers. The purpose of this was to prevent long suspensions of gate electrode in the "top-gate" design (Fig. 3.1a) that would increase its compliance. The same rule was applied to the "bottom-gate" design to facilitate better gas flow through the cavity. The large square pads at the end of the electrodes served as both electrical contact pads for the electrodes and heat sinks to conduct heat away from the narrow electrode tips.

3.3 Fabrication techniques and challenges

The MOPFETs were fabricated with conventional micromachining techniques. The fabrication process was developed and optimized over several iterations that required resolving problems faced during the fabrication as well as testing. The ultimate goal was to develop devices with the required design and ensure longevity of these devices during operation. As discussed in the earlier section, there are several factors that affect the operating span of a device, and optimizing the performance of the device required modifications in the fabrication process.

The MOPFET requires a nonconducting substrate due to the device structure. Oxidized silicon wafer would be the first preference due to the popularity of using silicon wafers in microfabrication. However, the MOPFET uses 100s of volts of excitation and requires a very thick (>1 μm) silicon dioxide layer to prevent dielectric breakdown and minimize leakage currents. The growth time of silicon dioxide has an exponential relation

with the thickness, and growing ≥1 μm requires more than 6–7 hours of oxidation in a high temperature furnace, which is not cost effective. A good alternate would be to use a glass wafer. Therefore, the MOPFETs were fabricated on a glass wafer.

Tungsten was the first choice of material for electrodes. The most common deposition techniques for metals is by sputtering and evaporation. Due to its high melting temperature, it is more convenient to deposit tungsten by sputtering. Metals are mostly used as contact pads in MEMS devices and ICs, due to which they are usually deposited in thin layers (100–200 nm). The depth of the cavity in a MOPFET is defined by the thickness of the source-drain electrode. It is necessary to have a >500 nm thick source-drain to create reasonably deep cavities that can enclose an appreciable volume of gas for ionization. Deposition of thick materials by sputtering and evaporation is also accompanied by a buildup of residual stress due to mismatch in grain size and thermal expansion coefficients, and tungsten is no exception. Tungsten was found to develop severe residual stress in the range of a few giga Pascals, sufficient to crack the film. Shen et al. [13] discovered a relation between the residual stresses developed in sputtered tungsten with the deposition gas pressure. According to their results, the residual stress in the tungsten film varied almost exponentially with the deposition pressure. At pressures below 30 mTorr, the residual stress switched sharply from compressive to tensile with the transition occurring around 15 mTorr. For pressures above 60 mTorr, there was no residual stress observed. They attributed the variations in residual stress to the grain size change that depended on the gas pressure. However, their film thickness was limited to 150 nm. The tungsten film thickness used in this work was ≥1 μm. The film was sputtered using the Denton Discovery 18 sputtering system at 15 mTorr Ar pressure and

200 W dc power on a 4" glass wafer. The films developed severe tensile stress (> 1 GPa) after deposition and cracked in most cases. Through careful iterations and examinations, the cause of the problem was found to be due to heating caused by continuous sputtering and also the thermal shock on the film when the wafer was exposed to room temperature immediately after sputtering. During sputtering, some of the external dc power dissipates as heat and is transferred to the wafer. The heat transferred increases with the duration of sputtering. At 200 W, it takes ~40 min to sputter a 1 μm thick layer. At low pressures of 15 mTorr, there are not enough gas molecules to exchange heat from the glass wafer. Thus, the wafer can heat to a few hundred °C. The effect of heat can change the grain structures that affect the stress characteristics [14]. In addition to this, exposing the wafer to room temperature immediately after sputtering subjected it to a thermal shock that cracked the film.

To minimize the heating, the deposition was performed in steps of 5 min with a 5 min cool down step after each deposition, where the dc power was turned off. The wafer was also allowed to cool down in the vacuum chamber for 30 min after sputtering before exposing it to atmospheric pressure. Despite these improvisations, the stress was still significant (>500 MPa) and cracked the film. To solve this problem an alternate material was considered to replace tungsten. TiW is an alloy with 10% composition of titanium and 90% tungsten and has roughly the same physical properties as pure tungsten. The interval deposition technique was tested with TiW, which produced much lesser stress on the film (<100 MPa), and there was no more cracking observed. The interval deposition technique allowed deposition of up to 2 μm thick TiW films with residual stress less than 100 MPa. This technique was also used to produce stiff beams for MEMS resonators

[15].

The fabrication sequence of the MOPFET is explained as follows. The procedure described here was used to fabricate the device shown in Fig. 3.1b. The same set of processes can also be used fabricate the device shown in Fig. 3.1a by rearranging the sequence. A 4" glass wafer was cleaned in piranha. Then a 700 nm thick TiW layer was sputtered and patterned by an Oxford 80 Reactive Ion Etching (RIE) system to form the gate electrode (Fig. 3.2a) using photoresist S1813 as the etch mask. TiW was etched with a mixture of SF_6, Ar and O_2 in the ratio 25:10:3.5 sccm at a pressure of 10 mTorr and 200 W rf power. A 100 nm thick layer of Al_2O_3 was then deposited on the wafer by a Cambridge Fiji 200 Atomic Layer Deposition (ALD) system at 250 °C to insulate the gate (Fig. 3.2b). 700 nm poly-Si was then sputtered and patterned by RIE to form a sacrificial layer (Fig. 3.2c). The poly-Si was etched with a mixture of SF_6 and O_2 gas in the ratio 25:3.5 at 50 mTorr and 200 W rf power. The source/drain electrodes were then formed on top of this by sputtering and patterning a stack of Cr (100nm), TiW (500nm), and Cr (100 nm) (Fig. 3.2d). The Cr layer was wet-etched with CR-17 chrome etchant. Cr was used to prevent direct exposure of TiW to XeF_2 gas, which was used to etch poly-Si and release the source/drain electrodes (Fig. 3.2e). Before the release, the Al_2O_3 layer on top of the gate bonding pad was etched away in buffered HF. The gate width was intentionally designed to be larger than the source-drain gap by 4 μm to accommodate any misalignment. Source-drain gaps ranging from 1 to 6 μm were designed; fabricated devices varied slightly in dimension due to etch nonuniformity across the wafer.

There were two major challenges in the fabrication that prevented patterning of narrow (< 3 μm) source-drain gaps. The first limitation was posed by the mask pattern

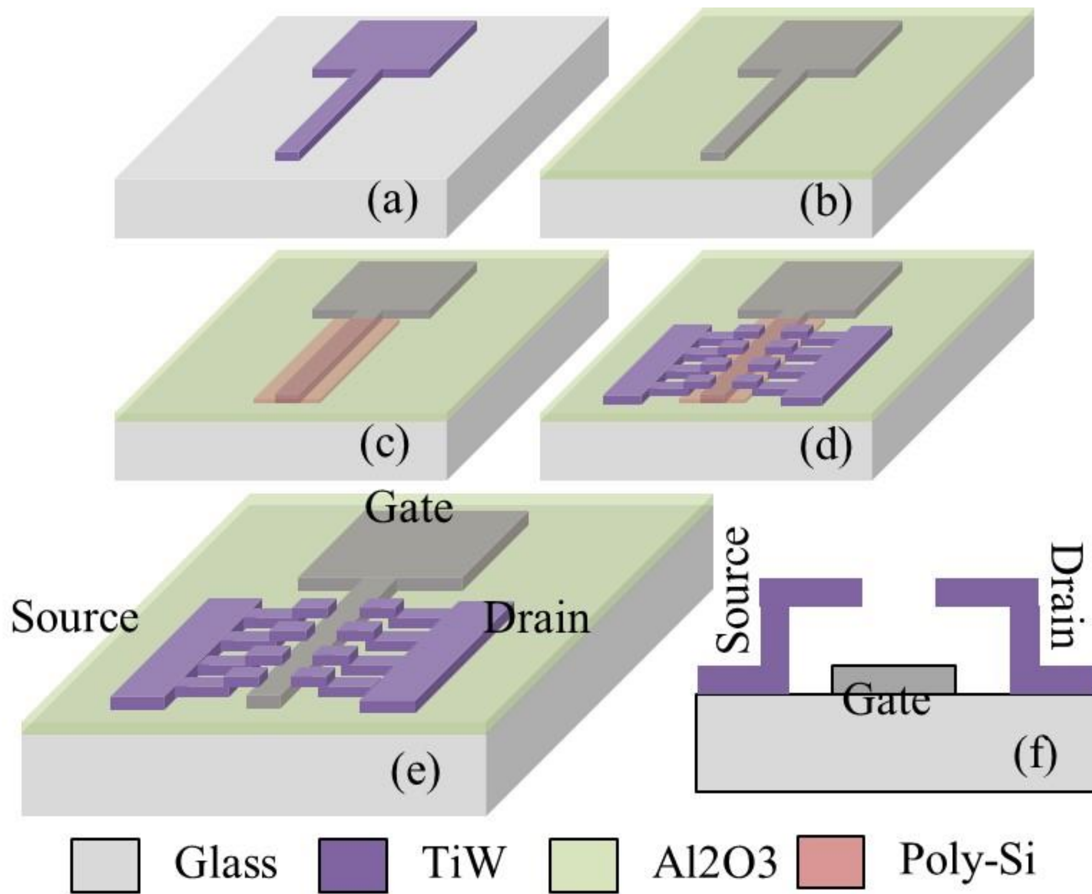

Fig. 3.2. Schematic representation of the fabrication process of the MOPFET shown in Fig. 3.1b. (a) shows the patterned gate. (b) shows the wafer after gate-oxide deposition. (c) shows the patterned poly-si sacrificial stub. (d) shows the patterned source-drain electrode. (e) shows the final device after etching the sacrificial layer. (f) shows the cross sectional view of the MOPFET.

generator that had a resolution limit of 3 μm. Despite drawing a 1 μm gap on the mask layout, the gap expanded to 3 μm when the mask was developed. A Heidelberg MicroPG 101 pattern generator was used to pattern the masks. The narrow gaps were created by a combination of developing and etching. Due to the limited resolution of the pattern generator it exposed a wider area even for smaller gaps. However, the photoresist in the whole gap width did not develop at the same rate due to its geometry. A partially developed (~75%) gap had a nonrectangular cross section as shown in Fig. 3.3b. Continuing the developing further eventually removed the photoresist from the corners and created a rectangular cross section. However, treating the photoresist to O_2 plasma for a short duration (~30 sec) etched down the whole photoresist uniformly with a preferential etch in the vertical direction due to the nature of RIE. By carefully timing the O_2 plasma etch, gaps much narrower than the actual exposed area were opened up as shown in Fig. 3.3c. This technique was used to create gaps smaller than 3 μm. The technique can be used in general with photolithography to create small gaps.

The second challenge in the creation of narrow gaps was in transferring the pattern from the mask to the TiW layer. Due to the relatively large thickness of the TiW layer, liftoff was not feasible. The challenge with etching was in minimizing the undercut that can widen the gap size. The undercut gets worse with thicker layers. This ruled out the wet etching. RIE is a good option. SF_6 and CF_4 plasmas are preferred etchant gases for tungsten due to their high etch rates [16]. However, these gases cause severe undercuts despite the anisotropic nature of RIE. Reyes-Betanzo et al. found a way to reduce the undercuts significantly by introducing Ar gas to the SF_6 plasma [17]. The etching pressure was optimized to 10 mTorr in this work to obtain minimum undercut

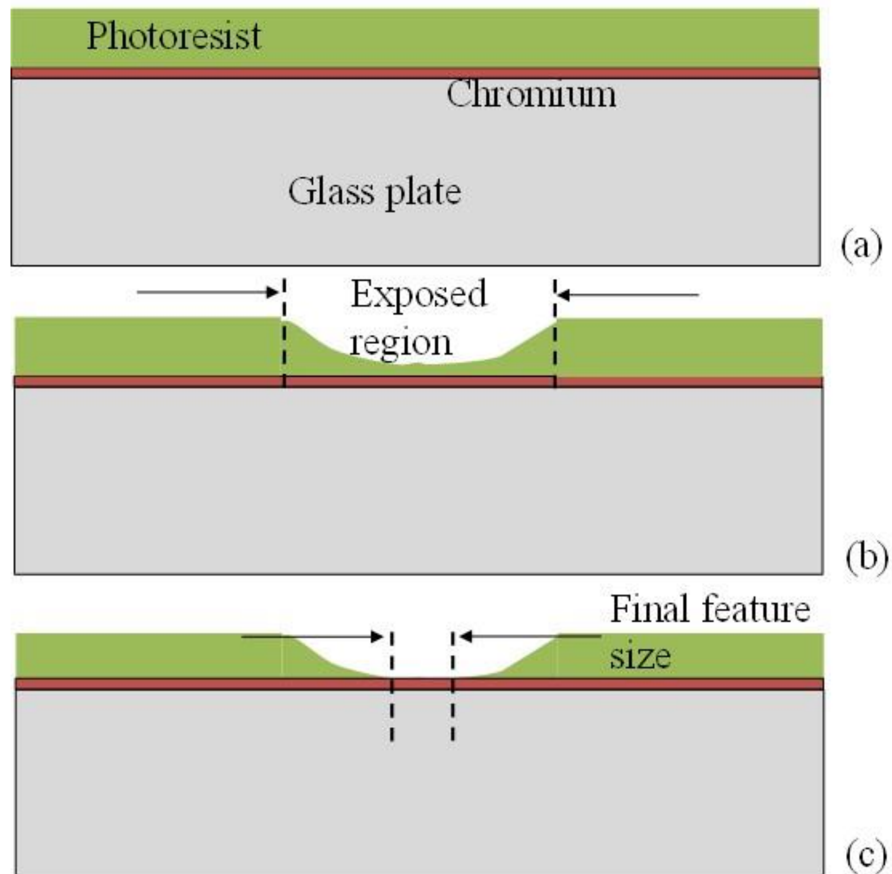

Fig. 3.3. Schematic of the photomask cross section through the development process. (a) shows a fresh photomask. (b) shows the partially developed mask. (c) shows the mask after a short treatment to O_2 plasma to open up narrow gap.

and have a reasonable etch rate.

Lastly, there was a minor problem in etching the bottom Cr layer in the source-drain electrode stack after etching the TiW layer. The TiW etching with SF_6 and Ar plasma developed a passivation layer on the bottom Cr layer that reduced its reactivity to the CR-17 etchant significantly. The prolonged etch time required to pattern the bottom Cr layer caused severe undercut in the top Cr layer as shown in Fig. 3.4a. Treating the bottom Cr layer to buffered HF before the CR-17 etch removed the passivation layer and improved its etch rate in CR-17. This prevented undercut on the top Cr (Fig. 3.4b).

After fabrication, the wafer was diced into rectangular dies. The devices were then wire-bonded to a hybrid package for testing. The package was partially sealed with a plexiglass plate and supplied with He gas. The package was maintained at atmospheric pressure. He was supplied at a gentle flow rate to prevent turbulent flow. Fig. 3.5 shows a picture of the device during operation.

The packaged devices were tested electrically to compare the performance of the “top gate” MOPFET against the “bottom gate” MOPFET. The first task in electrical characterization was to establish plasma within the device between the source-drain electrodes. Both dc and rf excitations were tested. The dc excitation damaged the cathode severely due to ionic sputtering, and the effect was observed in both “top gate” and “bottom gate” MOPFETs. Fig. 3.6a shows the SEM image of the source-drain electrodes of a MOPFET that was excited with dc voltage. The damage to the cathode is very evident in the image. The severity of the damage depended on the magnitude of the current density through the electrodes and the duration of device operation. For currents above 50 nA, the cathode electrodes were sputtered away instantly in large chunks and

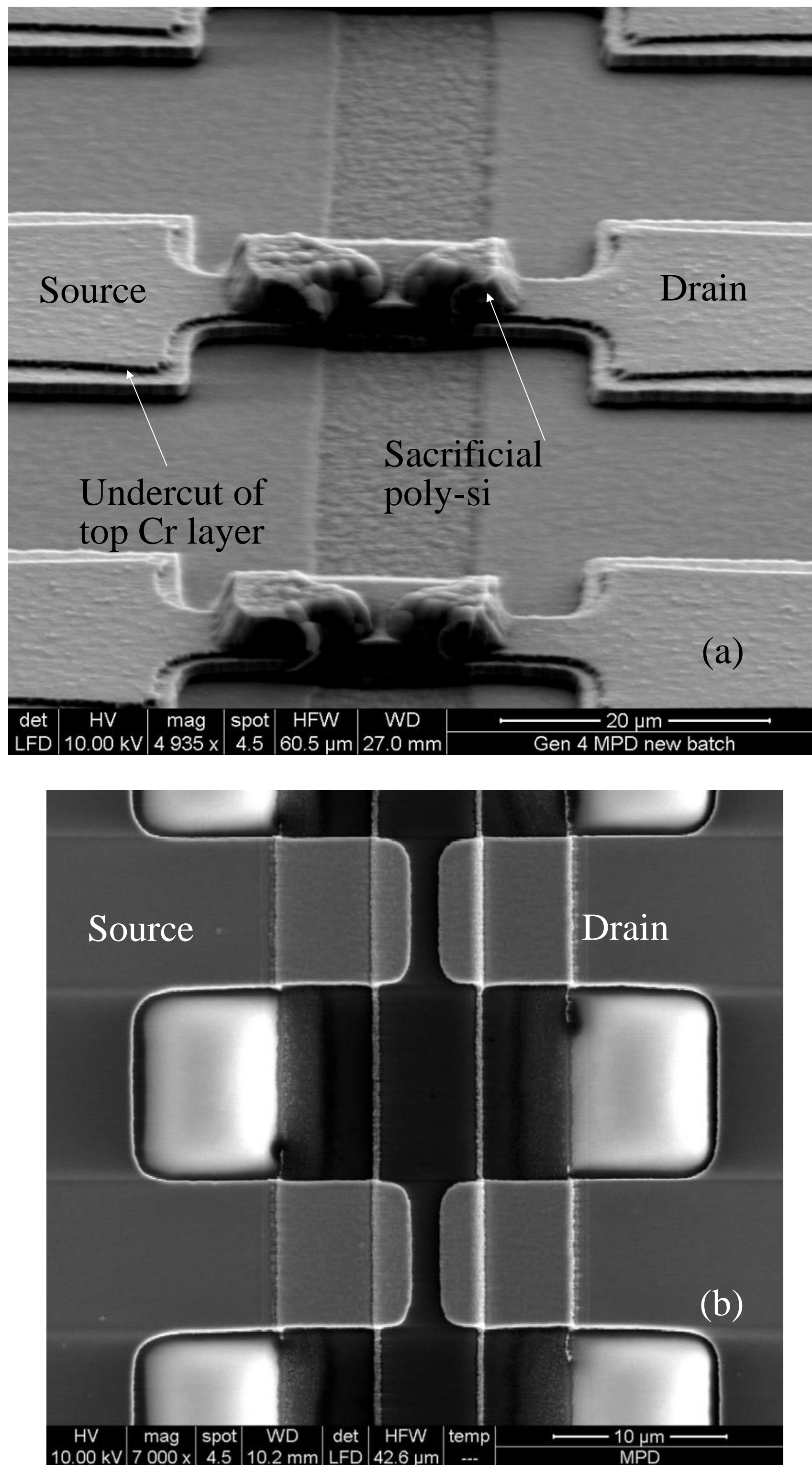

Fig. 3.4. SEM image of a MOPFET after source-drain electrode patterning. (a) shows a device with "top gate" design after the sacrificial silicon patterning. The top Cr layer on the source-drain electrodes show sever undercut. (b) shows a device with "bottom gate" design. There was no more undercut after treating the bottom Cr layer to buffered HF.

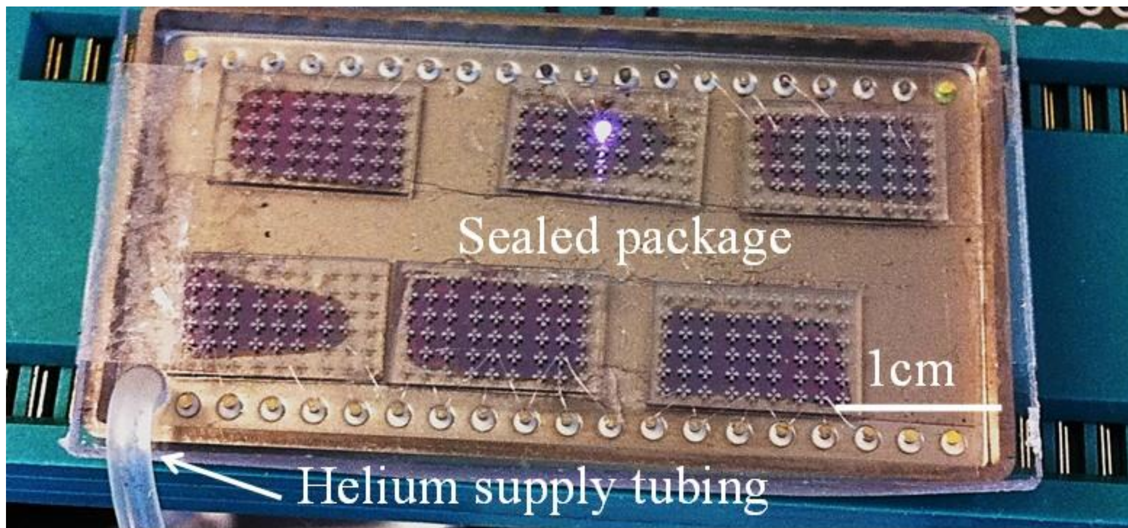

Fig. 3.5. Photograph of the device during operation showing the hybrid package used for electrical connection.

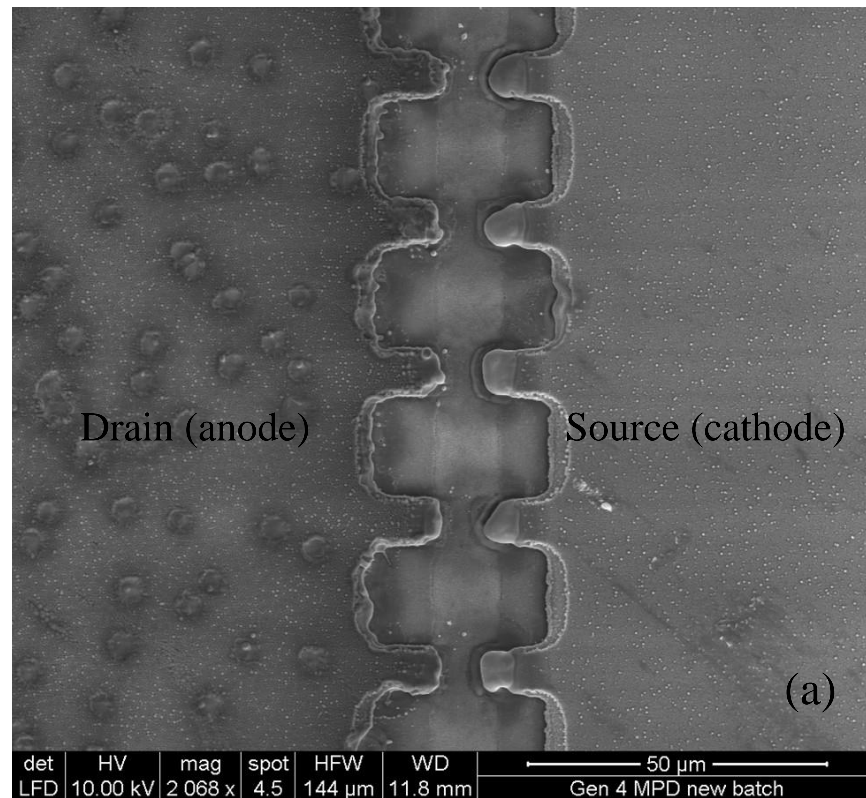

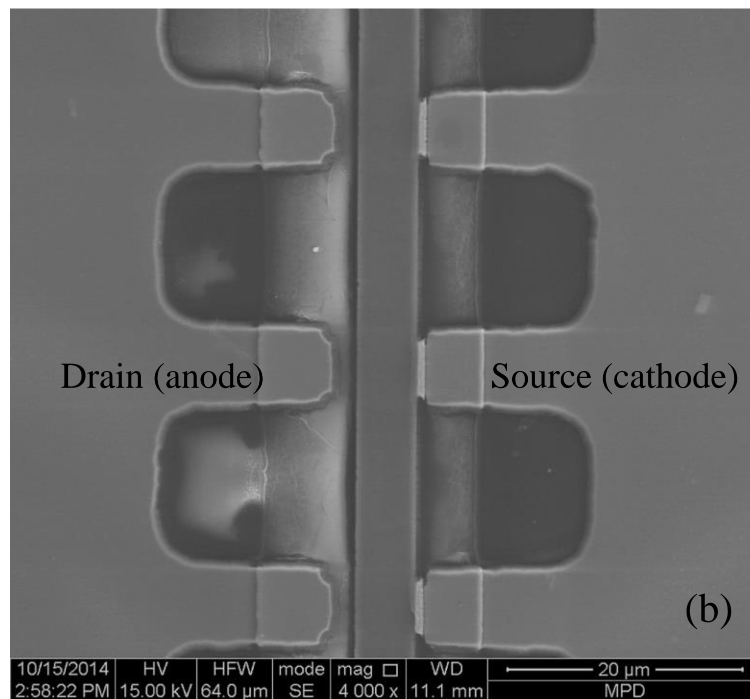

Fig. 3.6. SEM image of the source-drain electrodes of a MOPFET after plasma generation. (a) shows a device that was excited with dc voltage at 10 nA current for 1 min. The cathode is severely damaged due to ion sputtering. (b) shows a device that was excited with rf voltage at ~100 μA current for ~10 min.

destroyed the device completely. Thus, dc testing was done with very small currents. On the other hand, the MOPFET could handle significantly higher currents (up to 100 μA) with minimal damage to the electrodes while using rf excitation (Fig. 3.6b). To test the device lifetime with continuous operation, plasma was generated between the source-drain using rf excitation and allowed to sustain the plasma till the device failed. A low frequency pulse was applied on the gate to modulate the plasma current, which in turn modulated the intensity of the plasma glow. The device operation was recorded on a video camera continuously.

The first signs of failure were observed in the “top gate” MOPFET that started losing gate control after less than an hour of continuous operation. The device failed completely after some time and showed an electrical short between the source and drain. However, this problem was not observed in the “bottom gate” MOPFETs, and they operated continuously for more than 20 hours and switched off only when the gas supply tank ran out. The SEM of the failed MOPFET had surprising details that showed islands of metal where the gate used to be (Fig. 3.7a). These islands had shorted the source-drain electrodes at some places, which explained the shorting. The gate electrode had melted/softened and broken into segments/islands due to the surface tension that developed. This was surprising considering that the melting temperature of TiW is above 3000 °C, and glow discharge plasma has temperatures typically less than 1000 °C. The only plausible explanation for this is that a thin film material behaves differently compared to its bulk form. The melting point specified for a material is usually considering it in the bulk form, unless specified otherwise. The phenomenon has actually been observed in the past and explained in detail through careful material characterization

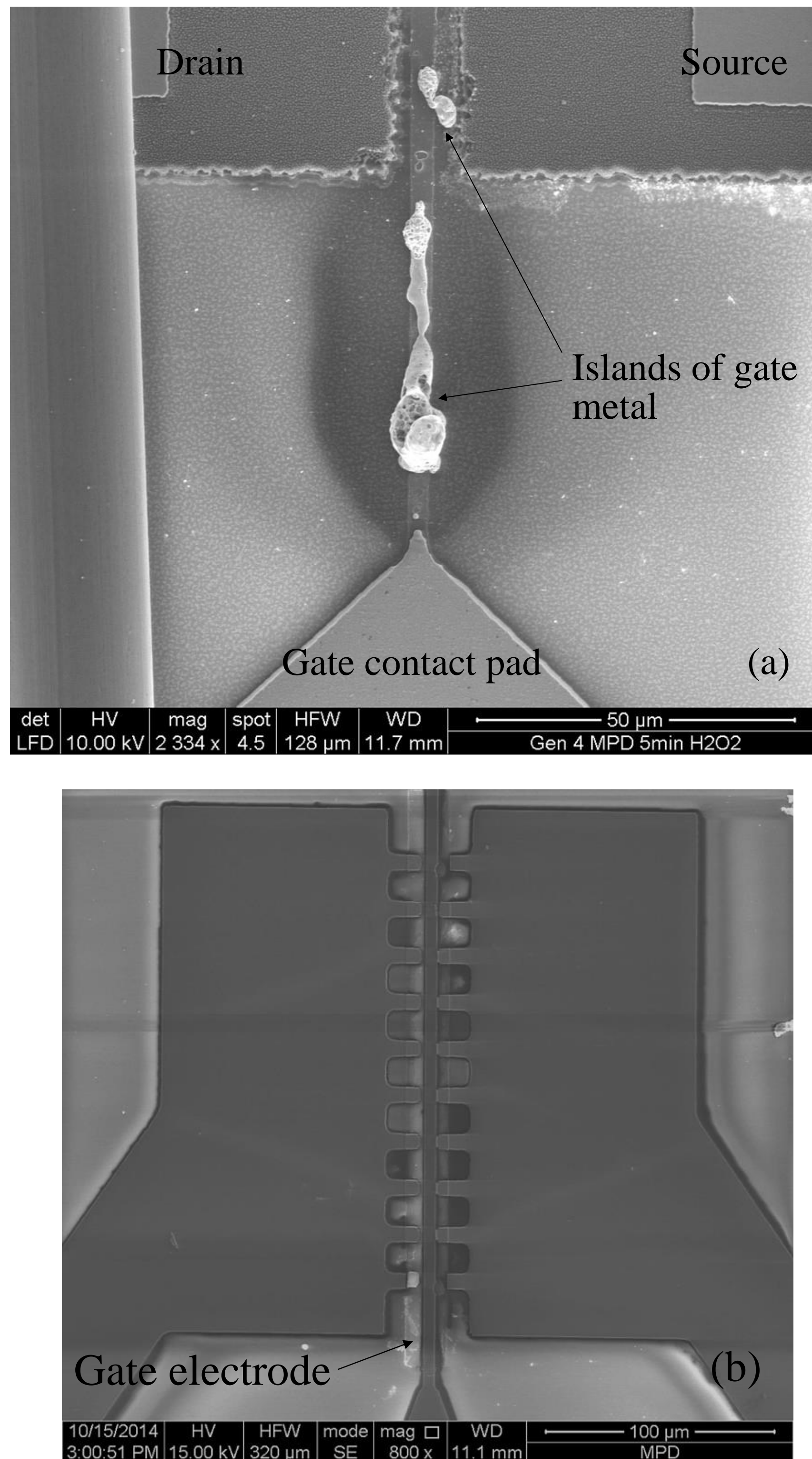

Fig. 3.7. SEM image of the top view of the MOPFETs after operating with rf plasma. (a) shows a device with a "top gate" design. Excess heating of the gate electrode caused it to soften/melt and form islands. (b) shows a device with a "bottom gate" design. The gate remained intact after operating with rf plasma.

by Aubert et al. [2]. According to their observations, thin film metals tended to soften and form islands at temperatures much less than their melting point. The cause for this was attributed to the increased mobility of atoms at higher temperature, which changed the grain structure and favored clustering. While this explains the reason for failure in the “top gate” MOPFETs, it does not help in understanding why the effect was not observed in the “bottom gate” MOPFETs (Fig. 3.7b). The obvious reason for this was due to the difference in their geometric structure. A “top gate” MOPFET formed a more enclosed space where plasma was trapped. The enclosure formed a hot zone when plasma was generated, which heated up the gate electrode sufficiently enough to soften it. A “bottom gate” MOPFET has a more open cavity for the plasma, due to which the plasma could easily transfer the heat to the surrounding neutral gas molecules that were maintained at almost room temperature by continuously flowing He. For this reason, the rest of the characterizations were performed with the “bottom gate” MOPFETs. Fig. 3.8 shows the SEM of a “bottom gate” MOPFET.

The MOPFET functioned well with minimum electrode damage while using an rf excitation to generate plasma. However, there are situations where the use of dc is more preferable over rf excitation. Due to the ionic sputtering in a dc excitation, the plasma current was limited to 10 nA or less, which is too small to be of practical use. The damage to the cathode (source) was worsened by the heating of the cathode, which softened the electrode and enhanced sputter yield. The effect of softening can be deduced by the rounding of the cathode tips in Fig. 3.6. Heating was caused by the large ionic current density produced due to the small cross sectional area of the electrodes. The small cross section also slowed down the heat transfer from the electrode tips to the contact

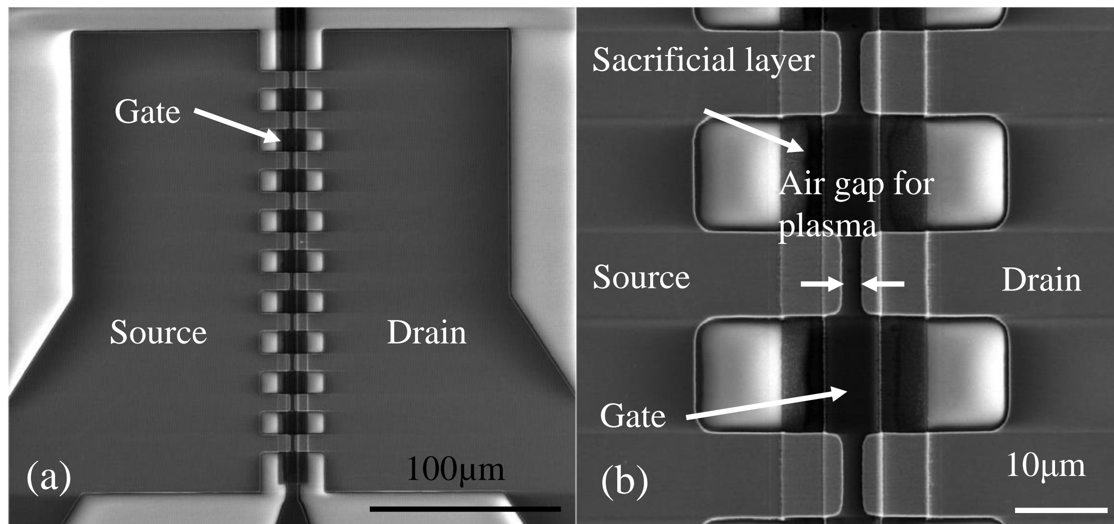

Fig. 3.8.[4] SEM images of a "bottom gate" MOPFET before the sacrificial layer etching. (a) shows a MOPFET with 10 pairs of source-drain fingers, each with a width of 10 μm. (b) shows a magnified view of the MOPFET.

pads. A solution to this problem would be to increase the thickness of the electrodes significantly. However, this cannot be done using sputtering and evaporation due to their slow deposition rates and residual stress buildup. A popular technique to deposit thick metal layers is through electroplating. Electroplating allows depositions of very thick metal layers (>100 μm) with low stress. Cu and Ni are common electroplating metals. Ni tends to develop residual stress and peel off, due to which Cu was chosen in this work. Due to the large thickness of the electroplated layer, the device electrodes were planar and fabricated with just one patterning mask. The fabrication process was simple. A 200 nm thick seed layer of Cu was sputter deposited on a glass wafer, with a 10 nm Ti layer serving as the adhesion layer. The electroplating mold was formed by patterning AZ 9260 photoresist. AZ 9260 is a thick photoresist, developed mainly for applications like electroplating that require thick molds. With a single spin coat, the resist can attain

[4] P. Pai and M. Tabib-Azar, "Microplasma field effect transistors operating with dc plasma," *IEEE Electron Dev. Lett.*, vol. 35, pp. 593–595, 2014. © 2014 IEEE.

thickness up to ~25 µm. Successive spin coats can be used to build up to 100-µm thick layers. The increased thickness comes with a trade-off of lower resolution. The minimum achievable gap in a 25 µm thick layer is ~3–4 µm. To make the best of the situation, the photoresist thickness was fixed at 25 µm, which would increase the thickness of the electrodes significantly compared to the TiW sputtered MOPFETs. Electroplating was carried out in a solution of copper sulfate using a rectangular copper plate as the anode. The electroplating was performed at a constant current density of ~3 mA/cm^2. Fig. 3.9. shows SEM images of a MOPFET and some other electrode structures used to realize logic gates. Due to the planar geometry of the electrodes, the gate electrode had to be split into two and placed orthogonally on either side of the source-drain electrodes. The electroplated devices were tested with plasma, and as expected they were more tolerant to the dc current and showed almost negligible wear even when the current was increased to up to 1 mA.

This chapter provided a detailed account of the fabrication procedure used to make narrow gap MOPFETs. The advantages and disadvantages of the device design, material choice, and fabrication schemes were discussed. The TiW MOPFETs were extensively used for characterization with both dc and rf excitations due to the small gaps achieved in them. The copper devices were mostly used in testing the logic gates. The following chapters present the detailed electrical characterization results of MOPFETs.

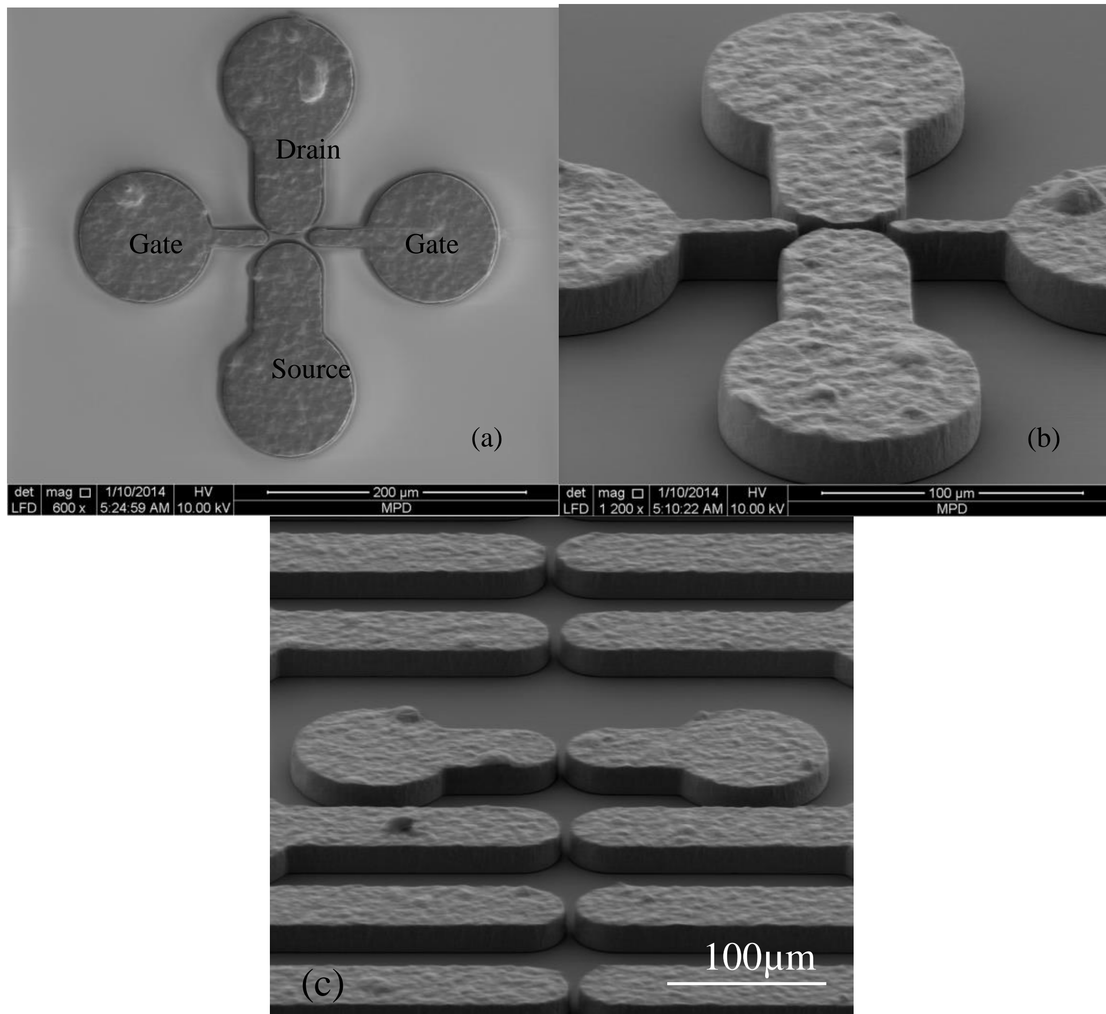

Fig. 3.9. SEM images of 25 µm thick electroplated devices. (a) and (b) show the top view and perspective view of a MOPFET. The electrodes are coplanar due to lithographic limitations. (c)[5] shows the perspective view of electrodes used in microplasma logic gates.

[5] P. Pai and M. Tabib-Azar, "Micro-plasma logic gates," *IEEE T. Plasma Sci.*, vol. 42, p. 1995–1998, 2014.
© 2014 IEEE

CHAPTER 4

MOPFET DC CHARACTERIZATION

As discussed in earlier sections, plasma devices have been used in various applications. They have been used for high power electrical switching due to their high conductance. There have been reports of microplasma transistors, but the field has not been extensively researched. All the microplasma devices reported in the past are relatively large and thereby require higher operating voltages. This work succeeds in shrinking the scale of the microplasma transistors to truly microscale (<5 μm), which can enable development of large scale integrated transistors for on-board electronics in harsh environments. This section discusses the technique of scaling down the operating voltage of the microplasma transistor and the complete characterization performed with dc excitation.

4.1 Sub-Paschen breakdown

The condition for generation of self-sustained plasma is governed by Townsend's breakdown criterion that defines the condition for the electrical breakdown of a gas. Extrapolation of the breakdown criterion leads to the Paschen's law (eq. 2.2), which relates the breakdown voltage of a gas to its pressure and electrode separation. Eq. 2.2 can be rearranged as

$$\gamma_i \left[e^{Apd\, exp\left(-Bpd/_{V_{BD}}\right)} \right] = 1 \tag{4.1}$$

where γ_i is the secondary emission coefficient for ions. The above equation produces exponentially increasing breakdown voltages for small interelectrode gaps and low gas pressures. However, recent experimental results have shown a contrary behavior where the breakdown voltage decreases monotonously for small gaps [18–20]. The cause of this behavior was attributed to ion-enhanced field emission. In a regular gas breakdown, the electron emission from the cathode occurs as a result of the energetic ions bombarding the cathode surface and knocking out the electrons. This is accounted for by the coefficient γ_i. At small interelectrode gaps (<10 μm), the electron emission is also affected by the cathode field emission, which is enhanced by the electric potential of the approaching ion as shown in Fig. 4.1.

At small gaps, the yield of the ion field-assisted electron emission far exceeds the electron emission from ion collision. Thus, the field-assisted emission becomes the primary ionization mechanism at small gaps. This phenomenon has been experimentally observed to cause electrical breakdown through independent experiments. This work used the same concept to generate self-sustained plasma at small gaps in the MOPFET. The phenomenon is well understood, and different theoretical models exist to find its effect on the breakdown voltage [21–22]. Tirumala and Go [21] used an approach that modified the existing Paschen's law to accommodate the field emission. They added an electron emission coefficient (γ') to the existing equation to obtain a modified Paschen's law (eq. 4.2), which applied to any given interelectrode gap and gas pressure. This work extended the modified Paschen's law proposed by Tirumala and Go to accommodate the

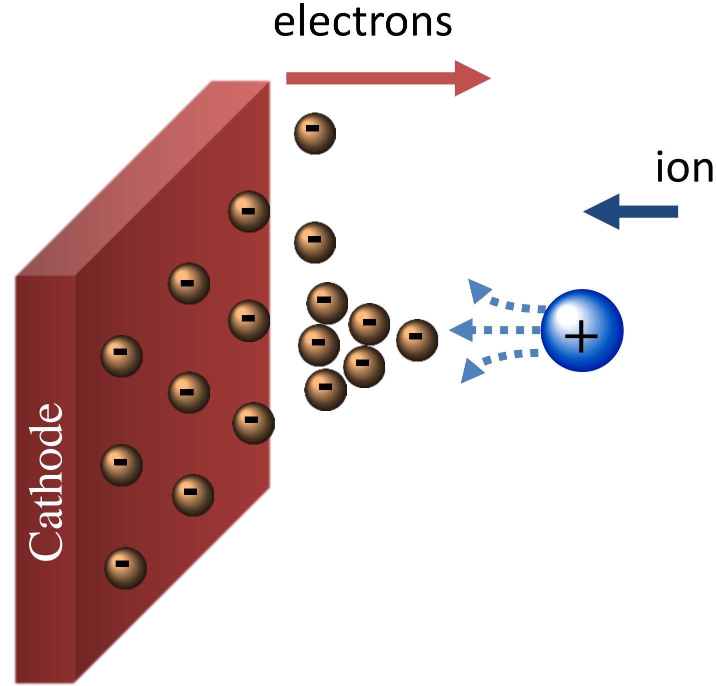

Fig. 4.1. Schematic representation of electron emission at cathode due to electric potential of an approaching ion.

effect of gate field-effect. The model was first curve-fitted to match the experimental breakdown voltages obtained in this work.

$$(\gamma_i + \gamma')\left[e^{Apd\, exp\left(-Bpd/V_b\right)}\right] = 1 \tag{4.2}$$

The ion-enhanced field-emission coefficient, γ', is given by

$$\gamma' = \int_0^R \left(\frac{2\pi r dr}{q}\right) \int_0^T dt \left[\frac{A_{FN} E(r,t)^2}{\varphi t^2(y)}\right] exp\left(-\frac{B_{FN}\varphi^{3/2} v(y)}{E(r,t)}\right) \tag{4.3}$$

And the net electric field at the cathode $E(r,t)$ is given by

$$E(r,t) = (\beta E_A) + \frac{q}{2\pi\varepsilon_0}\frac{L_0 - bE_A t}{[(L_0 - bE_A t)^2 + r^2]^{3/2}} \tag{4.4}$$

where r is the linear dimension of the cathode, A_{FN} and B_{FN} are Fowler-Nordheim field-emission constants, $E(r,t)$ is the electric field at the cathode due to the approaching positive ion, φ is the work-function of the cathode metal, $t^2(y)$ and $v(y)$ are functions with established approximations [23], β is the field-enhancement factor due to asperities on the cathode, E_A is the electric field between the cathode and anode due to applied voltage and is equal to V_b/d, L_0 is the distance from the cathode at which the ion is created, b is the ion mobility, and t is the time. The value for γ_i, R and L_0 are 0.0075, 125 nm, and 25 nm, respectively, as given in [21]. The value of β depends on the surface condition of the cathode. For a perfectly smooth surface, $\beta = 0$. In practice, there is always some roughness and asperities on the electrode surface that increase β up to 100. This work used β as the curve-fitting parameter to match the model closely with the experimental results.

The breakdown voltages were experimentally obtained for MOPFETs with source-drain gaps varying from 1 μm to 6 μm. The MOPFETs were wire-bonded and partially sealed in a hybrid package that was continuously supplied with He and maintained at atmospheric pressure. These MOPFETs had a “bottom-gate” design and were fabricated with TiW, similar to the device shown in Fig. 3.8. A variable dc voltage was applied between the drain and source, with the gate connected to the ground. Fig. 4.2a shows the experimental setup. Agilent 4156C semiconductor parameter analyzer was used as the voltage source for breakdown voltages up to 100 V.

For higher breakdown voltages, a Keithley 237 high voltage source measuring unit was used. To test the breakdown voltage, the drain-source voltage was gradually increased from 0 V, and the current was recorded. At the onset of breakdown, the current

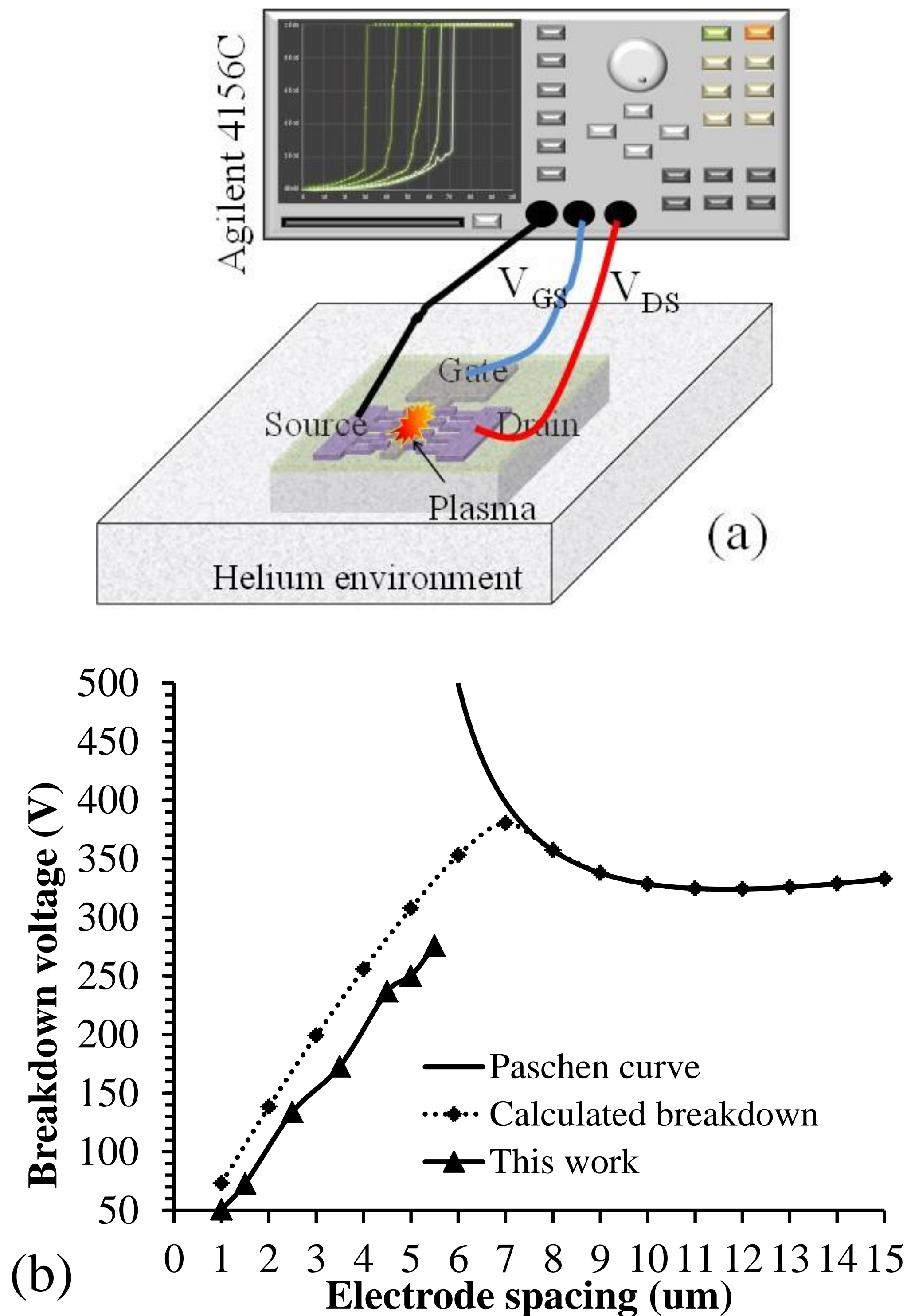

Fig. 4.2.[6] Breakdown voltage characterization of MOPFET. (a) shows the experimental setup. (b) plots the experimental and calculated values of breakdown voltage.

---

[6] P. Pai and M. Tabib-Azar, "Sub 3-micron gap microplasma FET with 50 V turn-on voltage," in *Tech. Dig. IEEE Micro Electro-Mech. Syst. (MEMS)*, Jan. 2014, pp. 171–174. © 2014 IEEE.

rapidly increased. At this stage, the gas was completely conducting and was in a plasma state, showing very small electrical resistance. To prevent damage to the device, the current was limited by setting a low current compliance on the voltage source. Thus, the current saturated to the preset limit after the gas breakdown. The current was limited to ≤10 nA since there was considerable damage to the cathode at higher currents. There was no glow discharge during the breakdown due to the low current limit. The breakdown occurred in the Townsend's dark discharge regime. The experimental breakdown voltages of different MOPFETs are plotted in Fig. 4.2b. The curve-fitted calculated values of breakdown voltage from eq. (4.2) are plotted for comparison and show a significant deviation from the Paschen's curve. The calculations were performed for air at atmospheric pressure. The calculated breakdown voltages matched well against the experimental values for a β of 68. As evident in the plot, the breakdown voltage curves overlap for interelectrode spacing greater than 7 μm, where it reaches a valley before increasing exponentially at much larger spacing (not shown in plot). However, this region is not of interest since the MOPFETs have gaps smaller than 5 μm. The most interesting observation in this plot is the breakdown voltage of 50 V at 1 μm gap. Bringing down the operating voltage of a MOPFET to 10s of volts compared to ~300 V in earlier microplasma transistors is a significant step. The voltage could be reduced further by using a smaller gap. The minimum gap of 1 μm in this work was set by the lithographic limit during fabrication. The breakdown of a gas is indicated by the sudden surge of current. However, the current surge could be due to sparking between the electrodes that causes a momentary breakdown and does not generate self-sufficient plasma. A second proof was required to independently verify plasma generation. In most cases, plasma is

accompanied by a stable glow that proves its existence. But the low currents used here were not sufficient to cause a glow discharge. Therefore, plasma generation was verified by the current-voltage behavior in these devices. The first indication of self-sustained plasma is the steady current flow. The second indication is the hysteresis in the switching characteristics that is typical of plasma [2.2].

Fig. 4.3 shows the current-voltage dependency in a ~1 μm gap MOPFET. During the forward voltage sweep from 0–100 V, the current remained negligible till 50 V. There was a sharp increase in current around 60 V, which marked the onset of breakdown. Further increase in voltage increased the current gradually until the current reached saturation with a sharp jump around 70 V. The plasma became self-sustained at this point and continued to conduct current steadily at higher voltages. The gradual increase in current between 60 and 70 V indicates the slow building up of the avalanche process, with the electrons being supplied mostly by random radiation. Around 70 V, the avalanche reaches a peak and spontaneously generates plasma. At this stage, the plasma is completely sustained by its own free electrons. The reverse voltage sweep from 100–0 V showed a typical plasma switching behavior. The plasma continued to conduct current even when the applied voltage was reduced to less than the breakdown voltage. The reason for this behavior can be understood from the breakdown mechanism. The breakdown is initiated by an avalanche multiplication of electrons, which is supported by a high electric field. After the plasma is generated, the gas behaves like a piece of regular conductor/resistor. There is no more avalanche required to sustain the plasma. The electrons and ions continue to conduct current at lower voltages. When the voltage is reduced below a critical value, the loss of electrons and ions by diffusion to the

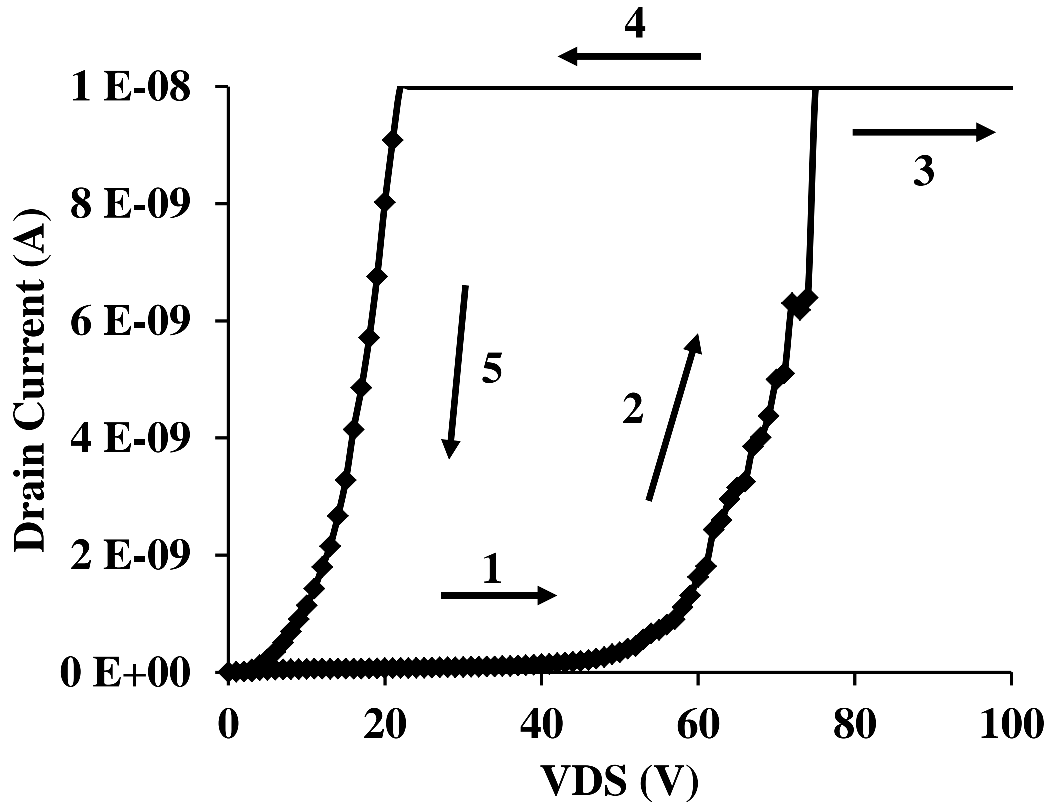

Fig. 4.3.[7] Current-voltage switching characteristics of a 1 μm gap MOPFET. The voltage was swept from 0–100 V and swept back to 0 V as indicated by the numbered arrows.

surrounding gas becomes significant, causing the plasma to turn off.

4.2 Gate field-effect

The most essential function of a transistor is to regulate the current using an auxiliary electrode or a "gate." After successfully testing the plasma generation, the MOPFETs were tested for their gate field-effect. The setup for testing was similar to the one shown in Fig. 4.2a. A second voltage source was used to bias the gate-source electrodes. The gate-source bias allowed the gate electrode to supply electrons or remove electrons from the "channel" (plasma) region that affected the drain- source breakdown

[7] P. Pai and M. Tabib-Azar, "Sub 3-micron gap microplasma FET with 50 V turn-on voltage," in *Tech. Dig. IEEE Micro Electro-Mech. Syst. (MEMS)*, Jan. 2014, pp. 171–174. © 2014 IEEE.

voltage. For a positive gate bias, electrons were removed from the channel region. The reduction in the electron density was compensated by an increase in the drain-source breakdown voltage that would provide additional kinetic energy to the existing electrons and increase their ionization efficiency. Conversely, a negative gate bias supplied electrons to the channel region, which lowered the drain-source breakdown voltage. The gate-field effect was tested by measuring the drain-source breakdown voltage for different gate-source bias. Fig. 4.4a shows detailed current-voltage plots for a ~1 μm gap MOPFET. The experimental results conformed to the theory. The switching had a hysteresis similar to that shown in Fig. 4.3, but is not shown here for clarity of the plot. The results show significant reduction in breakdown voltage for a gate bias of -20 V. This technique can be applied to larger gap devices to bring down the breakdown voltage. The testing was repeated on MOPFETs with different drain-source gaps, and the results are plotted in Fig. 4.4b. As observed in the plot, the gate-field effect affected the breakdown voltage almost linearly.

With the inclusion of a gate field-effect, eq. (4.2) was no longer valid in calculating the breakdown voltage. The equation was modified to include the gate field effect by including the gate-field in the expression for applied field E_A in eq. (4.4). With the addition of a gate bias, the channel field ($E_A=V_{DS}/d$) was modified by the gate field $E_{g1}=V_g/g$ where *"g"* is the gate-channel stand-off distance (Fig. 4.5). The channel field is then given by eq. (4.5). This was substituted into eq. (4.4), and the breakdown voltage was calculated. The new breakdown voltages did not match the experimental values as shown in Fig. 4.4b. The effect of gate-field on the calculated breakdown voltage was stronger than what was experimentally observed. This implied that the effect of gate bias

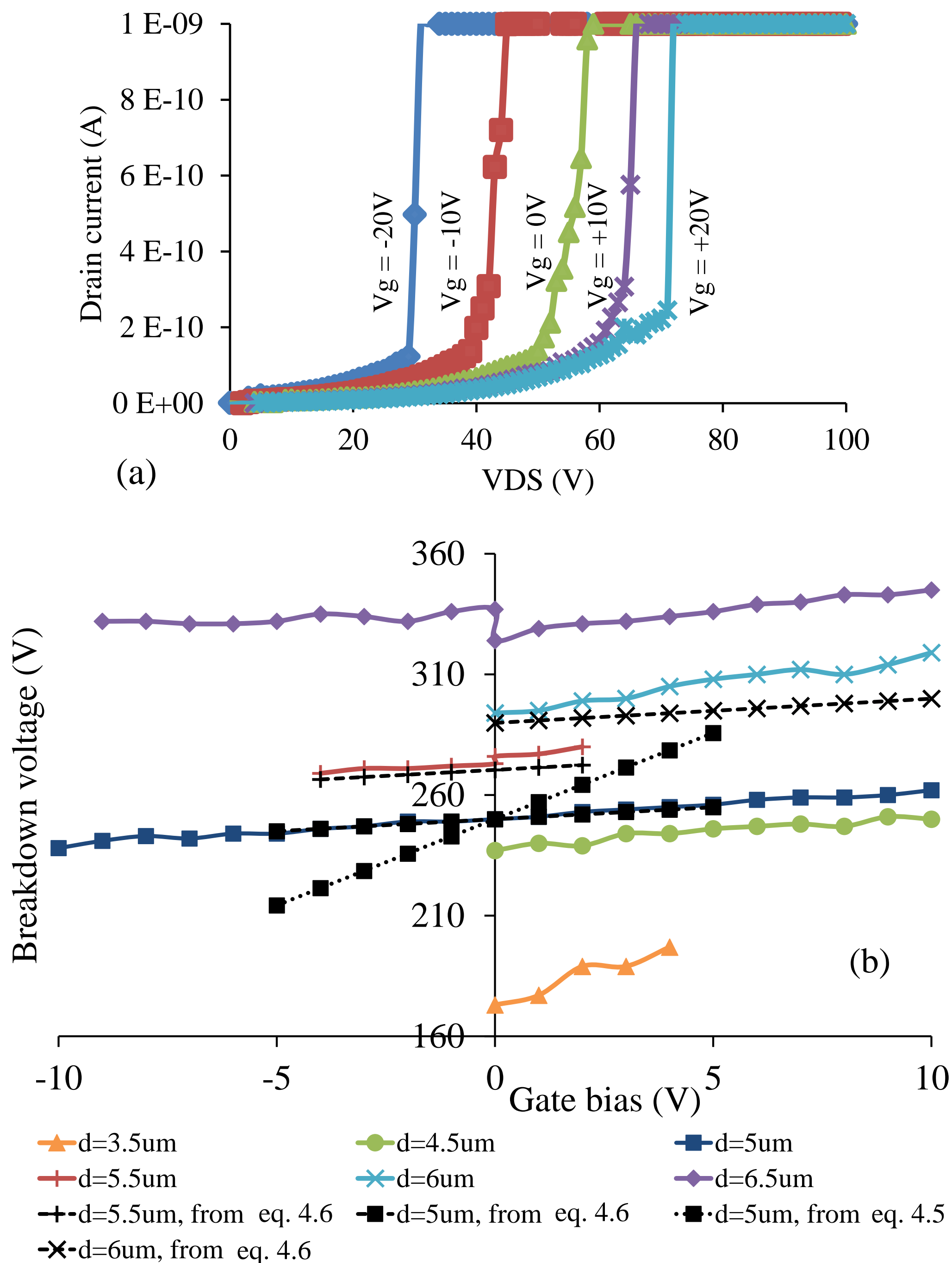

Fig. 4.4. Effect of gate-field on the drain-source breakdown voltage. (a)[8] shows the gate field-effect in a ~1 μm gap device. (b)[9] shows the drain-source breakdown voltages for different gate bias. The solid lines show the experimental values and the dashed/dotted lines are calculated values.

---

[8] P. Pai and M. Tabib-Azar, "Sub 3-micron gap microplasma FET with 50 V turn-on voltage," in *Tech. Dig. IEEE Micro Electro-Mech. Syst. (MEMS)*, Jan. 2014, pp. 171–174. © 2014 IEEE.

[9] P. Pai and M. Tabib-Azar, "Microplasma field effect transistors operating with dc plasma," *IEEE Electron Dev. Lett.*, vol. 35, pp. 593–595, 2014. © 2014 IEEE.

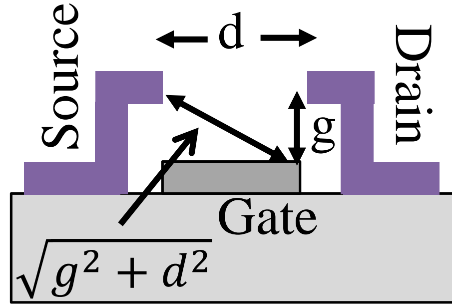

Fig. 4.5.[10] Cross sectional schematic of a MOPFET.

on the channel electric field was less than what was predicted by eq. (4.5). The actual effect of the gate-field can be understood by examining the cross section of a MOPFET as shown in Fig. 4.5. The channel is truly 3-dimensional and the largest voltage drop is at the drain-gate edge (assuming grounded source) when the gate is (-) and the drain is (+). Thus, the contribution of the gate voltage near the drain to the overall electric field is approximately given by $E_{g2}=V_g/(d^2+g^2)^{0.5}$ where *"d"* is the source-drain distance. The effective channel field E_A is then given by eq. (4.6). The breakdown voltages were recalculated by including this modification into eq. (4.4), and the values are plotted in Fig. 4.4b. The updated mathematical model showed a good match with the experimental results. The model is useful in designing a MOPFET more accurately and gives better understanding of the gate field-effect in a MOPFET.

$$E_A = E_{DS} - E_{g1} = \frac{V_{DS}}{d} - \frac{V_{GS}}{g} \tag{4.5}$$

$$E_A = E_{DS} - E_{g2} = \frac{V_{DS}}{d} - \frac{V_{GS}}{\sqrt{g^2+d^2}} \tag{4.6}$$

[10] P. Pai and M. Tabib-Azar, "Microplasma field effect transistors operating with dc plasma," *IEEE Electron Dev. Lett.*, vol. 35, pp. 593–595, 2014. © 2014 IEEE.

The functioning of a MOPFET can be represented by a simple electrical model shown in Fig. 4.6. The main component of the model is the voltage controlled voltage source, which represents the effect of the gate voltage on the breakdown voltage. The variable “A” is a scalar multiplier, synonymous to the voltage gain that depends on the configuration of the MOPFET.

The voltage gain “A” can be obtained from the experimental current-voltage characteristics of Fig. 4.4a. The voltage gain can be defined as the change in drain-source breakdown voltage produced by 1 V change in the gate voltage. To get a quantitative measure of the effect of the gate voltage, we estimate the free electrons Q_G attracted/repelled by the gate from/to the channel region by multiplying the gate capacitance C_G with the gate voltage V_G. The gate capacitance is ~100 fF for a gate of 1 μm width, 100 μm length that attracts (or repels) ~10^6 electrons into the channel. This is significant in comparison to the total gas molecules in the channel, which is ~10^9 assuming a gas molecular density of ~10^{19} cm^{-3} at room temperature. The effect of these free electrons is pronounced when they are accelerated in the drain-source electric field and contribute to the avalanche multiplication by also increasing the secondary electrons’ concentration. From Fig. 4.7 it can be observed that negative gate bias yields $A > 1$ compared to positive biases that yield $A < 1$. This is due to the larger electric field in the vicinity of the drain-gate region, which is greater for a negative gate bias. It is also due to the repulsion of the electrons from the gate electrode. It was experimentally observed that it was almost impossible to prevent the plasma electrons from “leaking” out of any boundary even if it was insulating. But a negative gate bias repels the electrons and effectively increases their concentration in the channel region. These electrons effectively

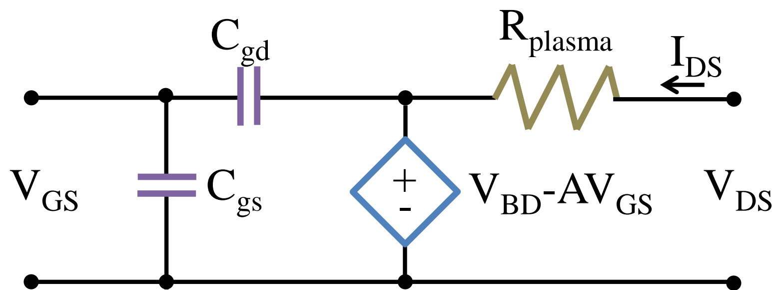

Fig. 4.6. Electrical model of the MOPFET.

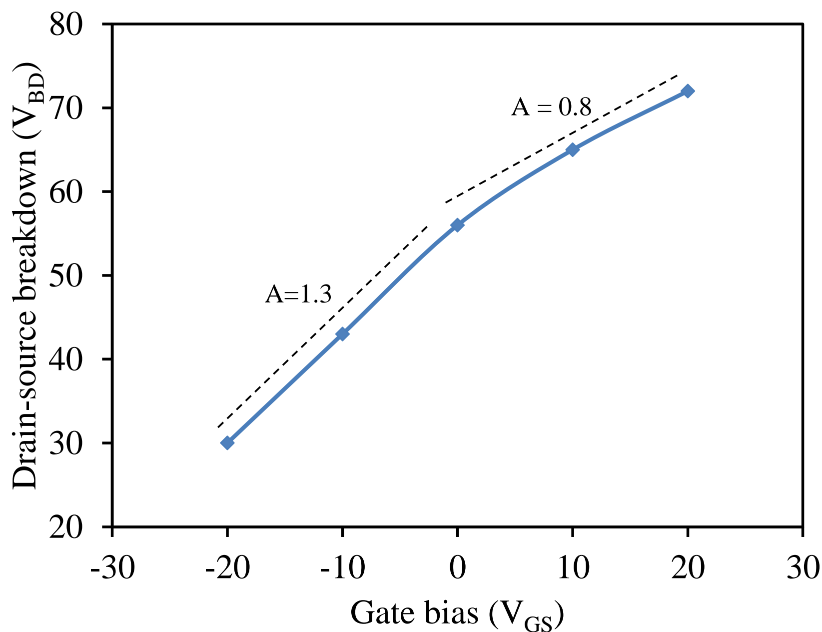

Fig. 4.7. Effect of gate bias on the drain-source breakdown voltage extracted from the data in Fig. 4.4a.

lower the breakdown field by increasing the secondary electron concentration and assisting the ionization process. The breakdown voltage in a semiconductor is proportional to $1/_{N^{0.7}}$, where N is the doping concentration. Similarly, in a MOPFET, the breakdown voltage depends on the free electrons in the channel, which is a function of the gate voltage and can be expressed using eq. (4.7) and (4.8). There is a discontinuity in the mathematical expression around V_G = 0V, due to which the expression for

breakdown voltage is defined for (-1 > V_G > 1).

$$V_{BD} \, \alpha \, \frac{1}{|V_G|^{0.185}} \qquad \text{(for } V_G < -1 \text{ V)} \qquad (4.7)$$

$$V_{BD} \, \alpha \, |V_G|^{0.079} \qquad \text{(for } V_G > 1 \text{ V)} \qquad (4.8)$$

4.3. MOPFET transconductance

One major problem while testing the TiW MOPFETs with dc excitation was the sputtering of the cathode due to ion bombardment. The damage was severe and destroyed the device within a minute of continuous operation. Even with < 10 nA limiting current, the sputtering caused the drain-source gap to widen at a fast rate that led to an increase in breakdown voltage. The presence of microscale protrusions on some electrodes worsened the problem by causing a surge in the local current density, which blew away the electrodes in an instant. Due to this, data points in some of the devices are missing in the plot of Fig. 4.4b. The slopes of the breakdown voltages are abnormally high in some of the devices owing to the same problem.

The fragility of these electrodes made it impossible to carry out testing for a longer duration. The devices are required to operate continuously to test the effect of gate bias on the drain-source current and thereby find the transconductance of the MOPFET. A different fabrication scheme was employed to produce more robust electrodes using electroplating. Fig. 3.9a,b shows SEMs of a MOPFET fabricated by electroplating. The thicker electrodes supported higher operating currents greater than 100 μA with negligible damage to the electrodes. Also, the device could be operated for hours without causing significant damage to the electrodes. The electroplated devices were used to

measure the transconductance of the MOPFET. Due to the limitations in the lithography of these devices, the minimum gap was around 3–4 μm, which increased the operating voltage in these devices.

The device was placed in a He ambience at atmospheric pressure and tested with two high voltage Keithley sources. There was no internal current limit set on the voltage sources to allow the current to swing with an applied gate voltage. Instead, series resistors of 165 kΩ were connected with the drain and source that acted as ballast resistors. The device was turned on by applying sufficient drain-source voltage. The plasma current was limited by the ballast resistors. Once the plasma was generated, it acted like a resistor, and the drain-source voltage could be increased to obtain higher currents. The drain current changed linearly with the drain-source voltage, as expected from a resistor. The experimental current-voltage characteristics between V_{DS} and I_D after the plasma was turned on is plotted by a blue line in Fig. 4.8. As shown in the plot, the device operated with ~500 μA current, which is significantly higher than the capacity of TiW devices. To measure the transconductance, V_{DS} was fixed at 200 V and the V_{GS} was varied in steps of -10 V. A negative bias was expected to increase the drain current due to an influx of electrons from the gate to the channel region, and this was experimentally observed as shown in Fig. 4.8.

From the plot in Fig. 4.8 it is evident that the gate bias has an almost linear effect on the drain current, similar to the effect of V_{DS}. The transconductance g_m, defined as the ratio of I_D and V_{GS}, can be obtained from the slope of the I_D-V_{GS} curve and computes to 5 μS. This is roughly 20x lesser than the transconductance of the plasma BJT developed by Chen and Eden [6]. The reason for significantly low transconductance of the MOPFET

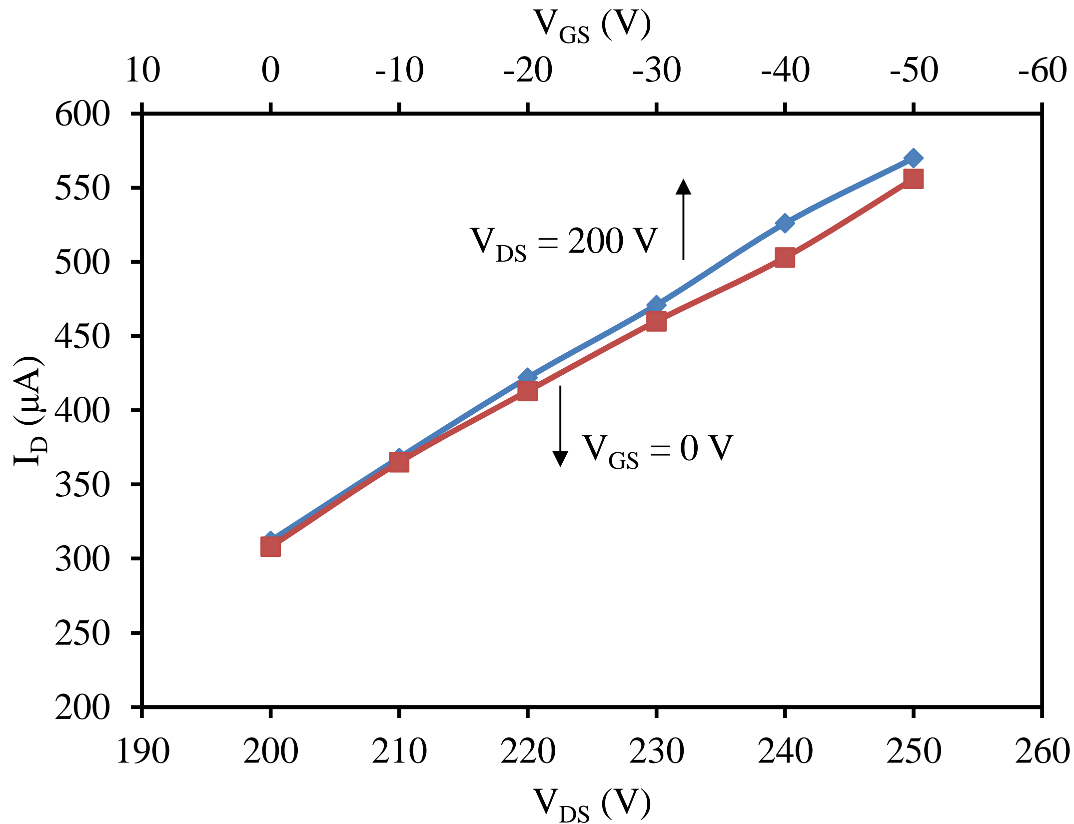

Fig. 4.8. Measurement of the effect of gate voltage on the drain current.

can be deduced by understanding the factors that influence the drain current and by comparing the MOPFET design against the plasma BJT.

A glow discharge plasma is made self-sustained by the development of a sheath of positive space charge surrounding the cathode (source). The sheath is formed due to the low mobility of ions and also due to the fact that ions cannot get absorbed into the cathode directly. The cathode sheath is a very efficient mechanism devised by nature to generate plasma with optimum energy. The externally applied voltage almost entirely drops across the cathode sheath and is termed as the "cathode fall." The width of the sheath spans a few Debye lengths of the ions. Due to this, the cathode sheath maintains an intense electric field that sustains the plasma. A very small portion of the applied

voltage is applied to the rest of the plasma region to drive charges and maintain electrical continuity between the cathode and anode. The current density remains constant through the entire length between the cathode and anode. However, the current is almost entirely due to ions in the cathode sheath, due to which the current density and thus the charge density at the cathode is dominated by ions. The electronic current dominates in the rest of the plasma. Due to the low mobility of ions, the ionic charge density (n_i) has to be significantly higher in the cathode sheath, much greater than the equilibrium charge density ($n_s = n_i = n_e$) in the bulk of the plasma to support the same current density. The plasma develops a positive space charge due to this reason. The current density in a plasma is related to the charge density at the edge of the cathode sheath (n_s) and the potential at the cathode wall due to the cathode sheath as

$$J_D = q.n_s\left[\sqrt{\frac{q.T_e}{M}} + \left\{e^{-\varphi_w/T_e}\sqrt{\left(\frac{q.T_e}{2.\pi.m}\right)}\right\}\right] \tag{4.9}$$

where q is the charge on an electron, n_s is the equilibrium charge density, T_e is the electron temperature in volts, M is the mass of ion (He in this case), φ_w is the cathode sheath potential, and m is the mass of electron. Fig. 4.9 shows experimental results of variation of drain current with the gate bias. The current-voltage values from the plot can be used to estimate the charge density in the plasma, by assuming the electron temperature T_e to be 10 eV. φ_w can be calculated as the difference between the applied voltage and the voltage drop across the resistors for ~500 µA current, which amounts to ~75 V (assuming there is negligible voltage drop outside the cathode sheath). The estimated values of equilibrium charge densities (n_s) are plotted in Fig. 4.9.

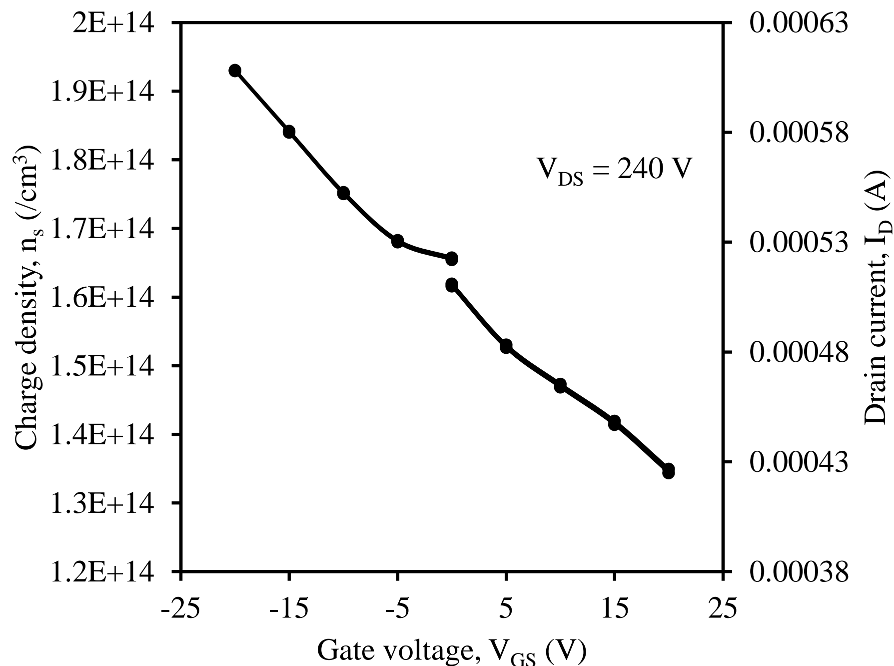

Fig. 4.9. Experimental plot of the gate field-effect showing the effect on drain current and the charge density.

The discontinuity in the plot was due to the drift in the drain current over time. The ratio of the ionic charge density (n_i) to the electronic charge density (n_e) in the cathode sheath was ~50, which was roughly twice the value obtained by Chen and Eden. This can be attributed to the higher gas pressure and significantly smaller interelectrode spacing that shrinked the cathode sheath considerably. The gate bias modifies the electronic charge density in the plasma. Since the electronic charge density in the cathode sheath was extremely lower than the ionic charge density in the MOPFETs, the effect of gate bias was not as significant as that reported in [6]. The second reason for obtaining lower transconductance in the MOPFETs is the choice of the gate electrode. The electron emission from the gate electrode is directly influenced by the work-function of the material. Chen and Eden used a heavily doped n-type silicon as the gate electrode and nickel as the drain/source electrode. A heavily doped n-type silicon can have work

function as low as 4.1 eV compared to the ~5 eV work function of nickel. However, all the electrodes in a MOPFET were fabricated with copper. The lower work-function of the gate material caused higher electron emission in the plasma BJTs [6] compared to the MOPFETs for a given gate bias.

A mathematical relation for the transconductance can be obtained from eq. (4.9) by expressing the plasma sheath potential as a function of the gate bias.

$$g_m = \frac{\partial I_{DS}}{\partial V_{GS}} = \frac{S.\partial J_{DS}}{\partial V_{GS}} = \frac{-S.q.n_s\{\partial(\varphi_W(V_{GS}))\}e^{-\varphi_W(V_{GS})/T_e}\sqrt{\left(\frac{q.T_e}{2.\pi.m}\right)}}{V_{GS}} \tag{4.10}$$

where S is the surface area of the source eletrode. As evident in eq. (4.10), the gate bias can have a significant influence on the transconductance by affecting the sheath potential. The transconductance in the MOPFET could be improved by optimizing the geometry and the position of the gate electrode with respect to the drain and source for maximum effect on the sheath potential.

4.4 Comparison between TiW and Cu MOPFETs

Sections 4.2 and 4.3 discussed the characterization of two varieties of MOPFETs. The TiW MOPFETs achieved low switching voltages, but could not sustain large currents. The Cu MOPFETs sustained larger currents, but vary in their structure and functionality from a true MOPFET. Fig. 4.10 shows SEM images of the two MOPFETs for comparison. The absence of a gate dielectric in the Cu MOPFETs allowed both ionic and electronic currents to pass through the gate, which is unlike the condition in the TiW MOPFET. Due to this, the gate electrode in the Cu MOPFET functioned like a Langmuir

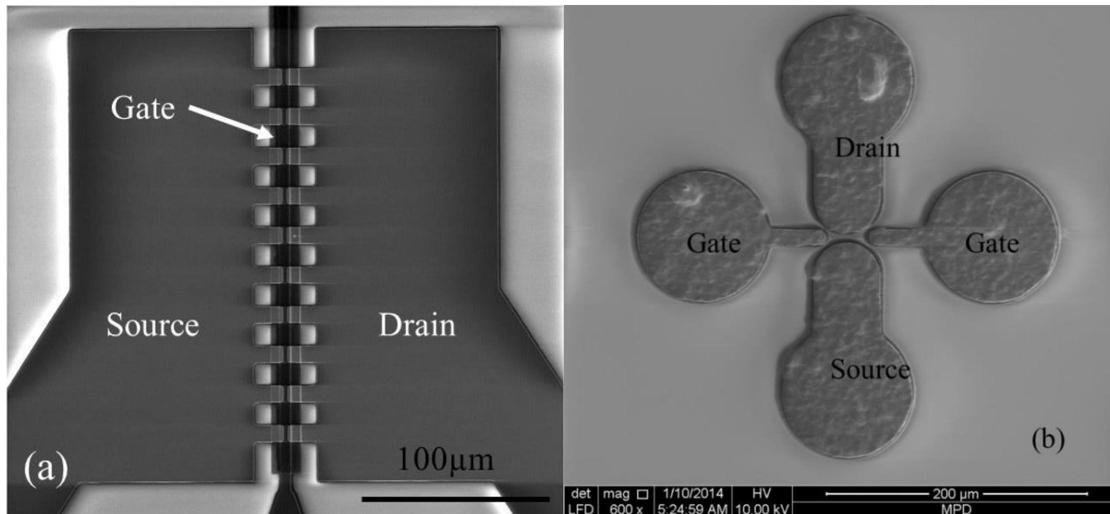

Fig. 4.10. SEM images of the two varieties of MOPFET. (a) shows the TiW thin film MOPFET characterized in section 4.2. (b) shows the Cu thick film MOPFET characterized in section 4.3.

probe. Accordingly, the gate field effect had a linear effect on the drain current for moderate levels of gate voltage. For sufficiently positive/negative gate voltage with respect to the plasma potential, the current saturates. The deviation from linearity can be faintly observed in Fig. 4.8 as the gate bias is increased in magnitude. Also, the location of the gate electrodes in the Cu MOPFETs does not provide optimum access to the channel region. As shown in Fig. 4.10b, the gate electrodes access the channel region only from the sides. But the largest area of access to the channel is through the top or bottom. Due to the high aspect ratio of the electrodes, a hybrid design is required that combines the design of TiW and Cu MOPFETs. Such a MOPFET would have the gate electrode contacting the channel on 3 sides, providing better gate control. The gate insulation could be provided by an atomic layer deposition process. One limitation common to both these MOPFETs is the maximum allowable negative bias. The electric field in the channel region is high in the vicinity of the drain-gate for a negative gate bias. When the gate bias is sufficiently negative, the electric field will be sufficient to

breakdown the gate oxide and generate plasma between the drain and gate instead of the drain and source. Based on the experimental testing, it was safe to operate the gate with less than half the magnitude of the drain bias.

4.5 Carrier mobility

The performance of a transistor is judged by its gain and switching speed. The previous section discussed the factors that influenced the gain of the MOPFET. The switching speed has a close relationship with the carrier mobility. It is desirable to have higher mobilities for fast switching. A popular and simple technique to measure the carrier mobility is the Hall effect. For a plasma medium, the mobility depends on the gas species and the operating gas pressure. The Hall measurements were performed in atmospheric pressure to yield data relevant to MOPFETs. The magnitude of Hall voltage generated is proportional to the current flowing normal to the magnetic field and the magnitude of the magnetic field. The electrodes for Hall measurement were fabricated with 25-µm thick electroplated copper. The interelectrode spacing for plasma and Hall electrodes were 250 µm and 100 µm, respectively. A Neodymium magnet with a field of 0.3 T was used as the source of the transverse magnetic field. Fig. 4.11a shows the experimental setup. The current through the plasma electrodes was set to 100 µA during the measurement. The magnetic field was directed out of the plane of the electrodes. Fig. 4.11b shows an optical picture of the device during operation. Both electrons and ions in the plasma respond to the magnetic field. The plasma, however, does not form as one uniform layer between the cathode and anode in the glow discharge mode. Instead it forms striations of glowing and dark regions with each region characterized by the differences in ionic and electronic charge densities [13]. The glowing region close to the

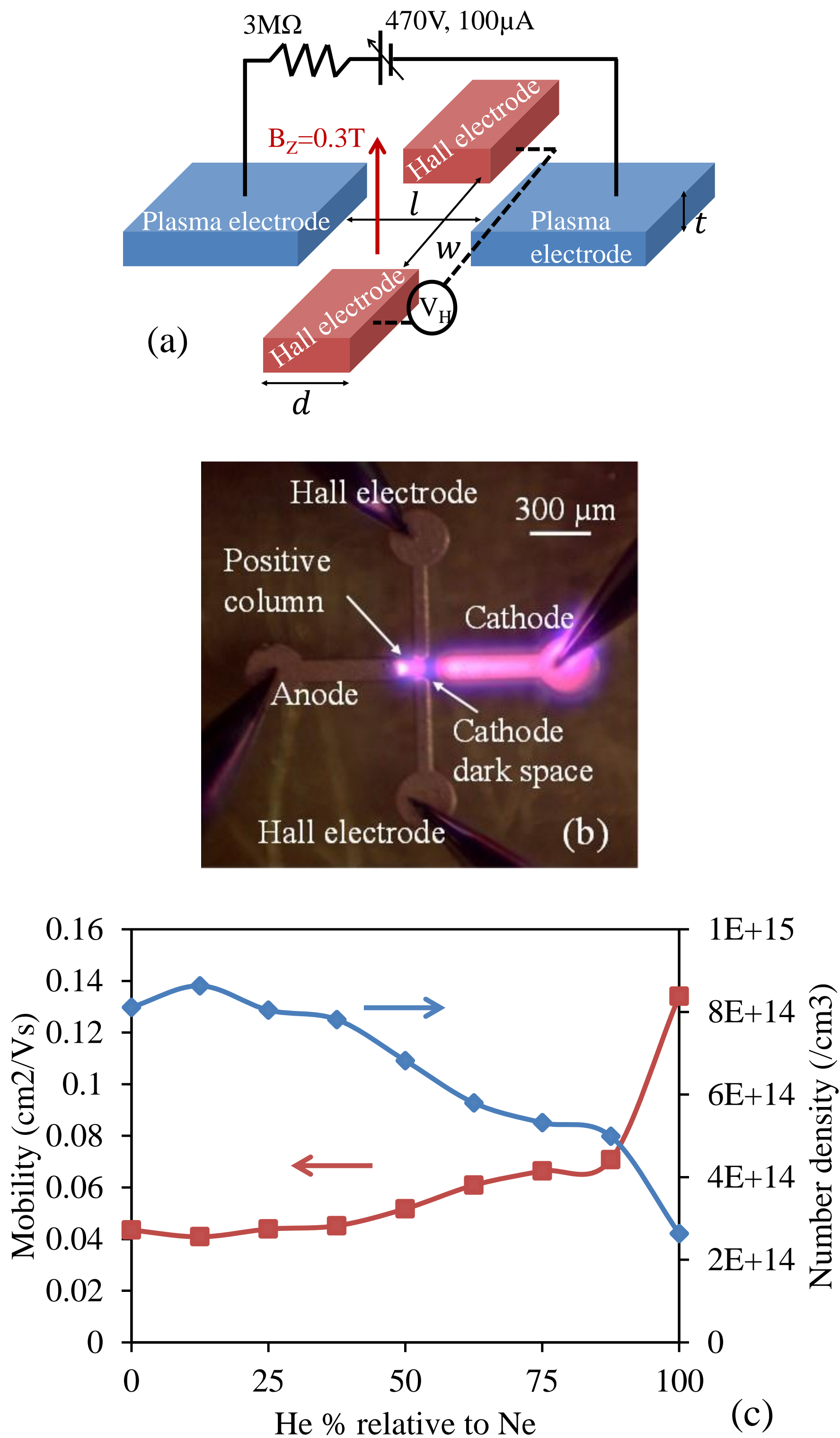

Fig. 4.11. Results of the Hall effect experiment. (a) shows the experimental setup. (b) shows a picture of the testing device during operation. (c) shows the experimental carrier mobility and charge density.

anode is called the positive column, which contains an equal number of electrons and ions and is quasi-neutral. The dark space near the cathode is the "cathode dark space," where most of the ionization occurs. Due to their heavier mass, the ions tend to get accumulated in this region all the way to the cathode, whereas the electrons proceed towards the anode. This creates a positive space charge. The glow on the cathode is due to the excited gas molecules and atoms. At large electrode spacing of a few centimeters and low operating pressures, these regions span over larger lengths and are well separated. The response of electrons or ions to the magnetic field can be separated from each other by placing the Hall electrodes close to the anode or cathode, respectively. At small electrode gaps and higher pressures, the gap is mostly filled with the positive column that transforms to the "cathode dark space" as it approaches the cathode (see Fig. 4.11b). Due to the positive space charge in the "cathode dark space," the Hall voltage measurements reflected the mobilities and charge densities of ions. However, since the plasma is quasi-neutral, the electron charge density will be the same as that of the ion. The measurements were made with a mixture of He and Ne at different ratios to observe the effect of different gases on carrier mobility and charge density. The Hall electric field obtained for different gas compositions were used to calculate the ion mobilities and ion densities using the following relations, where E_H, v, B_Z, J_X, V_X, q, n, μ, and l are the Hall electric field, ion velocity, transverse magnetic field, longitudinal current density, longitudinal voltage, electronic charge, ion density, ion mobility, and plasma electrode separation, respectively.

$$E_H \cong -v \times B_Z = \frac{B_Z \times J_X}{q.n} \quad (4.11)$$

$$\mu = \frac{v}{V_X/_l} \tag{4.12}$$

The actual Hall voltage is twice the value that is measured by the Hall electrodes across plasma due to the asymmetric electric charge density across the axis [24]. This factor was taken into account while estimating mobility and density using (4.11) and (4.12). Ion mobilities and densities obtained from Hall measurement are plotted in Fig. 4.11c. The charge densities are roughly of the same magnitude as that obtained though eq. (4.9). The mobility was highest in He, reduced significantly with the addition of just 10% Ne to the mixture, and continued to decrease. The reason for this behavior was the heavier mass of Ne ions. The mobility of Ne ions is 3x smaller than the He ions as plotted in Fig. 4.11c. As a result, even a small addition of Ne gas to the mixture generated a space charge dominated by Ne ions, thereby dominating the Hall voltage. For a given current density, the charge density depends on several factors including generation-recombination rates of charges, ionization efficiency, loss to surroundings by diffusion, etc. Due to the heavier mass of Ne ions, the loss to surroundings by diffusion can be expected to be lower than He ions. This could be one reason for the higher charge densities in Ne. A simpler argument can also be made to justify this by considering the mathematical relation for current density. Since mobility and charge density are directly proportional to current density, a faster He ion is expected to have lower charge density compared to slower Ne ion if both have the same current densities.

The gas pressure also affects the carrier mobility. At higher gas pressures, the number density of gas molecules is greater and thus restricts the motion of the charge carriers resulting in lower mobilities. The converse is true for lower pressures. Hence, the ion mobilities measured in this work are roughly two orders of magnitude smaller than

that reported for low pressure measurements in literature [25–26]. In addition to higher pressure, the temperature of operation also affects the measured mobility. All the mobility experiments reported in the literature were performed in long tubes at lower pressure, allowing a sufficient area of dissipating heat away from the plasma. The setup used here has a tightly packed space that creates a local hot spot in the core of the plasma. The elevated temperature increases the thermal agitation of gas molecules, further lowering the charge mobility. Lastly, it is to be noted that the mobility and the charge density in the actual microplasma transistor will be slightly different from the values calculated using this setup due to the smaller interelectrode gaps in the transistor. This experiment was performed to obtain a rough estimate of the carrier properties at this size scale and operating pressure.

This chapter presented detailed experimental results of the dc switching characteristics of the MOPFET. The gate field-effect was very evident even at small gaps and small excitation voltages. The main problem experienced during the dc testing was the sputtering of the cathode (source electrode) that damaged the device. An alternate fabrication scheme using electroplated copper electrodes solved this problem. However, this scheme had its own limitations and produced a more BJT like response due to the absence of insulation layer on the gate. The dynamic response of the MOPFET depends on the mobility of the charge carriers. The experimental results from the Hall effect measurements provided an estimate of the ion mobility and charge density. The dynamic response of the device to rf gate voltage is presented in the next chapter.

CHAPTER 5

MOPFET RF CHARACTERIZATION

Most of the practical applications of transistors require operation with rf input excitation. The previous chapter presented the complete dc characterization of the MOPFET, which helped in understanding the basic functioning of the device. This chapter discusses the operation of the MOPFET with rf excitation. One of the advantages of using rf excitation voltage instead of a dc is in preventing sputtering damage to the electrodes. The alternating field in an rf excitation oscillates the charges back and forth between the electrodes. For frequencies above ~50 kHz, the ions fail to synchronize with the oscillations due to their heavy mass, remain almost stationary in most parts of the plasma, and are agitated mostly by their thermal energy. There are, however, sheaths created at the electrodes during alternate cycles of the rf oscillations, during which some ions get accelerated towards the electrode. But in the absence of a dc bias, the ions do not acquire sufficient energy to cause damage to the electrodes. This allowed the use of thin film TiW MOPFETs for all the characterizations performed using rf excitation. RF excitation was used for both plasma generation and current modulation.

5.1 RF plasma switching with two electrodes

Similar to dc excitation, plasma can be generated with rf excitation by applying sufficient voltage greater than the breakdown voltage. Most rf signal sources have limited

output voltage ratings, typically up to 2 V_{p-p}. RF amplifiers can boost this signal by up to 20 dB. However, the rf amplifiers are tuned to deliver maximum power to 50 Ω loads. The MOPFETs were not tuned to 50 Ω impedance. Due to this, a matching network was required to deliver the power from the rf amplifier to the MOPFETs efficiently. The matching network was a simple inductor with a few turns of copper wire connected in series with the drain-source electrodes of the MOPFET. The inductance of the inductor was varied by changing the number of turns on the coil that was used to tune the resonant frequency of the LC network to a desired frequency. The impedance of a LC network is minimum at the resonant frequency and is almost entirely resistive. Fig. 5.1 shows the frequency response of a tuned MOPFET showing a dip of >10 dB at its resonant frequency. The resonant frequency was tuned between 0.1–1 GHz to keep it within the frequency limit of the rf signal source.

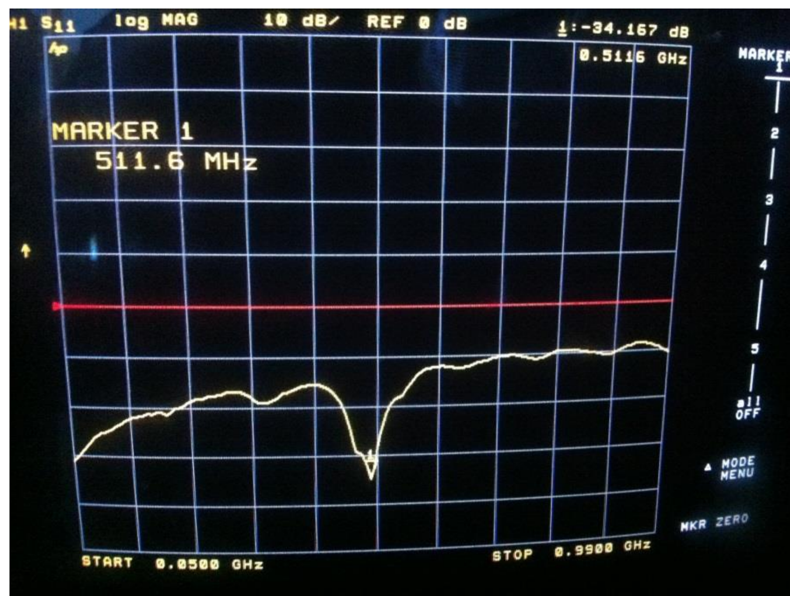

Fig. 5.1. Frequency response of a tuned MOPFET showing a resonant frequency of 511.6 MHz.

The tuned MOPFETs were then tested for plasma generation. Unlike the dc source measurement units, the rf source was not equipped with a current measurement unit. A secondary means was required to detect the plasma current during operation. The direct option was to include a series resistor with the LC network and calculate the current by measuring the voltage drop across the resistor. However, at the instant of plasma generation, most of the amplified rf voltage would drop across the resistor due to the extremely low resistance of the plasma. A regular oscilloscope is not capable of handling such high voltages even with a 10x reduction probe. To prevent damage to the oscilloscope, the plasma current (drain current) was indirectly measured by a capacitive probe as shown in the schematic of Fig. 5.2a. Although the capacitive probe did not measure the exact current, it indicated the variation in the current accurately. The current-voltage characteristics of the drain-source were tested by gradually increasing the rf source voltage well beyond the breakdown voltage and decreasing it down to zero. The switching was tested with a 937 MHz voltage signal. The switching behavior is plotted in Fig. 5.2b. The rf switching showed hysteresis similar to the dc switching. Since there was no current limit set during measurement, the plasma current continued to increase after turning on. Similarly, the current decreased gradually until the plasma turned off. The slope of the green and red lines are proportional to the combined resistance of the plasma and the LC network. The nonzero current before the plasma turned on (blue line) was due to the rf radiation leaking to the capacitive probe. The drain current was roughly in the range of 100 μA, which was sufficient to produce a glow discharge.

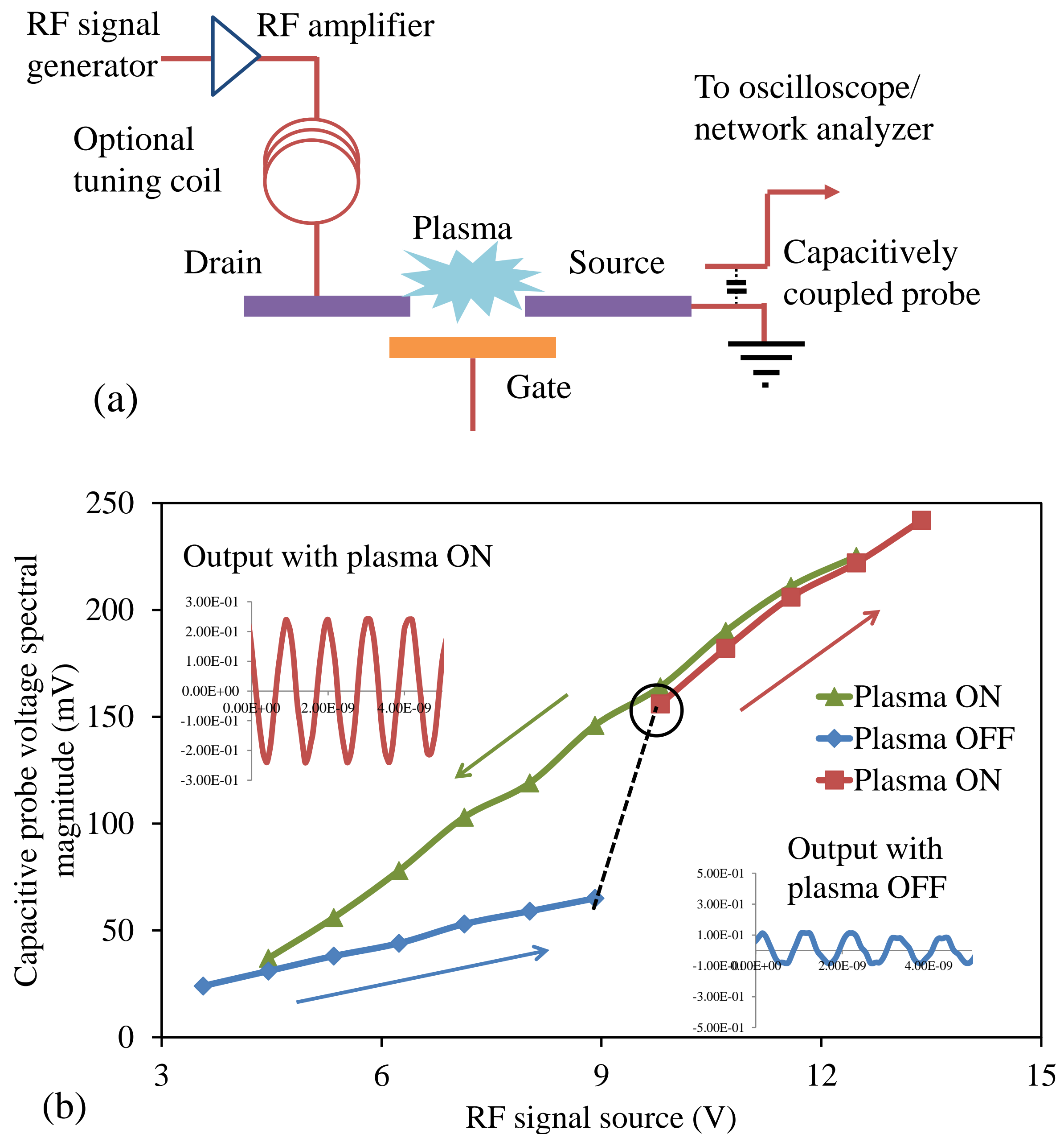

Fig. 5.2. Plasma generation using rf excitation. (a) shows the schematic of the testing setup. (b) shows the current-voltage characteristics observed during the plasma generation.

5.2 Gate field-effect with dc excitation

The advantage of having a glow discharge was that it allowed testing to be performed with optical detection. The presence and absence of the glow discharge indicated the ON and OFF states of the transistor. The intensity of the glow varied with the change in plasma current. This reduced the unwanted rf noise significantly. The optical detection setup of Fig. 5.3a was used to test the gate field-effect of the MOPFET. The optical detection was done using either a photomultiplier tube or a phototransistor. Both these detectors produced a voltage proportional to the intensity of the plasma glow. Fig. 5.3b shows the optical picture of a MOPFET during operation. The visible light from the glow discharge is very evident from the photograph, which was sufficient to produce appreciable output voltage on the photo detectors. For gate field-effect measurements using dc voltages, a voltmeter was used to record the voltage of the photo detector. The dc voltage on the gate was fixed at a particular value, and the rf voltage on the drain-source was gradually increased in steps from 0 V to a little beyond the breakdown voltage. As mentioned earlier, there was no current limit set on the rf source, and the current continued to increase after the breakdown, which also increased the intensity of the glow. The response of the device beyond breakdown was clipped in the plot of Fig. 5.3c for clarity. The gate bias had the same effect on the device switching as observed during dc characterization. The breakdown voltage was reduced for a negative gate bias and increased for a positive gate bias.

5.3 Gate field-effect with rf excitation

The experimental setup for testing the gate field-effect was the same as the one shown in Fig. 5.3a. The plasma between drain-source was excited with a 600 MHz rf

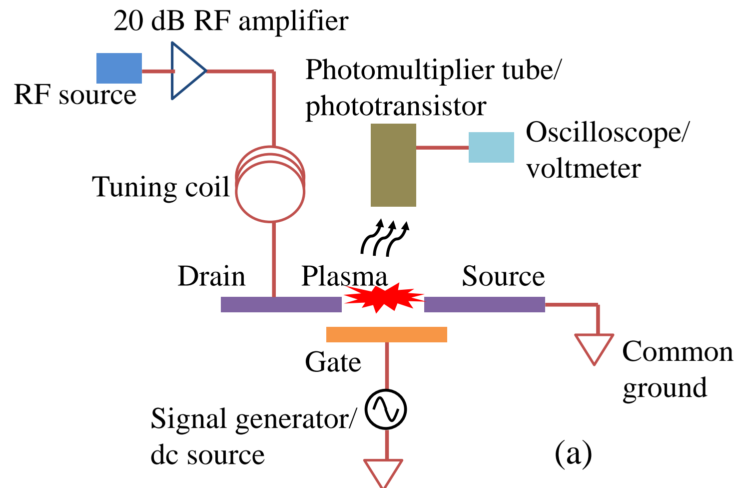

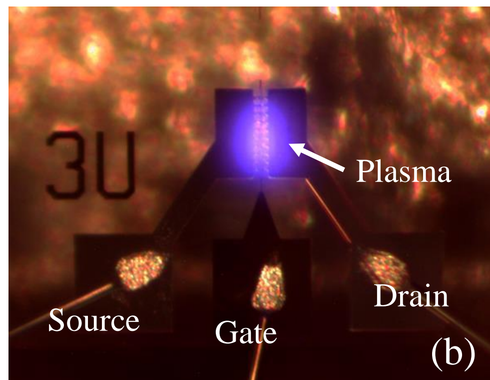

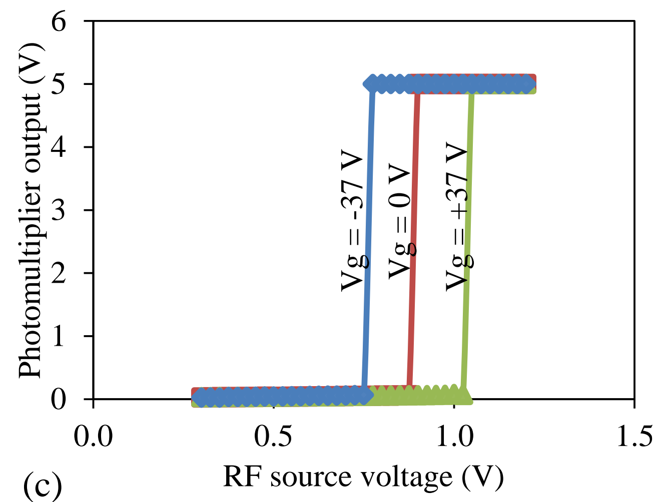

Fig. 5.3.[11] Gate field-effect testing of the MOPFET with dc excitation. (a) shows schematic of the testing setup. (b) shows a photograph of a MOPFET during operation. (c) shows the switching characteristics.

---

[11] P. Pai and M. Tabib-Azar, “Sub 3-micron gap microplasma FET with 50 V turn-on voltage,” in *Tech. Dig. IEEE Micro Electro-Mech. Syst. (MEMS)*, Jan. 2014, pp. 171–174. © 2014 IEEE.

voltage. The gate was excited with a signal generator at different frequencies from kHz to GHz. The plasma current modulation was detected optically at lower frequencies (up to 1 MHz) and electrically at higher frequencies due to the limited bandwidth (~100 kHz) of the phototransistor. Fig. 5.4 shows time-domain response of the plasma luminance for a 10 kHz square wave gate voltage. The intensity of plasma decreased during the positive cycle of the gate voltage and increased during the negative cycle. This behavior was directly a result of the variations in the plasma current.

At this point it is worth mentioning that the drain current modulation at 10 kHz had surpassed the 4 kHz switching speed of the microplasma transistor reported in the past [7]. To test the frequency limit of the MOPFET, the frequency of the gate voltage was stepped up to 1 MHz by applying 1 μs pulses at 1 kHz. Pulses were chosen over square wave to differentiate noise from the actual signal clearly, considering that the input frequency had exceeded the frequency range of the phototransistor. Fig. 5.5 shows

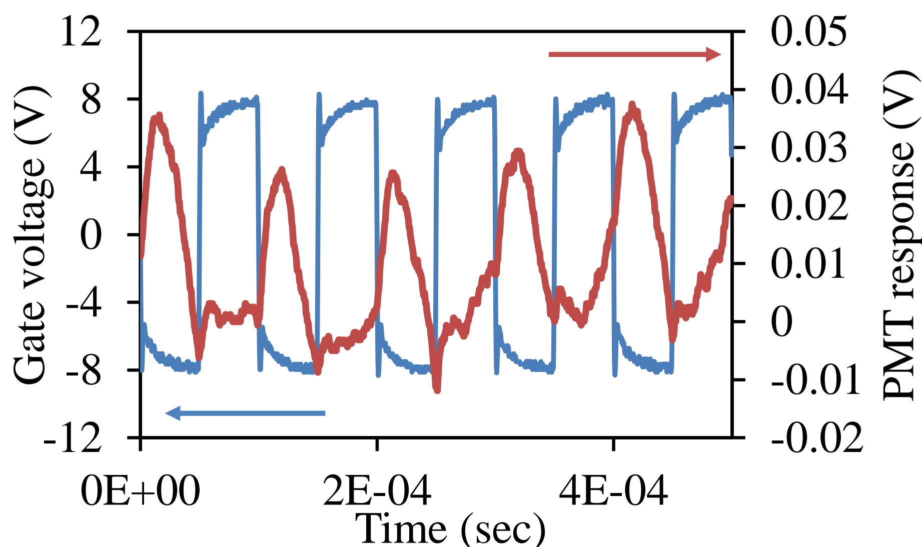

Fig. 5.4. Time-domain response of the plasma luminance to a 10 kHz, 16 V_{pp} gate voltage.

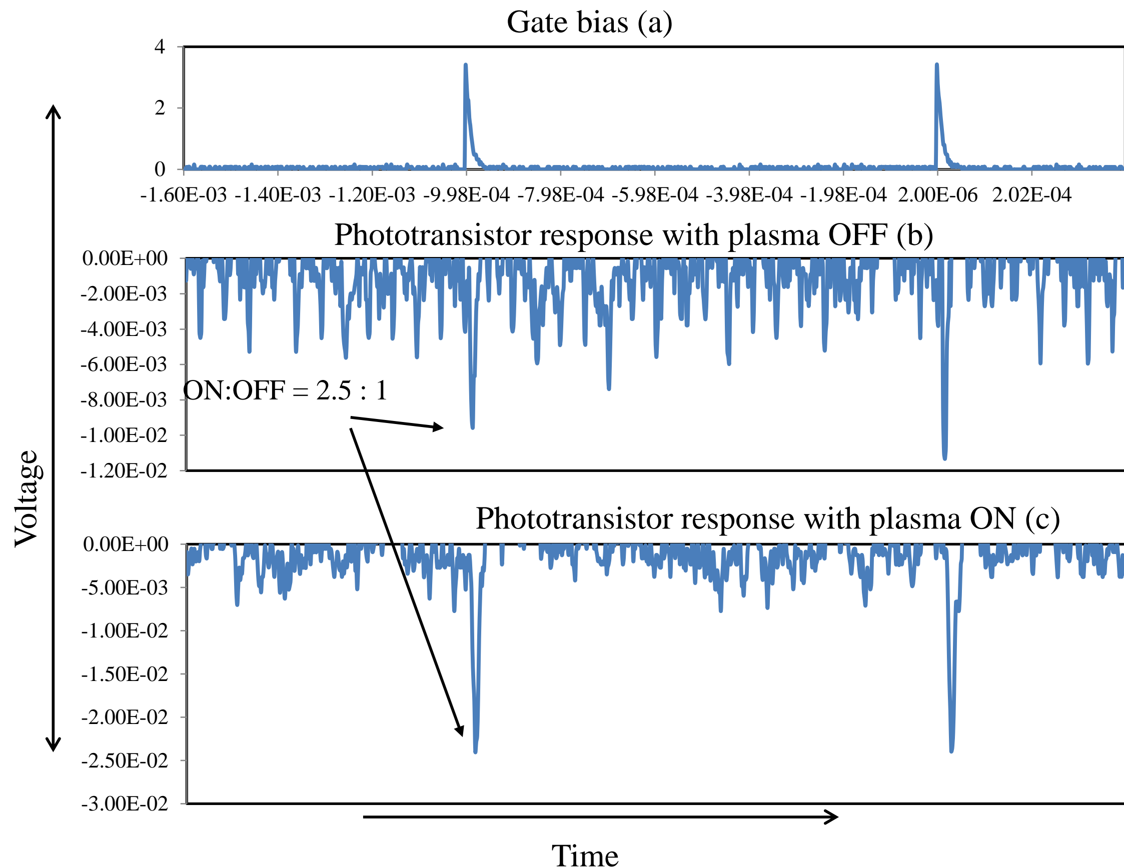

Fig. 5.5. Time domain response of the MOPFET plasma luminance for 1 μs gate pulses. (a) shows the gate voltage pulses. (b) shows the phototransistor response when the plasma was OFF. (c) shows the phototransistor response when the plasma was ON.

the time-domain response of the plasma luminance for 1 μs pulses. The radiative leakage of rf signal on a wire increases at higher frequencies. The electrically unshielded hybrid package allowed the excitation signals from the drain, source, and gate electrodes of the MOPFET to be easily transmitted to the surrounding. Due to the close proximity of the phototransistor electrical leads to the MOPFET, there was sufficient voltage induced in the leads to produce an appreciable voltage after amplification. This was not a problem at frequencies within the bandwidth of operation of the phototransistor as the output voltage of the phototransistor was large. As the modulation frequency of the plasma luminance increased beyond the phototransistor bandwidth, there was practically no gain produced

by it. Under this condition, the output voltage produced by the phototransistor in the presence of an optical excitation was comparable in magnitude to the noise voltage produced by the radiation leakage from the MOPFET electrodes. This can be understood better by looking at the output response of the phototransistor in Fig. 5.5. The variations in the gate signal were registered in the phototransistor output even in the absence of plasma as shown in Fig. 5.5b. This was solely due to the radiative leakage of the gate signal to the phototransistor leads. In the presence of plasma, the response of the phototransistor was ~2.5x stronger than the noise signal as shown in Fig. 5.5c. The phototransistor could not be used for any higher frequencies.

The unity gain cut-off frequency of BJTs and MOSFETs are proportional to the ratio of the device transconductance and the gate/base capacitance. Due to the similar nature of operation of the MOPFETs, the same relation can be used to get a rough estimate on the operating frequency range. Since the gain of the MOPFET was ~1 (Chapter 4), the calculated unity gain cut-off frequency would just indicate the practical operating frequency range. Based on the results obtained in Chapter 4, the transconductance of the MOPFET can be assumed to be ~5–10 μS. The gate capacitance (3μm length, 200 μm width, ~1 μm dielectric gap) of the MOPFET shown in Fig. 5.3b is estimated to be ~100 fF, considering the dielectric to be air. Based on these values, a cut-off frequency of ~50 MHz is obtained. The actual capacitance will differ from the estimated value due to the dielectric effect of the plasma. The dielectric constant of the plasma is a function of the excitation frequency and is a complex variable to determine. To improve the operating frequency range, the gate capacitance of the MOPFET was further reduced by using only 1 pair of drain-source electrodes, which reduced the width

of the gate by a factor of ~10. The absence of the gate insulator further reduced the capacitance by a factor of ~10. This was expected to increase the operating frequency of the MOPFET to ~5 GHz.

The MOPFET was tested for GHz current modulation using the electrical detection technique shown in Fig. 5.2a since the phototransistor could not operate at such high frequencies. The electrical detection was expected to be noisy since the capacitive probe was left floating, which basically acted like a receiving antenna. Therefore, the measurements were made in the frequency domain. The output of the capacitive probe could not be measured using an oscilloscope since the frequency was out of range of the oscilloscope. A 20 GHz bandwidth HP network analyzer was used to excite the gate as well as detect the output of the capacitive probe. The weak output signal of the network analyzer was amplified using a variable gain X-band amplifier. The amplifier was limited in its bandwidth from 7–10 GHz, due to which the testing was confined to this range. The plasma between drain and source was generated with a 600 MHz amplified rf voltage. Fig. 5.6a shows a photograph of the device during operation. Fig. 5.6b shows the gate field-effect on the drain-source current.

Similar to the radiative rf leakage observed in phototransistor output in Fig. 5.5b, the capacitive probe was prone to the rf leakage. Therefore, the response of the capacitive probe was recorded with the plasma OFF and ON to clearly distinguish the gate field-effect on the plasma current. These two outputs were normalized and plotted in Fig. 5.6b for comparison. The gate field-effect is evident from the plot, which shows a ~5 dB difference in the power at ~7.3 GHz between the plasma ON and OFF states. However, the response is not flat and shows a frequency selective behavior. This was caused by an

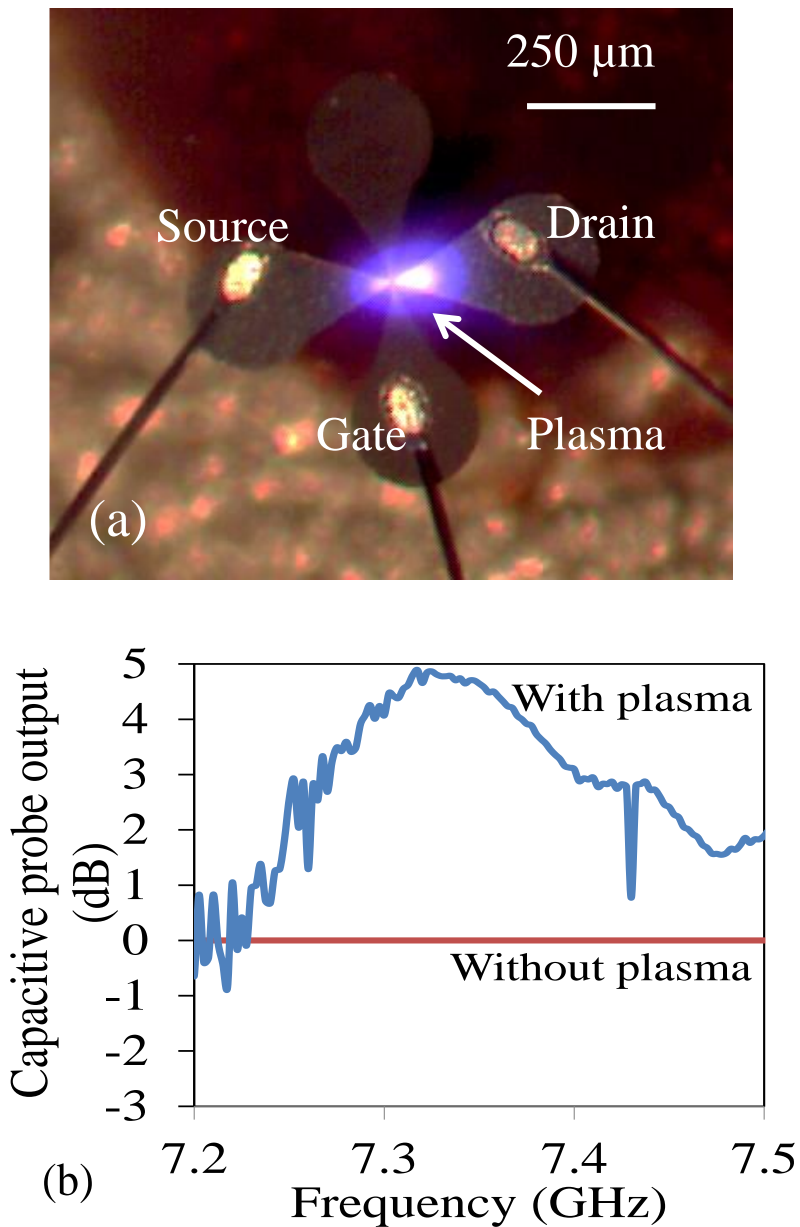

Fig. 5.6. High frequency gate field-effect characterization of MOPFET. (a) shows a photograph of the device during operation. (b) shows frequency response of the drain-source current picked up by the capacitive probe.

impedance mismatch between the input impedance at the gate and the rf source. The excitation frequency of 7–10 GHz is well in the microwave range, where the geometries and dimensions of the device electrodes and routing wires affect signal propagation. For proper operation, the devices are required to have appropriate geometries and well-matched impedance. Since the MOPFETs used in this work were not optimized in this regard, they responded only to a small frequency range within 7–10 GHz. Despite this shortcoming, the device succeeded in demonstrating gate field-effect at GHz frequencies, which far exceeds the operating speeds of earlier microplasma transistors. Owing to almost no contribution from ionic currents, the device can be considered to be an electronic device at these frequencies. Although the gate response showed plasma current modulation up to ~7.5 GHz, the electrons in the plasma can respond to even higher frequencies. To test if this was true, the output of the X band amplifier was connected to the drain-source to generate plasma, leaving the gate electrode floating. The amplifier was excited with the HP network analyzer. The excitation frequency was pushed to the maximum limit (10 GHz) of the X band amplifier. The plasma generation was detected by the same capacitive probe. Fig. 5.7 shows frequency response of the current through the drain-source detected by the capacitive probe. The spikes in the response indicate the plasma firing. As indicated by the spikes, the plasma was generated at 10 GHz and could be sustained for long by applying a steady 10 GHz signal. This supports the fact that the frequency selective behavior observed in Fig. 5.6b was due to lack of device optimization, rather than the lack of plasma response.

The results obtained with the MOPFETs are promising and with some more effort in optimizing the frequency response, these devices could be successfully

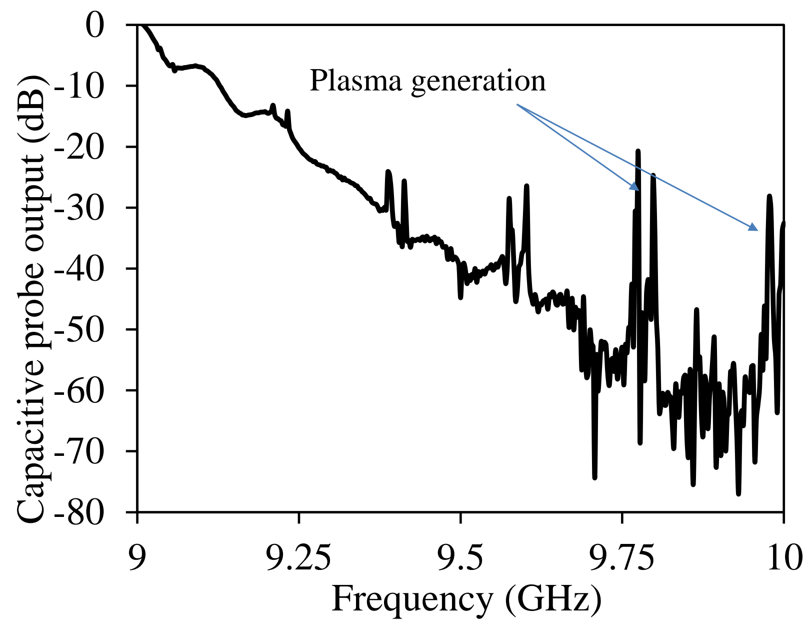

Fig. 5.7.[12] Frequency response of the drain-source current obtained by exciting the drain-source with the X band amplifier.

[12] P. Pai and M. Tabib-Azar, "Sub 3-micron gap microplasma FET with 50 V turn-on voltage," in *Tech. Dig. IEEE Micro Electro-Mech. Syst. (MEMS)*, Jan. 2014, pp. 171–174. © 2014 IEEE.

commercialized for harsh environment operation. The use of rf excitation to generate plasma solved the dc sputtering problem and improved device longevity. The MOPFET showed gate field-effect over a wide range of frequencies. A better technique to accurately monitor the drain current is required to perform a complete frequency-domain response of the transistor.

CHAPTER 6

MICROPLASMA LOGIC CIRCUITS

A majority of this thesis discussed microplasma transistors and their characterization. As an electronic component, the transistor is the most essential part of a functioning circuit. A typical digital integrated circuit consists of millions of transistors, most of which perform logical switching operations to serve an application. One of the applications of microplasma transistors is as switches for logic gates. There is not much work done in this area. The only microplasma-based logic circuit implementation reported in the past [27] was used to address pixels in a plasma display that used space-charge effect and timed switching. This chapter presents two novel approaches to realizing logic gates using only two electrode plasma switches. The first approach used a technique similar to the diode-resistor logic. The second one used space-charge of the plasma to develop logic circuits without wired interconnects. The following sections describe each of these techniques in detail. Basic logic operations like AND, OR, and NOT were performed with these plasma switches. As an extension of the application, a one-bit half adder was also developed.

6.1 Diode-resistor scheme[13]

The logic operations were performed similar in technique to the well-known diode-resistor logic. Fig. 6.1 shows an OR logic implementation using the diode-resistor logic. In this work, the diode was replaced by a microplasma switch. The microplasma switch, unlike a diode, switches with both positive and negative excitation voltages and yet has a well-defined and reproducible threshold voltage. The threshold voltage is determined by the breakdown voltage of the gap. The interelectrode gap in these devices was ~5 μm, which set the breakdown voltage to ~250 V for operation in He. The electrodes were fabricated with 20-μm thick electroplated copper. Fig. 6.2 shows the SEM of some devices.

6.1.1 AND and OR logic

The AND and OR operations were both realized using the same circuit as shown in Fig. 6.3a. Current sources were used for excitation of inputs A and B. The currents from the input were added at the load resistor (R3), which produced a voltage drop. The load resistor could be varied to obtain desired voltage range on the output. Keithley 237 source measurement units were used for excitation. The output voltage was measured using a digital multimeter or an oscilloscope. The microplasma devices behaved like a resistor over a small range of current after the breakdown of gas. Hence, the output voltage response was precise and reproducible as shown in Table 6.1. From Table 6.1, it can be noted that the device could be used as both an AND gate or OR gate by using a suitable threshold. With a threshold of 19 V considered as a logical "1," the device behaved as an OR gate. For a threshold of 38 V, the device was an AND gate. In case of

[13] All the text and figures presented in this section are reprinted, with permission, from P. Pai and M. Tabib-Azar, "Micro-plasma logic gates," *IEEE T. Plasma Sci.*, vol. 42, pp. 1995–1998, 2014. © 2014 IEEE

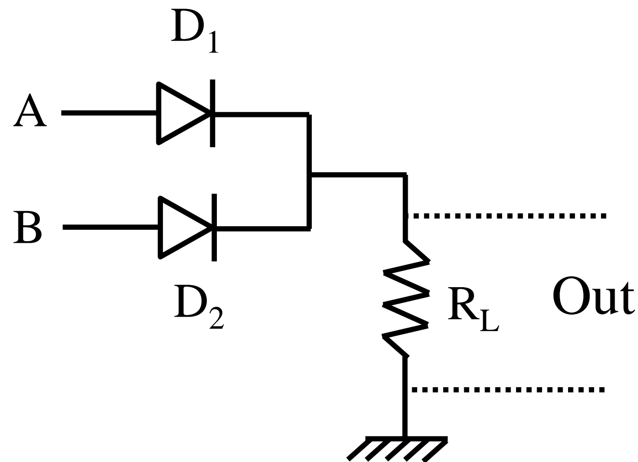

Fig. 6.1. Example of a diode-resistor logic, showing an AND gate implementation.

an AND gate, the voltage levels for the “0” and “1” states differed by 50%, which was reasonable to eliminate ambiguities during operation.

Plasma follows the least resistant path to ground after it is formed. The series resistors (R1 and R2) and load resistor (R3) were set to the given values to prevent any cross-talk between the inputs. When the load resistor was set equal to the series resistors, the plasma current would flow to the load as well as the series resistance of the unexcited input. In other words, if R1 = R2 = R3 and the state of the inputs were A = 0 and B = 1, the current from source B would flow into R1 and R3 by inadvertently creating plasma in the interelectrode gap of the electrode pair near input “A.” To test the dynamic response of the device, current pulses were applied to the inputs A and B. The response was captured on an oscilloscope and is reproduced here in Fig. 6.3b. The input impedance of the oscilloscope was 1 MΩ and could draw most of the current from the input source to itself if directly connected. A current-limiting resistor of 1 GΩ was used in series with the oscilloscope as shown in Fig. 6.3a. Although this prevented loading of the microplasma device, the high value of resistance introduced significant RC delay in the detected input

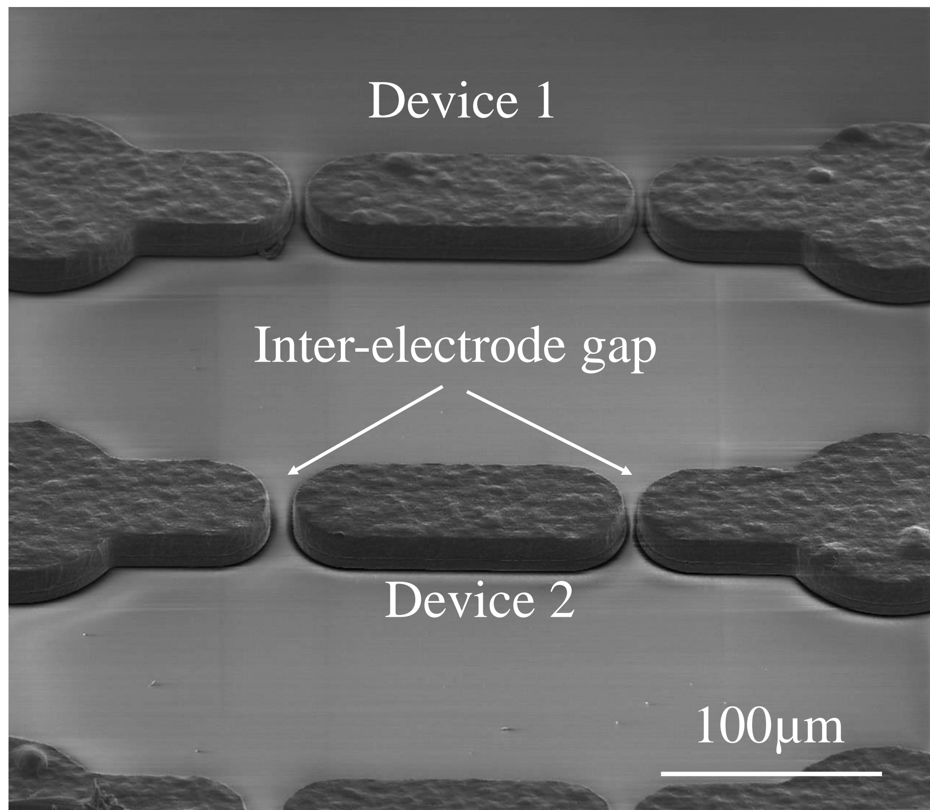

Fig. 6.2. SEM image of some devices used to realize plasma logic gates.

pulses, as seen by the decaying trails. The RC decay time was at least 13 msec, considering 13 pF of the input capacitance of the oscilloscope and neglecting capacitance of the coaxial cable. Stray capacitances and resistances added up to the total capacitive load and further increased the RC delay. Hence, the pulse frequency was set to 1 sec to observe the input transitions clearly. However, the device responded up to 1 kHz successfully, limited only by the frequency limit of the Keithley 237 current source. The limiting frequency of the device was not tested.

6.1.2. XOR logic

The XOR logic was implemented in a similar way as shown in Fig. 6.4a. It is to be noted that in this configuration the two microplasma devices lay parallel to each other

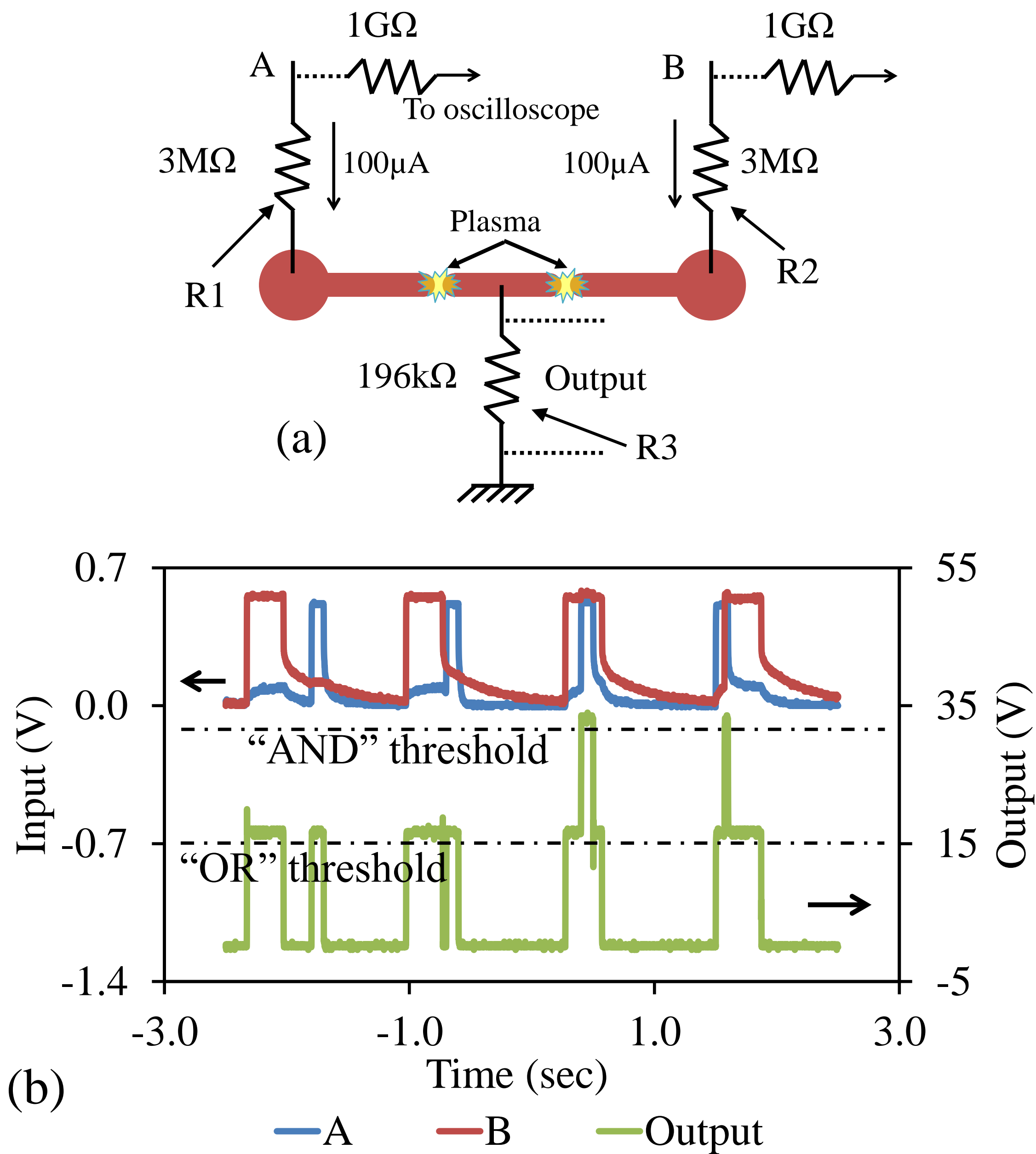

Fig. 6.3. Implementation of AND and OR logic operations. (a) shows schematic of electrode configuration. (b) shows time-domain response of the circuit to input pulses.

Table 6.1. Response of the AND/OR logic circuit of Fig. 6.3a for different combinations of inputs

A (μA)	**B (μA)**	**Output (V)**
0	0	0
0	100	19
100	0	19
100	100	38

and had more interaction area for cross-talk compared to the AND gate of Fig. 6.3a. To prevent cross-talk and unnecessary plasma arcing between devices, they were separated by at least 1 mm. The excitation current was also set to a slightly lower value of 50 μA. The output voltage was a differential voltage between the load resistors of the two devices. Hence it varied in both positive and negative directions when the inputs were individually excited as shown in the response in Table 6.2. The nonzero value of output when both inputs were excited was due to the slight difference in the value of load resistors.

The dynamic response of the device is shown in Fig. 6.4b. The input waveforms showed RC decay similar to the response in Fig. 6.3b. In this case again, the device response was successfully tested up to 1kHz. In both AND and XOR gates, the dynamic response was very well resolved in time, as shown by the narrow transitions in output for minimally overlapping inputs at the fourth peak in Fig. 6.3b. The cause of plasma cross-arcing or device cross-talk in these plasma devices was due to the mutual interaction of the space charge surrounding plasma. This effect is discussed in detail in the next section.

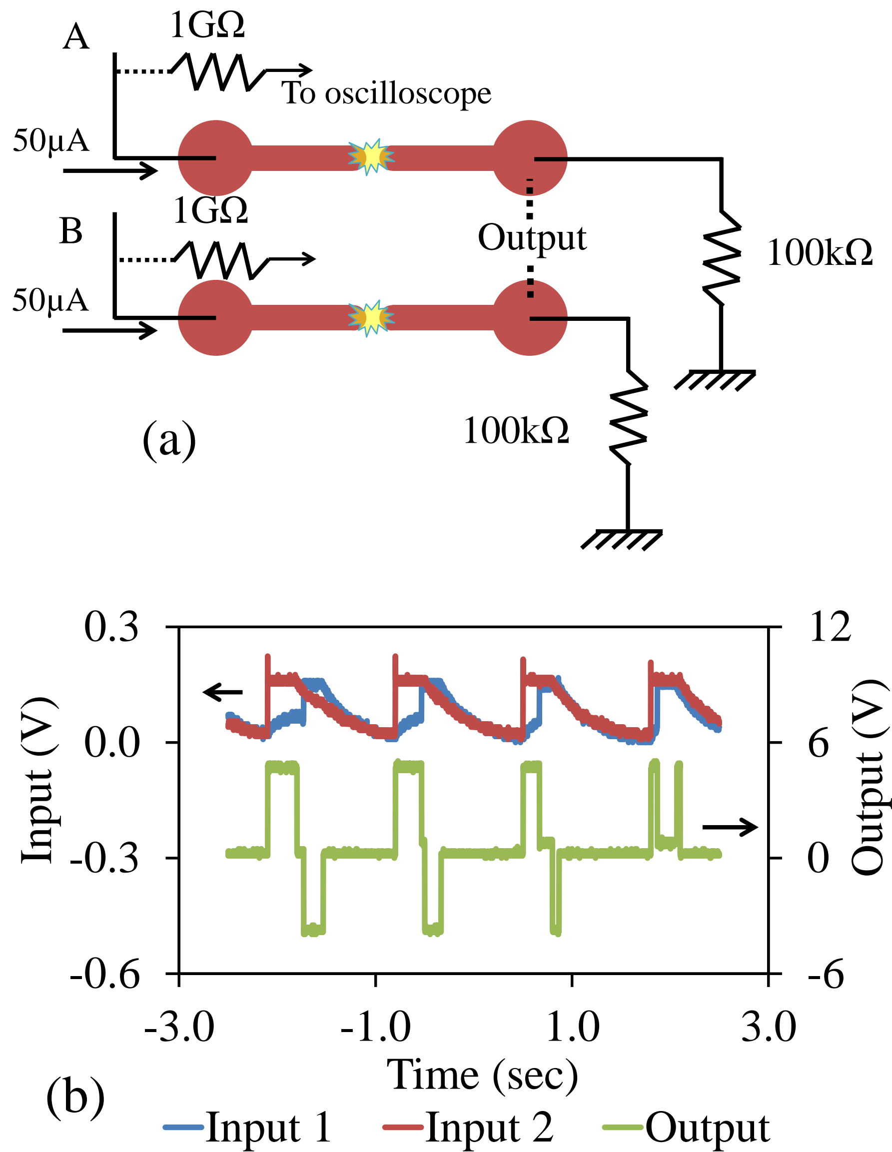

Fig. 6.4. Implementation of XOR logic operation. (a) shows schematic of electrode configuration. (b) shows time-domain response of the circuit to input pulses.

Table 6.2. Response of the XOR logic circuit of Fig. 6.4a for different combinations of inputs

A (µA)	B (µA)	Output (V)
0	0	0
0	50	4.32
50	0	-4.36
50	50	-0.15

6.2. Space charge scheme[14]

The logical switching in this scheme was completely based on the effect of space charge that electrically connects microplasma devices (MPD) to form logic gates *without* any metal interconnects. Once the plasma was turned off, the functional electrical link between the input and the output was completely lost. Moreover, different logical operations could be performed using identical devices and interdevice distances by simply changing the plasma characteristics (density, temperature, and spatial decay constant) electronically. This would allow a user to dynamically program the functionality of μPD circuits in real-time.

To realize logical operations, MPDs were placed in close proximity to each other so that when a device was turned on, the nearby devices' breakdown voltage was lowered by the presence of the space-charge produced by the adjacent device. The logic states of the input and output depended on the plasma being ON or OFF. When the plasma was OFF (ON), a logic "0" ("1") state was obtained. The devices were fabricated using electroplated Cu electrodes with a separation gap of ~5 μm. Fig. 6.5a and b shows SEM of some devices.

The space-charge region at the boundary of the plasma is similar to the Debye sheath that separates the charge-neutral inner plasma region from the outside. Under dc excitation, plasma develops a positive space charge boundary due to accumulation of heavier ions. This positive space charge induces an opposing negative charge through electrons in the surrounding neutral gas region. The effect of these seed electrons on the breakdown voltage of a central device EP0 in Fig. 6.5a was determined while generating

---

[14] All the results and figures presented in this section are reprinted, with permission, from P. Pai and M. Tabib-Azar, "Plasma interconnects and circuits for logic gates and computer sub-circuits," *Appl. Phys. Lett.*, vol. 104, pp. 244102, 2014. Copyright 2014, AIP Publishing LLC.

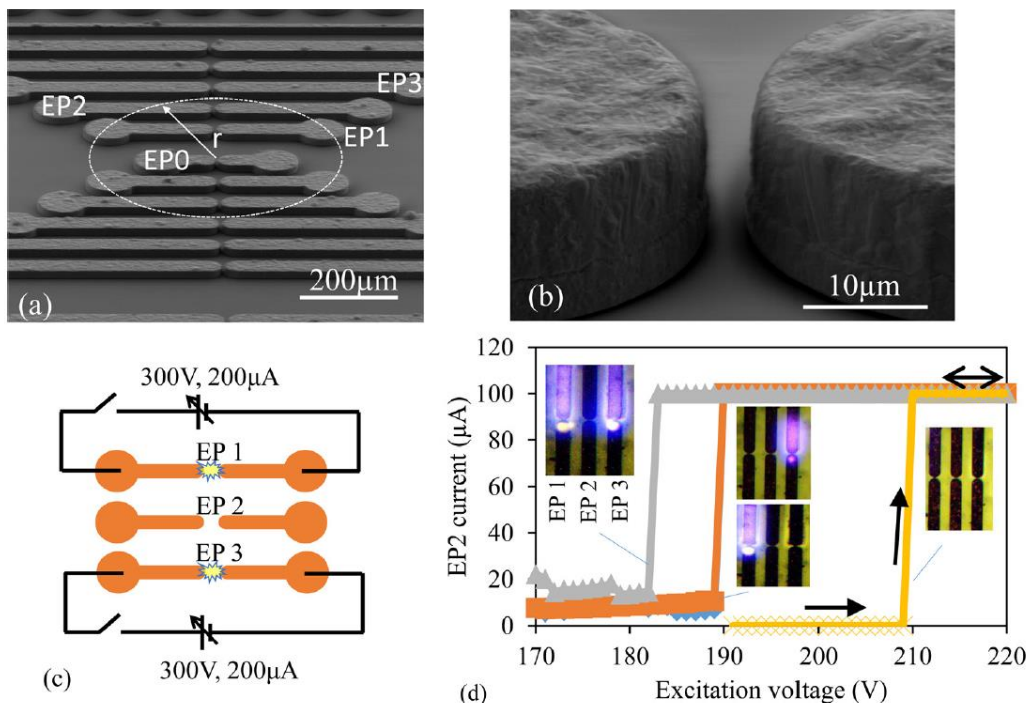

Fig. 6.5. Effect of space charge on the breakdown voltage of a device. (a) and (b) show SEM of some devices. (c) shows the electrode configuration used to characterize breakdown voltage. (d) shows the breakdown voltage dependency on the state of a nearby plasma device.

plasma in nearby devices EP1–EP3. All measurements were carried out at atmospheric pressure in He. The breakdown voltage for EP2 was 210 V when both EP1 and EP3 were OFF (Fig. 6.5d). Turning either EP1 or EP3 ON lowered the EP2 breakdown voltage to 190 V. The breakdown voltage was lowered further to 182 V when both EP1 and EP3 were ON.

The breakdown voltage of a gas is given by eq. (4.2). For interelectrode spacing less than 10 μm, $\gamma' >> \gamma_i$. γ_i ~ 0.0075, is a constant for a given electrode material and gas species, whereas γ' is a function of the applied electric field. A breakdown voltage of 210 V shown in Fig. 6.5d corresponds to an electrode spacing of ~4 μm (Fig. 4.2). The value of γ' for 4 μm electrode spacing is calculated to be 0.067, which translates to 0.067

electrons emitted for every ion. In the presence of seed electrons generated by the space-charge of a nearby device, Eq. 4.2 can be modified to obtain the new breakdown voltage as

$$(\gamma_s + \gamma_i + \gamma') \left[e^{Apd\, exp\left({}^{-Bpd}/_{V_b} \right)} \right] = 1 \qquad (6.1)$$

where γ_s is the electrons available per ionizing collision due to space-charge. The breakdown voltage of EP2 reduced from 210 V to 190 V when EP1 or EP3 was turned ON. Substituting this new breakdown voltage into Eq. 6.1, we get γ_s = 0.074 (compare γ' = 0.067). This implied that there were 0.074 additional electrons available per ionizing collision, which resulted in a lower breakdown voltage. Similarly, the breakdown voltage reduced from 210 V to 182 V when both EP1 and EP3 were turned on, which corresponded to γ_s = 0.084. γ_s is a function of the charge density at the plasma electrodes and the spacing between adjacent electrodes, which consequently affected the breakdown voltage.

The spatial range of the space charge surrounding plasma was determined by measuring conductance of the gas surrounding the plasma electrodes at distances varying from 100 to 500 μm. The effect of different gases was determined using He and Ar mixtures as noted in Fig. 6.6. The charge density (C_p) as a function of distance can be calculated using the Fick's law, and it is approximately given by the exponential relation:

$$C_p(r) = C_p(0).\, e^{-{}^{r}/_{l}} \qquad (6.2)$$

where *r* is the distance from the plasma source (Fig. 6.5a) and *L* is the charge diffusion

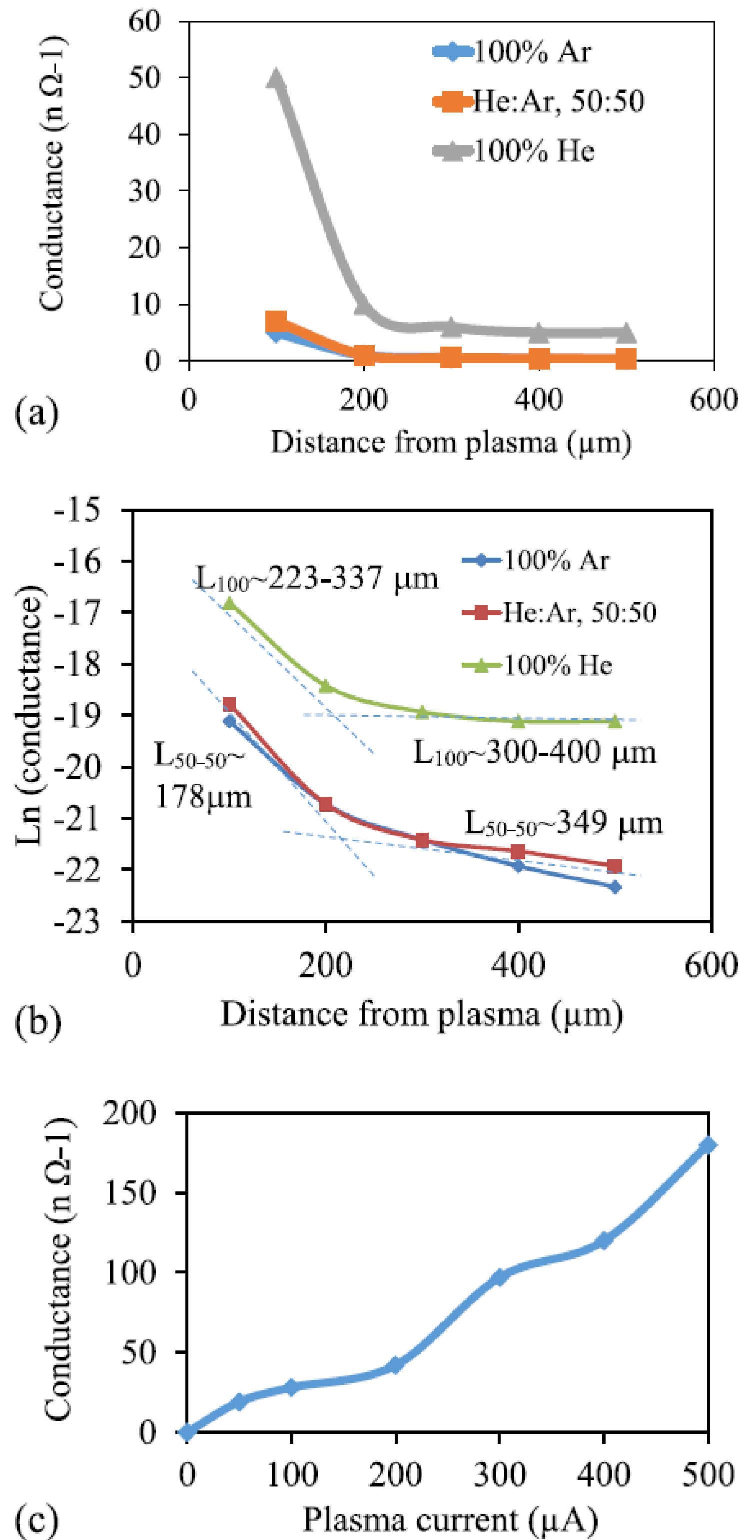

Fig. 6.6. Space-charge characterization of the plasma. (a) shows the decay length of the space-charge. (b) shows the decay lengths in linear-log scales for better understanding. (c) shows the dependence of space-charge density on the plasma current.

length.

Fig. 6.6a shows the conductance of EP0 (Fig. 6.5a) as a function of the distance to other devices at distance r that were subsequently turned “ON” with i) pure Ar plasma, ii) pure He plasma, and iii) 50% He/50% Ar. Fig. 6.6a clearly shows that a nearby plasma affected the conductance and the breakdown voltage of EP0. To understand the spatial-decay of this plasma effect, conductance-distance curves were replotted in a log-linear scale in Fig. 6.6b. In all three cases i)–iii), two distinct decay regimes were observed. Noting that the decay constant L, is the plasma diffusion length $L = \sqrt{D\tau}$, it can be seen that the two distinct decay regimes were associated with two different diffusion coefficients (D) and recombination lifetimes (τ) associated with a) neutral part of the plasma and b) space-charge region in the plasma boundary created by the different electronic and ionic mobilities. In the space-charge region, the diffusion lengths were higher than the charge-neutral regime. This can be qualitatively understood by noting that the electrons usually have larger mobility and a smaller lifetime than ions. Once electrons diffused away, ions were left behind, giving rise to longer diffusion lengths. It was also interesting to note that the decay constants of pure gas plasmas were similar. In the long decay regime, the 50/50 gas plasma had a longer decay constant. The boundary layer space-charge region usually has a lower density than the central and neutral part of the plasma. Also, the conductance change due to nearby plasma almost linearly increased as the plasma current was increased from 50 μA to 500 μA as shown in Fig. 6.6c. The above observations and the plasma hysteresis were used to design and implement logic gates and a 1 bit adder as described in the following subsections.

6.2.1. OR and AND logic

The OR logic operation was implemented using the arrangement shown in Fig. 6.7a. When the central device (X) was biased at 195 V, the voltage would be insufficient to cause a breakdown in the absence of any space charge. However, if either Input A or Input B were turned ON, the space-charge from their plasma would generate plasma at X (Fig. 6.7b). After X was turned ON, it did not turn OFF when the inputs A and B were turned OFF because the plasma at X remained self-sustained at this stage. X could be turned OFF by turning down the bias voltage significantly or turning it OFF. The output voltage was valid only in the duration when the output bias was high. The AND logic was implemented with the same arrangement of devices used for the OR operation by using a lower bias voltage of 185 V across the output device X. The response of the AND gate is shown in Fig. 6.8a. The problem with this configuration was that the difference in breakdown voltage for AND and OR logic was too small (8 V) to switch reproducibly.

Alternately, when the biasing voltage was set much lower than the breakdown voltage, the electric field was insufficient to produce a breakdown but was strong enough to drive the space-charge electrons and produce an appreciable current (Fig. 6.8b). In this case since there was no plasma generated in the output device, the bias voltage was fixed and did not have to be pulsed. Although there was a finite output voltage with one of the inputs high, there was an appreciable margin to differentiate between the two cases. A threshold voltage could be defined to differentiate between the “0” and “1” states.

6.2.2. XOR logic

The XOR gate was implemented with only 2 devices (Fig. 6.9a). The output bias was set to 195 V. Plasma was generated on the input electrode only when inputs A and B

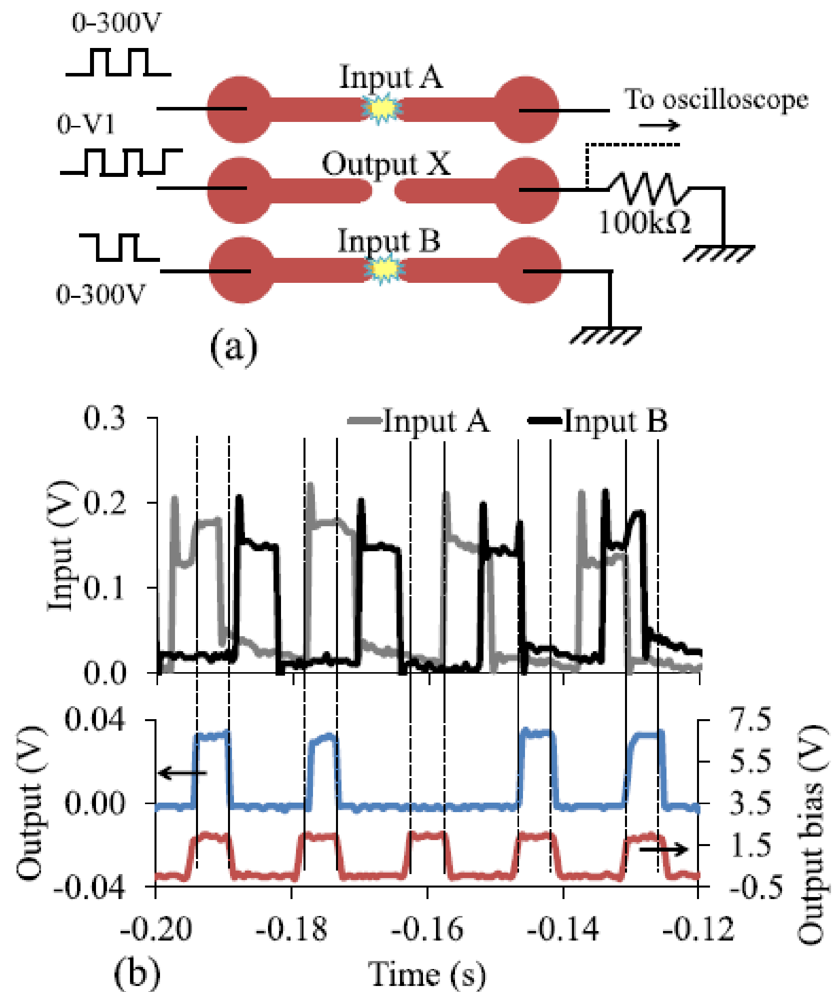

Fig. 6.7. OR gate implementation using space-charge from plasma. (a) shows the electrode configuration. (b) shows time-domain response of the OR gate to input pulses.

were different. The device response is shown in Fig. 6.9b. The same electrode configuration was used to obtain a NOT gate response by connecting Input (B) to 300V. The device response is shown in Fig. 6.9c.

6.2.3. 1-bit half adder circuit

Similar to the logic-gate implementation, a 1-bit half-adder circuit was also realized. The number of MPD devices and shared input signals required for operation was minimized by optimum placement of devices (Fig. 6.10a). The operation of the device for

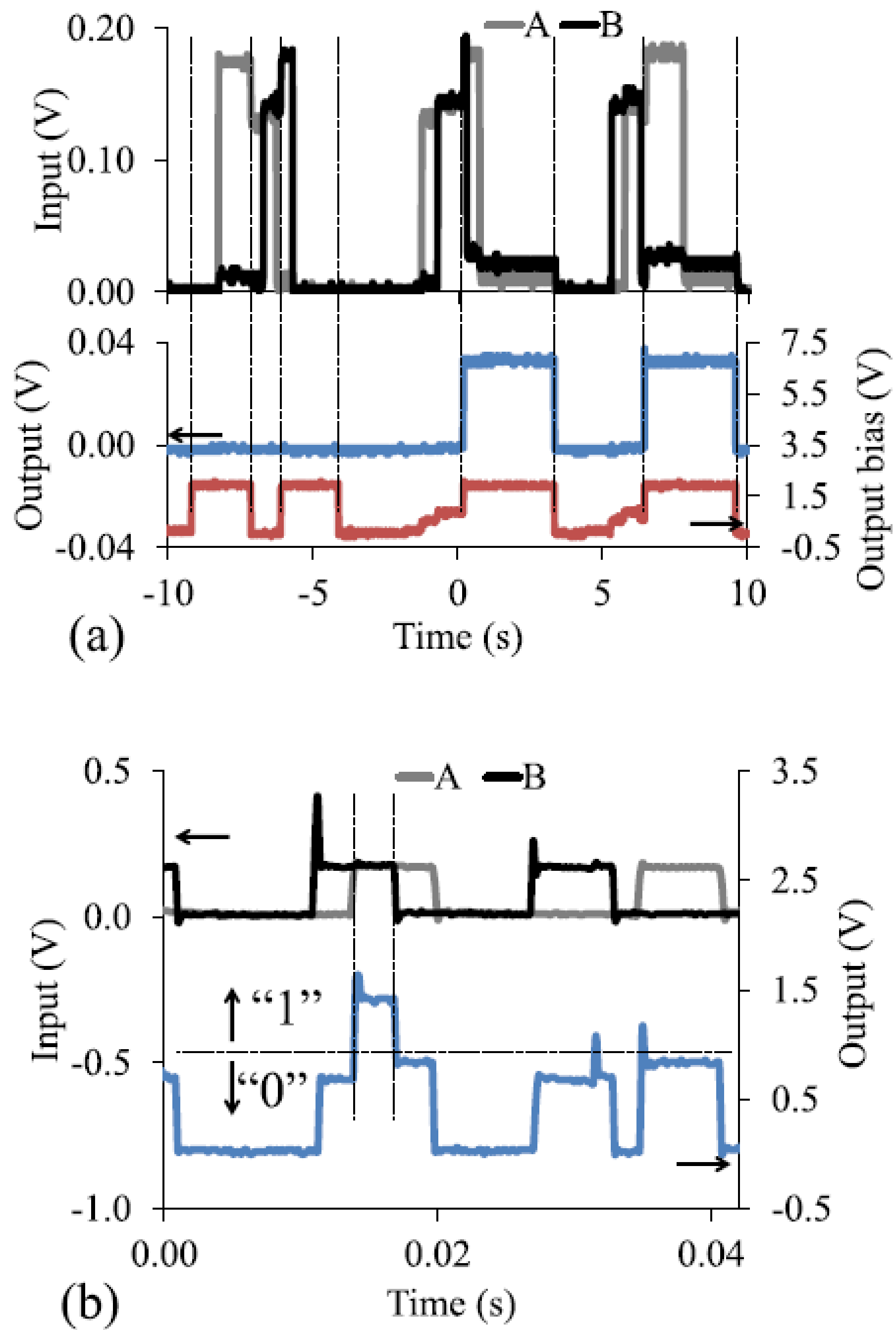

Fig. 6.8. Response of the AND gate to input pulses. (a) shows the response when the output bias voltage was set to 195 V. (b) shows the response when the output bias was set to 150 V.

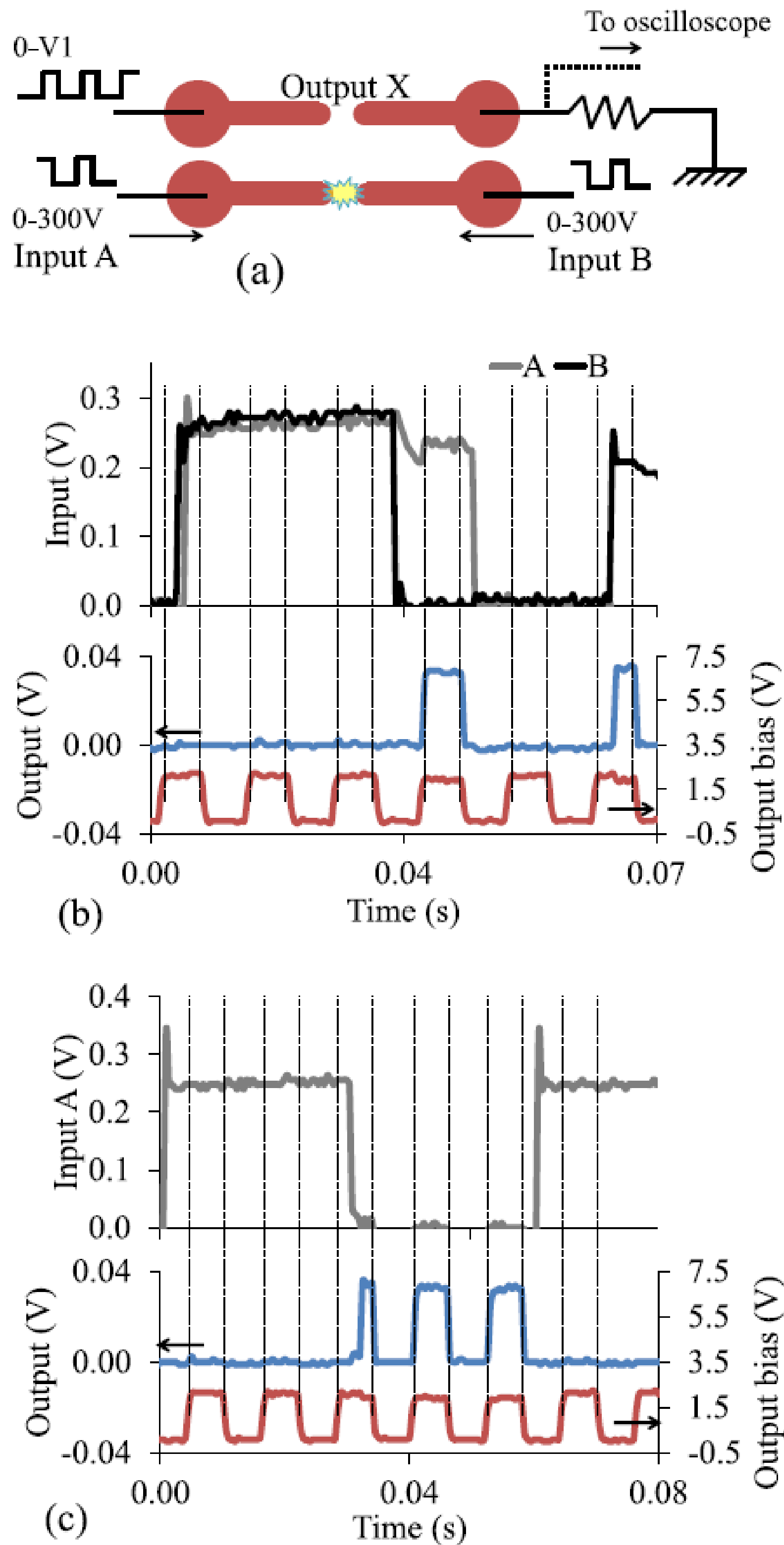

Fig. 6.9. XOR and NOT gate implementation. (a) shows the electrode configuration. (b) shows the response of the XOR gate to input pulses. (c) shows the response of the NOT gate for input pulses.

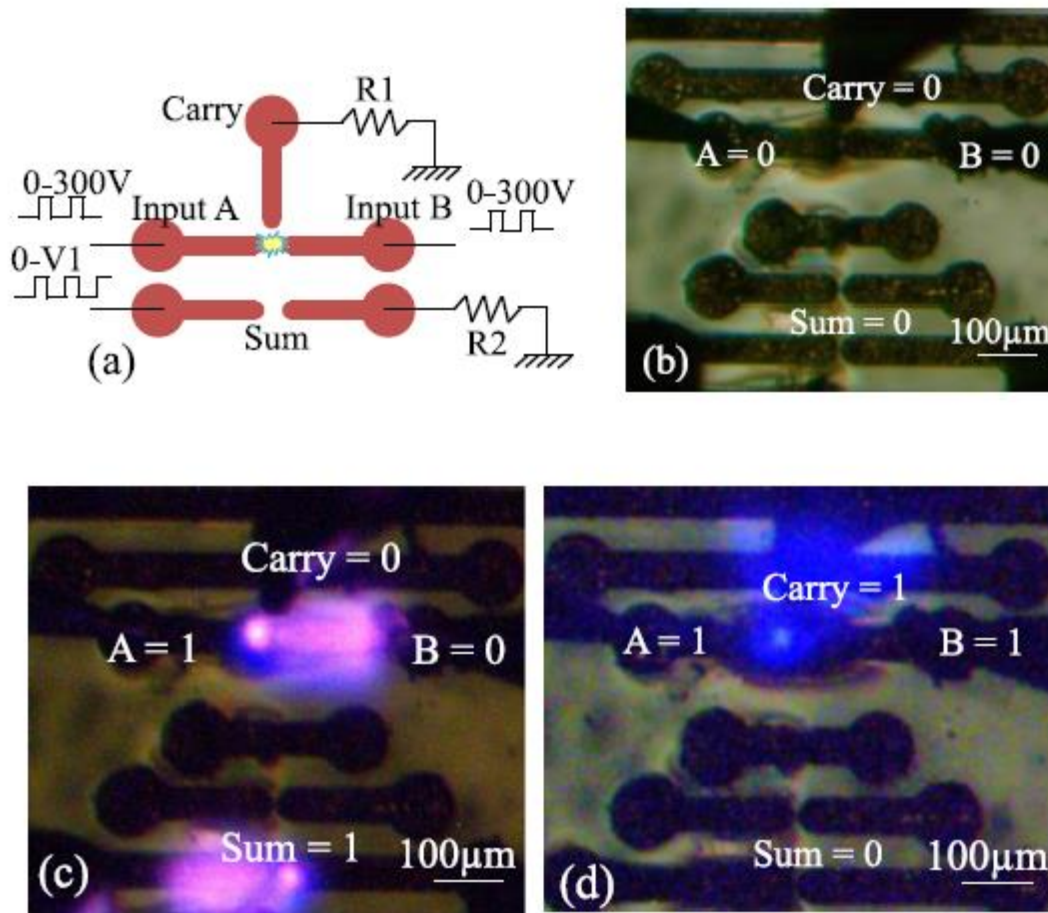

Fig. 6.10. Implementation of 1-bit half adder circuit. (a) shows the electrode configuration. (b), (c), and (d) show photographs of the device in operation with different combination of inputs.

the “Sum” bit was the same as that of XOR. The “Carry” operation was realized by using a resistor R_1 (~100 KΩ), which allowed plasma generation at Carry electrode only when A and B were high, as shown in Fig. 6.10d.

An advantage of implementing logic gates using plasma-linked MPDs is in the reduction of the number of active switching elements. For example, AND and OR gates implemented using CMOS require four transistors each while XOR requires eight transistors. Implementing these gates with plasma-connected circuits required only 2–3 MPDs.

The logic devices presented in this chapter are unique both in their working principle and functionality. One of the main problems in these devices was the unintentional coupling due to the diffusion of the space charge. For practical applications, it is desirable to insulate a significant portion of the plasma electrodes and expose only the tips for plasma creation. This would allow closer spacing of adjacent devices that will improve the device density. The successful implementation of logic gates and even an adder circuit will hopefully help in developing microplasma-based ASICs and microcontrollers for use in harsh environments in the future.

CHAPTER 7

CONCLUSION

This research work successfully developed microplasma devices for electronic applications. The performance of these devices far exceeded the expectations of a plasma device. Through the course of this research work, unique MPDs were developed and tested. The following is a list of the significant contributions of this work.

- Microplasma devices with breakdown voltages of 10s of volts, working in the sub-Paschen regime demonstrated for the first time. By lowering the operating voltages, this work has presented a way to lower the power dissipation by at least a factor of 5 in microplasma devices.
- A good understanding of the gate field-effect mechanism was obtained and attributed to the change in the secondary electron concentration. This technique provides a way to lower the breakdown voltage of microplasma devices electrically, instead of using UV and other high energy irradiation.
- Plasma current modulation at 7 GHz using gate field-effect is a significant step towards possible commercialization of MOPFETs.
- The implementation of logic gates without the use of hard-wired devices shows a novel way of implementing programmable logic gates, in which the same set of electrodes can perform different logical operation depending on the excitation voltages. The technique also showed a significant reduction in the number of

switching elements in a logic gate compared to CMOS, which can improve the power consumption and switching speeds.

The MOPFETs demonstrated their feasibility in both digital and analog applications. There is much work needed to be done to improve the performance of the MOPFET and make it on par with the CMOS devices. The following are some of the device features that need improvement.

- *Gain and transconductance*: The gain and transconductance are currently very small to be of any practical use. One way of increasing these parameters is by increasing the gate area exposed to the channel, which would increase its control on the drain current. An increase in gate area would also increase the gate capacitance, which could result in a reduced switching speed. Further characterization is required to understand these tradeoffs well and optimize the design.
- *Frequency bandwidth*: The bandwidth of MOPFET is currently limited and can be increased by optimizing the geometries of the electrodes for better impedance matching.
- *Breakdown voltage*: Although this work demonstrated very low breakdown voltages compared to earlier microplasma devices, it is still high compared to other electronic devices. The main disadvantage of having higher breakdown voltage is in the static power dissipation. In the absence of a gate signal, the drain source voltage remains active to sustain the plasma. This problem can be addressed by reducing the source-drain gap to reduce the breakdown voltage. A side effect of this would a reduction in the gate area exposed to the channel.

Under such circumstances, the gate could be made 3-dimensional with protruding posts.

- *Operating temperature*: This work used flowing He gas for device operation due to which there was not heating observed in the devices. In a practical application, the device will be sealed in a hermetic package with a fixed volume of gas. With continuous operation of plasma, the gas temperature can be expected to increase over time and thereby increase the temperature of the devices. Although this would not affect the switching properties of the devices significantly, it can physically affect the electrodes. A cooling mechanism in the form of a thermal sink would be a good option under such conditions.

The MOPFETs have shown great potential for use in practical applications especially in harsh environments. The results obtained in this work are promising and will hopefully ignite interest among researchers to pursue this work further and put it to practical use.

REFERENCES

[1] X. Pei, X. Lu, J. Liu, Y. Yang, K. Ostrikov, P. K. Chu, and Y. Pan, "Inactivation of a 25.5 μm enterococcus faecalis biofilm by a room-temperature, battery-operated, handheld air plasma jet," *J. Phys. D, Appl. Phys.*, vol. 45, no. 16, pp. 165205, 2012.

[2] B. Mitra and Y. B. Gianchandani, "The detection of chemical vapors in air using optical emission spectroscopy of pulsed microdischarges from two- and three-electrode microstructures," *IEEE Sens. J.*, vol. 8, pp. 1445–1454, 2008.

[3] Y. Xie, R. Surapaneni, F. Chowdhury, M. Tabib-Azar, and C. H. Mastrangelo, "Fabrication of localized plasma gold-tip nanoprobes with integrated microchannels for direct-write nanomanufacturing," in *Proc. IEEE Sensors*, Nov. 2012.

[4] H. Rahaman, B. Lee, I. Petzenhauser, K. Frank, J. Urban, and R. Stark, "Switching characteristics of microplasmas in a planar electrode gap," *Appl. Phys. Lett.*, vol. 90, pp. 131505, 2007.

[5] J. J. Rocca and K. Floyd, "Glow discharge plasma switch controlled by a small magnetic field," *Appl. Phys. Lett.*, vol. 61, pp. 901–903, 1992.

[6] K. F. Chen and J. G. Eden, "The plasma transistor: A microcavity plasma device coupled with a low voltage, controllable emitter," *Appl. Phys. Lett.*, vol. 93, pp. 161501, 2008.

[7] C. J. Wagner, P. A. Tchertchian, and J. G. Eden, "Coupling electron-hole and electron-ion plasmas: Realization of an npn plasma bipolar junction phototransistor," *Appl. Phys. Lett.*, vol. 97, pp. 134102, 2010.

[8] W. Yuan, F. K. Chowdhury, and M. Tabib-Azar, "Microplasma field effect transistors," in *Tech. Dig. IEEE Micro Electro-Mech. Syst. (MEMS)*, Jan. 2012, pp. 293–296.

[9] M. Cai, F. K. Chowdhury, and M. Tabib-Azar, "Micro-plasma field-effect transistors," in *Proc. IEEE Sensors*, Nov. 2012.

[10] F. K. Chowdhury, Y. Zhang, and M. Tabib-Azar, "Fabrication and characterization of 3D micro-plasma field effect transistors," in *Tech. Dig. IEEE Micro Electro-Mech. Syst. (MEMS)*, Jan. 2013, pp. 669–672.

[11] M. A. Lieberman and A. J. Lichtenberg, *Principles of plasma discharges and material processing*, Second Edition, Hoboken, NJ, John Wiley and Sons, Inc., 2005.

[12] Y. P. Raizer, *Gas discharge physics*, Berlin, Springer-Verlag, 1991.

[13] Y. G. Shen et al., “Residual stress, microstructure, and structure of tungsten thin films deposited by magnetron sputtering,” *J. Appl. Phys.*, vol. 87, pp. 177–187, 2000.

[14] T. Aubert, O. Elmazria, and M. B. Assouar, “Wireless and batteryless surface acoustic wave sensors for high temperature environments,” in *Proc. 9th Int. Conf. on Electron. Meas. Inst.*, Aug. 2009, pp. 2-890–2-898.

[15] L. Chen, *Microelectromechanical system-based wireless microsystem for brain interfacing*, PhD dissertation, Elec. Comp. Eng., University of Utah, Salt Lake City, Utah, 2013.

[16] K. R. Williams, K. Gupta, and M. Wasilik, “Etch rates for micromachining processes – Part II,” *J. Microelectromech. S.*, vol. 5, pp. 256–269, 1996.

[17] C. Reyes-Betanzo, S. A. Moshkalyov, A. C. Ramos, J. A. Diniz, and J. W. Swart, “Study of conditions for anisotropic plasma etching of tungsten and tungsten nitride using SF_6 / Ar gas mixtures,” *J. Electrochem. Soc.*, vol. 149, pp. G179–G183, 2002.

[18] J. M. Albright, L. L. Raja, M. Manley, K. Ravi-Chandar, and S. Satapathy, “Studies of asperity-scale plasma discharge phenomena,” *IEEE T. Plasma Sci.*, vol. 39, pp. 1560–1565, 2011.

[19] R. T. Lee, H. H. Chung, and Y. C. Chiou, “Arc erosion behavior of silver electric contacts in a single arc discharge across a static gap,” *IEE P. Sci Meas. Tech.*, vol. 149, pp. 172–180, 2002.

[20] J. M. Torres and R. S. Dhariwal, “Electric field breakdown at micrometre separations,” *Nanotechnology*, vol. 10, pp. 102–107, 1999.

[21] R. Tirumala and D. B. Go, “An analytical formulation for the modified Paschen’s curve,” *Appl. Phys. Lett.*, vol. 97, pp. 151502, 2010.

[22] M. Radmilovic-Radjenovic and B. Radjenovic, “Theoretical study of the electron field emission in the generation of a micrometer scale discharge,” *Plasma Sources Sci. T.*, vol. 17, pp. 024005, 2008.

[23] C. A. Spindt, I. Brodie, L. Humphrey, and E. R. Westerberg, “Physical properties of thin-film field emission cathodes with molybdenum cones,” *J. Appl. Phys.*, vol. 47, pp. 5248–5263, 1976.

[24] W. B. Kunkel, “Hall effect in plasma,” *Am. J. Phys.*, vol. 49, pp. 733–738, 1981.

[25] R. Johnsen, R. Tosh, and L. A. Viehland, “Mobility of helium ions in neon: comparison of theory and experiment,” *J. Chem. Phys.*, vol. 92, pp. 7264–7266, 1990.

[26] J. M. Madson, H. J. Oskam, and L. M. Chanin, “Ion mobilities in helium,” *Phys. Rev. Lett.*, vol. 15, pp. 1018–1020, 1965.

[27] J. Ryeom, “Novel discharge logic gate for reducing the number of scanning drive circuits of plasma display panel,” *Jpn. J. Appl. Phys.*, vol. 44, pp. L1122–L1125, 2005.